UNIVERSITÀ DEGLI STUDI DI PADOVA

Dipartimento di Ingegneria Industriale

Corso di Laurea Magistrale in Energy Engineering

Neutron-Capture Cross Sections: Experimental Activation and Nuclear-Data Analysis

Supervisor:

Prof. Giuseppe Zollino

Student:

Margutti Francesco (2120838)

Supervisor 2:

Prof. Surjit Mukherjee

Academic Year 2025/2026

A mamma e papà, che mi hanno sempre supportato.

Ai miei due cugini, zii e nonni, punti di riferimento.

A tutti i miei amici, fonti di ispirazione, distrazione e riflessione.

Al professor Surjit, che mi ha aiutato a rendere possibile questo lavoro.

A me stesso, che sono sempre andato avanti.

Abstract

Accurate neutron-capture cross sections are essential for activation analysis, reactor physics, fusion technology, dosimetry, and nuclear fuel-cycle applications. However, their determination is affected by experimental uncertainties and by the nuclear models adopted in theoretical calculations. This thesis investigates these aspects through an experimental study of gold activation and a broader analysis of selected neutron radiative-capture reactions. The overall aim of this work is to compare experimental information with nuclear-model predictions and to identify the main sources of model spread.

The experimental study focused on the $^{197}Au(n,\gamma)^{198}Au$ reaction. Two gold foils were irradiated using Am–Be neutron sources and measured with NaI(Tl) and $LaBr_3$(Ce) scintillation detectors. The induced activity was determined from the 411.8 keV gamma emission of ^{198}Au, leading to an effective cross-section estimate of 8.12 ± 1.71 mb at a representative neutron energy of about 4.2 MeV.

The analysis was then extended to the $^{51}V(n,\gamma)^{52}V$, $^{103}Rh(n,\gamma)^{104}Rh$, $^{209}Bi(n,\gamma)^{210}Bi$, and $^{232}Th(n,\gamma)^{233}Th$ reactions. EXFOR measurements were compared with evaluated nuclear data libraries and TALYS calculations obtained using different Level Density and Photon Strength Function models. Restricted chi-square, empirical covariance, and sensitivity analyses were used to quantify agreement and identify the origin of the model spread.

The experimental value obtained for ^{197}Au is close to the mean TALYS prediction at the representative neutron energy. For several reactions, the largest model spreads were mainly associated with a few TALYS combinations clearly separated from the others. However, the reliability of neutron capture predictions is strongly dependent on both isotope and energy, showing that experimental results, evaluated libraries, and model calculations should be treated as complementary sources of information.

Keywords: Neutron activation analysis; neutron-capture cross sections; gamma-ray spectrometry; evaluated nuclear data libraries; EXFOR; TALYS; empirical covariance analysis; sensitivity analysis.

Table of contents

Chapter 1 – Neutron Activation of ^{197}Au

1.1 Introduction

In neutron activation analysis, a sample is irradiated with neutrons, and some of its nuclei are converted into radioactive products. The radiation emitted by these products can then be measured to determine the activity induced in the sample [1].

Natural gold was selected as the activation material because of the favourable neutron-capture properties of ^{197}Au.

When a neutron is captured, the excited compound nucleus ^{198}Au* is formed. It promptly de-excites through gamma emission, producing radioactive ^{198}Au:

$$^{197}_{79}\mathrm{Au} + \mathrm{n} \rightarrow {}^{198}_{79}\mathrm{Au}^{*} \rightarrow {}^{198}_{79}\mathrm{Au} + \gamma$$

Radioactive ^{198}Au then undergoes β^- decay to excited states of ^{198}Hg. During this process, a neutron is converted into a proton with the emission of an electron (β^-) and an antineutrino ($\bar{\nu}$):

$$\mathrm{n} \rightarrow \mathrm{p} + \beta^- + \bar{\nu}$$

This process increases the atomic number from 79 to 80, leading to the formation of mercury (^{198}Hg), while the mass number remains unchanged [2].

Reaction	Decay data			
	Half-life	Eγ (keV)	Iγ (%)	Decay scheme
^{197}Au(n,γ)^{198}Au	2.6941 d (2)	411.80205 (17)	95.62	β-

Table 1 — Main decay data of ^{198}Au produced by the ^{197}Au(n,γ)^{198}Au activation reaction [2].

The daughter nucleus ^{198}Hg is often produced in an excited state and subsequently de-excites through the emission of gamma radiation. The overall decay process can therefore be summarized as:

$$^{198}_{79}\mathrm{Au} \rightarrow {}^{198}_{80}\mathrm{Hg} + \beta^- + \bar{\nu} + \gamma$$

The most prominent gamma line at 411.8 keV is used for activity determination. By measuring this gamma emission, it is possible to quantify the induced activity in the gold foil.

Figure 1 shows the decay scheme of ^{198}Au as reported in NuDat. The radionuclide decays by β^- emission to excited states of ^{198}Hg, which subsequently de-excite by gamma emission.

The decay scheme reported in NuDat is reproduced in Figure 1 [2]:

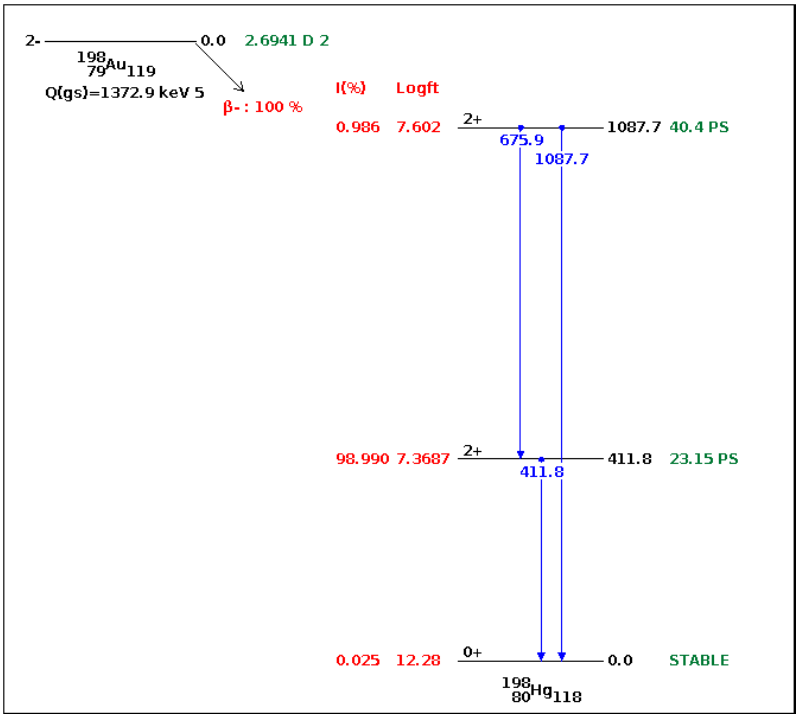

Figure 1 – Decay scheme of $^{198}_{79}$Au to $^{198}_{80}$Hg, showing the main β^- branches and gamma transitions. Reproduced from NuDat3.0/ENSDF, National Nuclear Data Center [2].

1.2 Objective of the Experiment

The experiment was designed to activate natural gold foils through the ^{197}Au(n,γ)^{198}Au reaction and measure the resulting ^{198}Au activity by gamma-ray spectrometry. Two gold foils were irradiated in two different neutron sources for approximately the same irradiation time, calculated individually for each foil. Then, the activated foils were measured using two different gamma detectors. For each foil, three activity measurements were performed with the first detector and two with the second one. The detector efficiencies at 411.8 keV were estimated from calibration measurements performed with ^{133}Ba, ^{134}Cs, and ^{137}Cs sources.

The final objective of the experimental part was to determine the experimental cross section for the ^{197}Au(n,γ)^{198}Au reaction using the measured activity and the estimated neutron flux.

1.3 Details of the Experiment

1.3.1 Setup

The experiment was carried out using two ^{241}Am–Be neutron sources with activities of 185 GBq and 92.5 GBq, respectively. In this type of source, alpha particles emitted by ^{241}Am interact with beryllium and produce neutrons through an (α,n) reaction [3].

Two natural gold foils were used as activation samples due to their high neutron capture cross-section. Each foil was placed on the external surface of a different source holder and irradiated for approximately two days. After irradiation, the activated foils were removed and their gamma emission was measured using two different gamma-ray detectors.

The gamma measurements were performed using two scintillation detectors: NaI(Tl) and $LaBr_3$(Ce). In a scintillation detector, the energy deposited by incident ionizing radiation produces light photons within the scintillator material. These photons are subsequently converted into electrical pulses by a photosensitive device, traditionally a photomultiplier tube. NaI(Tl) is a widely used scintillation material with good gamma-ray detection efficiency, although its energy resolution is relatively limited. $LaBr_3$(Ce), though, provides improved energy resolution, slightly higher detection efficiency, and a faster scintillation response compared with NaI(Tl) [4].

Their performance at the 411.8 keV gamma line is compared in Section 1.3.5.

The gamma spectra were acquired and analysed using the “Gamwin” software.

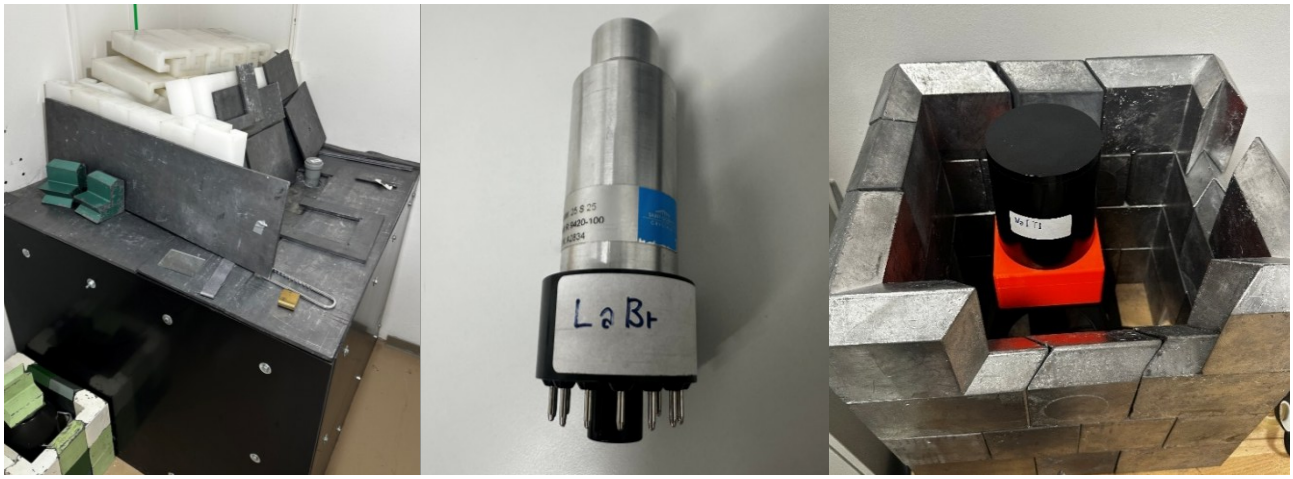

Figure 2 – Experimental equipment used in the activation measurements: (a) shielded irradiation setup housing the Am–Be neutron source, (b) $LaBr_3$(Ce) detector, and (c) NaI(Tl) detector.

1.3.2 Procedure

Before irradiation, each natural gold foil was identified and stored in a labelled plastic envelope. One of the activation samples prepared for the experiment is shown in Figure 3.

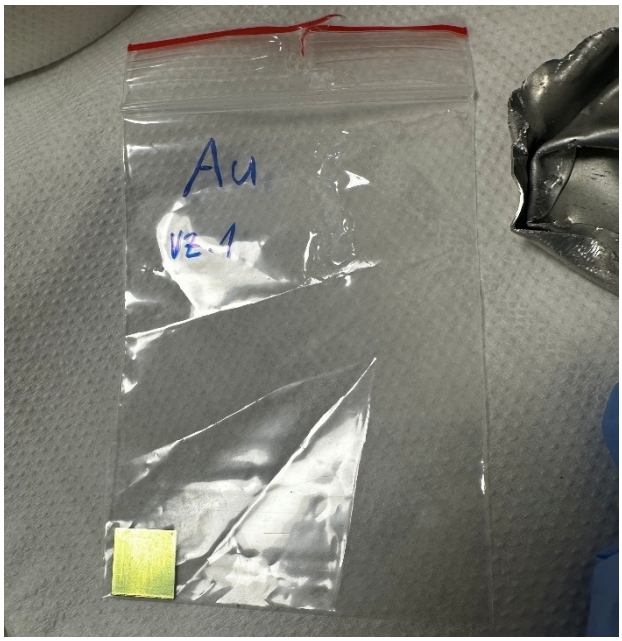

Figure 3 – One of the natural gold foils used as an activation sample, stored in its labelled plastic envelope

The gold foils were irradiated in the neutron sources for a period of approximately two days. The irradiation started on March 4th, 2026, at 15:54 and 16:01 for the two foils, respectively, and ended on March 6th, 2026, at 13:30 and 14:16. The irradiation time t_{irr} was calculated individually for each foil based on the recorded start and end times.

After irradiation, the foils were removed from the neutron sources and transferred to the measurement setup. For each acquisition, the cooling time $\mathrm{t_{cool}}$ was defined as the interval between the end of irradiation and the start of the measurement.

The gamma spectra of the activated foils were acquired using two detectors. For each foil, multiple measurements were performed in order to improve the statistical reliability of the results. In particular, three measurements were carried out using the first detector, while two measurements were performed using the second detector.

Each acquisition was performed with a live time greater than 600 s.

All gamma measurements were performed using the same measurement geometry. Both the activated gold foils and the calibration sources were placed on a plastic support positioned on the detector, corresponding to an approximate source-detector distance of 1 cm.

1.3.3 Measurements

For each measurement, the following parameters were recorded from the Gamwin software: energy of the selected gamma peak, live time, real time, dead time, gross area, background area, net area, and the associated uncertainty. The net peak area was used for the subsequent calculation of the activity.

1.3.4 Data processing of gamma spectra

The analysis of the gamma spectra was performed using the Gamwin software. The region of interest around the 411.8 keV peak was manually selected by defining appropriate left and right boundaries. The peak was identified using the "Peak Search → Manually" function.

The net peak area was determined using the "Peak Area" function, while the peak shape was fitted using a Gaussian function through the "Peak Fit" tool [5].

The selected region of interest and the fitted 411.8 keV peak are shown in the representative spectra reported in Figure 4.

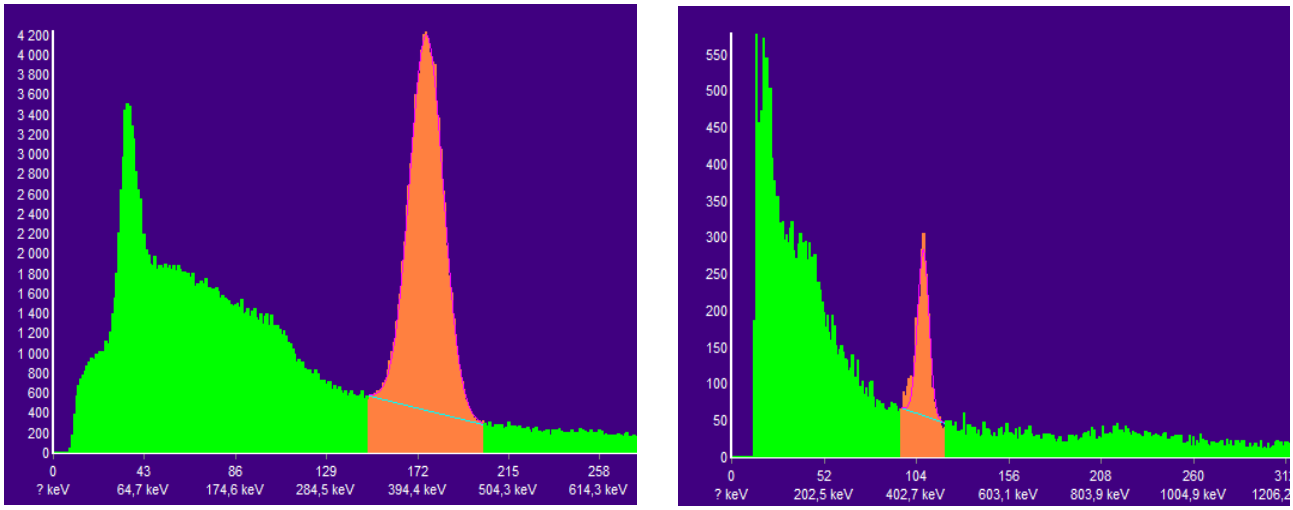

a) b)

Figure 4 – Representative gamma spectra acquired and analysed in Gamwin for the gold foil irradiated in the higher-activity neutron source, measured with (a) the NaI(Tl) detector and (b) the $LaBr_3(Ce)$ detector. The highlighted region corresponds to the characteristic 411.8 keV gamma peak of ^{198}Au.

1.3.5 Peak resolution of the detectors

The energy resolution of the detectors was evaluated by analysing the width of the gamma peak corresponding to the main emission of ^{198}Au, located at approximately 411.8 keV [2]. The resolution was defined as:

$$R = \frac{\text{FWHM}}{E}$$

where FWHM is the full width at half maximum of the peak and E is the measured peak energy.

The FWHM values were obtained from the Gaussian fitting of the gamma peaks performed in Gamwin. Figure 4 shows representative spectra of the gold foil irradiated in the higher-activity neutron source and subsequently measured with the two scintillation detectors. The characteristic 411.8 keV peak of ^{198}Au is clearly visible in both spectra. However, the peak recorded with the $LaBr_3$(Ce) detector is visibly narrower than that obtained with the NaI(Tl) detector, providing a direct qualitative indication of its better energy resolution.

The quantitative resolution results obtained from all the analysed spectra are reported in Table 2.

	Peak Resolution			
Au Foil	Detector	Meas. #	FWHM [keV]	FWHM rel. [%]
Foil 1	1	1	47.75	11.79
Foil 1	1	2	47.49	11.72
Foil 1	1	3	47.78	11.79
Foil 1	2	1	29.04	6.96
Foil 1	2	2	27.49	6.57
Foil 2	1	1	46.93	11.58
Foil 2	1	2	47.73	11.77
Foil 2	1	3	46.89	11.57
Foil 2	2	1	24.29	5.8
Foil 2	2	2	32.28	7.74

Peak Resolution	
Detector	FWHM rel. (Average val.)[%]
1	11.70
2	6.77

Table 2 – Peak-resolution results obtained from the Gamwin analysis of the activated gold-foil spectra, showing the FWHM and relative FWHM values for each measurement and detector

Detector 1, corresponding to the NaI(Tl) detector, has an average relative energy resolution of approximately 11.7%, whereas Detector 2, corresponding to the $LaBr_3$(Ce) detector, provides an improved average resolution of approximately 6.77%. These results are consistent with the visibly broader ^{198}Au peak observed for NaI(Tl) and the narrower peak obtained with $LaBr_3$(Ce) [4].

The improved energy resolution of the $LaBr_3(Ce)$ detector allows more accurate peak identification and background separation, which improves the reliability of the net peak-area determination and the resulting activity calculation.

1.3.6 Efficiency calibration of the detectors

The activity calculation required the full-energy peak efficiency of each detector at the 411.8 keV gamma line of ^{198}Au.

The efficiency calibration was performed using these sealed gamma-ray sources:

-^{133}Ba (initial activity 3.38 kBq, $T_{1/2}$ = 10.53 yrs, and date of manufacture = 30/09/2014);

-^{134}Cs (initial activity 300.40 kBq, $T_{1/2}$ = 2.06 yrs, and date of manufacture = 01/02/2015);

-^{137}Cs (initial activity 16.63 kBq, $T_{1/2}$ = 30.01 yrs, and date of manufacture = 01/02/2015).

The reference activities and reference dates were taken from the source. The radionuclide half-lives, gamma-ray energies, and emission probabilities used in the calculations were obtained from NuDat [2].

Figure 5 – Calibration sources used for efficiency determination (^{133}Ba, ^{134}Cs, ^{137}Cs)

These reference sources provide well-characterized gamma emissions in the energy region surrounding the 411.8 keV line of interest. In particular, the selected calibration lines were approximately 356 keV for ^{133}Ba, 605 keV for ^{134}Cs, and 662 keV for ^{137}Cs.

Each calibration source was measured with both detectors, providing a separate efficiency value for each detector. The efficiency $\varepsilon(E_\gamma)$ at a given gamma energy was calculated using the following relation:

$$\varepsilon(E_\gamma) = \frac{N}{A(t)\, I_\gamma\, t_{live}}$$

where N is the net peak area, $A(t)$ is the activity of the source at the time of measurement, I_γ is the emission probability of the gamma line, and t_{live} is the live time of the acquisition.

The activity of each source at the measurement time was obtained by applying radioactive decay correction:

$$A(t) = A_0\, e^{-\lambda \Delta t}$$

where A_0 is the reference activity provided by the manufacturer, λ is the decay constant, and Δt is the elapsed time between the reference date and the measurement date.

For each energy point, two efficiency values were obtained, one for each detector. The resulting efficiency values were then plotted as a function of energy.

In order to estimate the detector efficiency at 411 keV, a second-order polynomial interpolation was performed using the three available calibration points. The interpolation was carried out using the Lagrange polynomial formulation, which provides a quadratic function passing exactly through the known data points.

The interpolated efficiency was calculated according to:

$$\varepsilon(E) = \varepsilon_1 \frac{(E-E_2)(E-E_3)}{(E_1-E_2)(E_1-E_3)} + \varepsilon_2 \frac{(E-E_1)(E-E_3)}{(E_2-E_1)(E_2-E_3)} + \varepsilon_3 \frac{(E-E_1)(E-E_2)}{(E_3-E_1)(E_3-E_2)}$$

where E_1, E_2, and E_3 are the gamma energies of the calibration sources, and ε_1, ε_2, and ε_3 are the corresponding efficiencies.

The efficiency at the energy of interest was obtained by evaluating the polynomial at 411.8 keV and then used in the activity calculation for the irradiated gold foils.

The resulting efficiency curves for both detectors are shown in Figure 6:

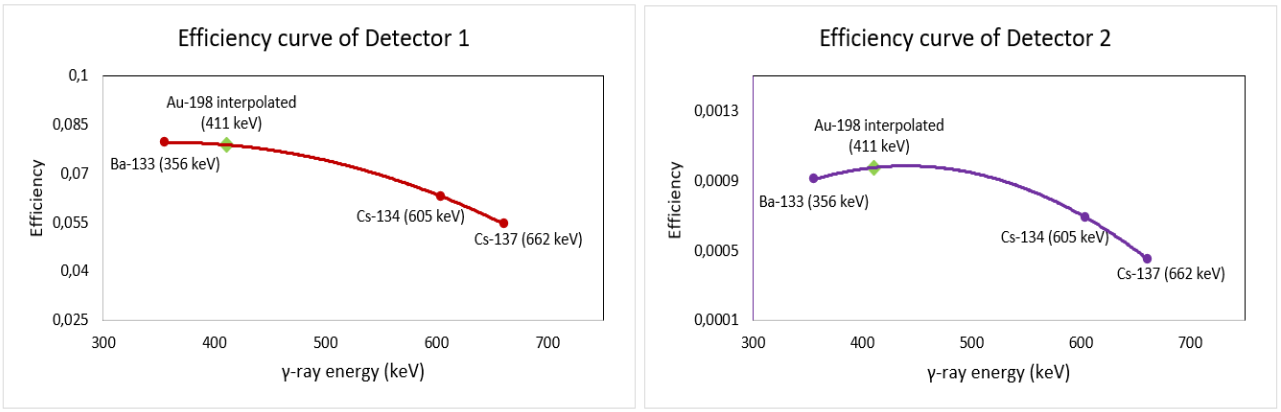

Figure 6 – Efficiency curves of Detector 1 and Detector 2 as a function of gamma energy, including the interpolated value at 411 keV.

1.3.7 Activity determination of ^{198}Au

The induced activity of the irradiated gold foils was determined from the measured gamma spectra by analysing the dominant 411.8 keV gamma emission of ^{198}Au [2].

The activity was calculated taking into account the detector efficiency, the emission probability of the gamma line, and the corrections for decay during cooling and measurement. The activity at the end of irradiation was obtained using the following expression:

$$A_{EOI} = \frac{N \cdot \lambda \cdot \frac{t_{real}}{t_{live}}}{\varepsilon(E_\gamma) \cdot I_\gamma \cdot e^{-\lambda t_{cool}} \cdot (1 - e^{-\lambda t_{real}})}$$

Where:

N is the net peak area,

$\varepsilon(E_\gamma)$ is the detector efficiency at 411 keV,

I_γ is the gamma emission probability,

λ is the decay constant of ^{198}Au,

t_{live} is the live time of the measurement,

t_{real} is the real time of the measurement,

t_{cool} is the cooling time between the end of irradiation and the start of the measurement.

The decay constant lambda was calculated from the half-life of Au-198 as:

$$\lambda = \frac{\ln 2}{T_{1/2}}$$

The net peak area N was obtained from the Gamwin software by fitting the 411 keV peak with a Gaussian function and subtracting the background contribution [5].

Several activity values were obtained for each foil, since three measurements were performed with Detector 1 and two with Detector 2. The final activity of each foil was determined by averaging the values obtained from the repeated measurements. The consistency between the results obtained with the two detectors was also used as a validation of the measurement and data processing procedure.

1.3.8 Neutron flux estimation from the Am–Be source

The neutron flux at the position of the gold foils was estimated from the activity of the Am–Be source. Since the ^{241}Am activity decreases with time due to radioactive decay, its value at the irradiation date was first calculated.

The activity was corrected using the radioactive decay law:

$$A(t) = A_0 e^{-\lambda \Delta t}$$

where A_0 is the initial activity of the source, λ is the decay constant of ^{241}Am, and Δt is the elapsed time between the reference date and the measurement date. The decay constant was calculated as:

$$\lambda = \frac{\ln 2}{T_{1/2}}$$

with a half-life $T_{1/2}$ of 432.6 years for ^{241}Am [2].

The neutron emission rate was estimated from the activity of the ^{241}Am–Be source according to:

$$S = A(t) \cdot Y$$

where A(t) is the activity of the ^{241}Am source at the irradiation date and Y is the neutron yield per unit activity. A typical neutron yield of 2.2×10^6 n s^{-1} Ci^{-1}, corresponding to approximately 5.95×10^{-5} n s^{-1} Bq^{-1}, was adopted from the literature [6]. Since the reported value represents a typical yield for Am–Be sources rather than a certified emission rate for the specific sources used in the experiment, the resulting neutron source strength and flux should be regarded as approximate estimates.

The neutron flux at a distance r from the source was estimated using:

$$\phi = \frac{S}{4\pi r^2}$$

where ϕ is the neutron flux expressed in n cm^{-2}s^{-1}, and r is the distance between the source and the foil position.

In this work, a source-to-foil distance of approximately 0.05 cm was assumed. This choice reflects the actual experimental configuration, in which the gold foils were positioned on the external lower surface of the cylindrical source holder, as close as possible to the neutron source. The active neutron source was located inside the cylindrical holder; therefore, the foils were not in direct contact with the active material, but were separated from it by the external cover of the source holder and by the thin plastic envelope used to contain the foils.

The effective distance between the active source and the foil cannot be determined precisely, and the value of 0.05 cm was adopted as a working assumption. Since this distance is comparable to the dimensions of the source assembly, the point-source relation is used at the limit of its range of applicability, and the resulting flux is strongly sensitive to the assumed geometry.

In addition, the neutron field at the sample position was not characterized in this work.

The sources are housed in a shielded assembly, so the neutron energy distribution reaching the foil may differ from the emission spectrum of the bare source. The flux used here is therefore a reference value based on the source emission properties, rather than a measured flux at the sample position.

1.3.9 Cross Section Determination

The experimental cross section of the ^{197}Au(n,γ)^{198}Au reaction was determined using the activation equation, which relates the induced activity to the neutron flux, the number of target nuclei, the reaction cross section, and the saturation factor associated with the irradiation time [7]:

$$A_{EOI} = N_{target}\, \sigma\, \phi\, (1 - e^{-\lambda t_{irr}})$$

The number of gold atoms in each foil was calculated from the foil mass according to:

$$N_{target} = \frac{m}{M} N_A$$

where $m$is the mass of the foil, $M = 196.97$ g mol^{-1} is the molar mass of gold, and $N_A = 6.022 \times 10^{23}$ mol^{-1} is Avogadro's number.

The activity at the end of irradiation, A_{EOI}, was used in the calculation.

The production of ^{198}Au during irradiation is governed by the decay constant:

$$\lambda = \frac{\ln 2}{T_{1/2}}$$

where $T_{1/2}$ is the half-life of ^{198}Au. The growth of activity during irradiation is described by the saturation factor:

$$1 - e^{-\lambda t_{irr}}$$

which accounts for the simultaneous production and decay of the radioactive nuclei.

The cross section was therefore calculated by rearranging the activation equation:

$$\sigma = \frac{A_{EOI}}{N_{target}\,\phi\,(1 - e^{-\lambda t_{irr}})}$$

where ϕ is the neutron flux previously estimated from the Am–Be source.

All quantities were expressed in consistent units, resulting in a cross section expressed in cm^2. For comparison with literature values, the results were subsequently converted into barns using:

$$1 \text{ barn} = 10^{-24} \text{ cm}^2$$

Because each foil was measured several times with both detectors, more than one cross-section value was obtained for each foil. These values were then averaged to obtain a representative result.

1.4 Results

1.4.1 Activity

The results obtained for Foil 1 with Detector 1 show a good internal consistency, with values around 1470–1490 Bq. The values obtained with Detector 2 are also consistent with each other and lie around 1240–1255 Bq. A small discrepancy between the results obtained with the two detectors can be observed, with Detector 2 providing systematically lower values compared to Detector 1. This systematic difference may be associated with uncertainties in the detector-efficiency calibration, measurement geometry, and net peak-area determination.

Measurement table				
Au Foil	Detector	Meas. #	A_EOI [Bq]	A_EOI Average values
Foil 1	1	1	1489.6557	1479.8290
Foil 1	1	2	1471.4612	
Foil 1	1	3	1478.3701	
Foil 1	2	1	1253.5065	1247.8299
Foil 1	2	2	1242.1533	
Foil 2	1	1	1127.9612	1140.3621
Foil 2	1	2	1153.9202	
Foil 2	1	3	1139.2049	
Foil 2	2	1	849.4467	929.0189
Foil 2	2	2	1008.5911	

Table 3 – Measured activity values of Au-198 for the irradiated gold foils obtained using Detector 1 and Detector 2.

The repeatability is good for Foil 1 with both detectors, whereas the two acquisitions of Foil 2 with Detector 2 differ by about 17%, indicating a larger scatter in the corresponding determination of the net peak-area. This spread is reflected in the uncertainty quoted for the final cross section.

1.4.2 Measured Activity vs Time

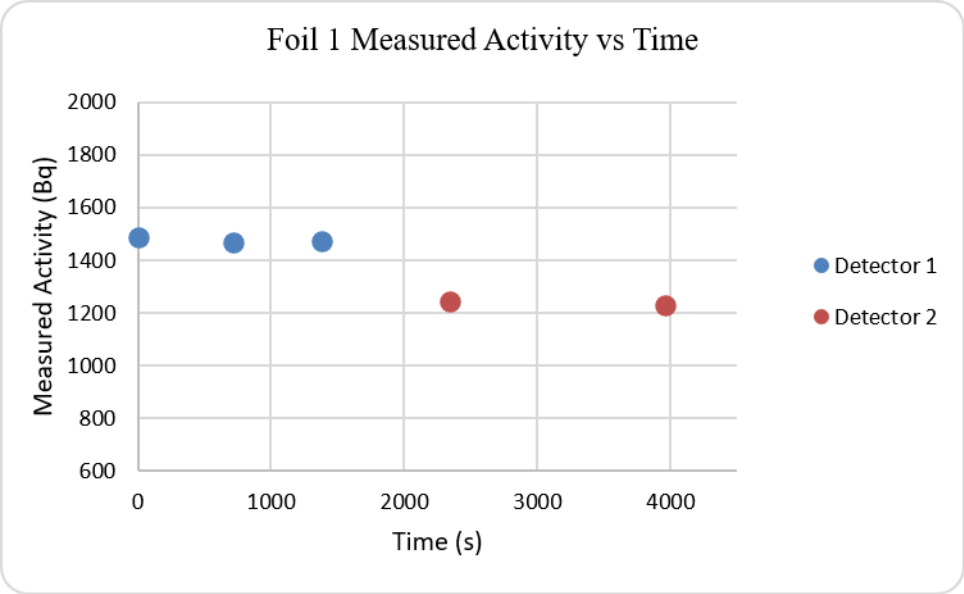

Figure 7 – Measured activity A_{meas} of Foil 1 as a function of elapsed time from the first acquisition. The limited variation of activity reflects the short measurement interval compared to the half-life of Au-198.

The activity values plotted in Figure 7 correspond to the measured activity values, A_{meas}, that is the activity at the time of each acquisition, without applying the correction for decay during the cooling time. In other words, these values were not referred to the end of irradiation but were left in their measured form in order to visualize the temporal evolution of the activated foil during the counting sequence.

However, the resulting trend does not show a clear exponential decrease, and only a limited variation of the activity is observed over time.

This behaviour can be explained by considering the relatively long half-life of ^{198}Au compared to the short time interval between consecutive measurements. The half-life of ^{198}Au is approximately 2.7 days [2], corresponding to about 233000 seconds. The decay constant is therefore:

$$\lambda = \frac{\ln 2}{T_{1/2}} \approx \frac{0.693}{233000} \approx 2.97 \times 10^{-6} \quad \mathrm{s}^{-1}$$

To estimate the expected variation of activity over a typical time interval of 10 minutes ($t = 600$ s), the decay law can be applied:

$$e^{-\lambda t} = e^{-2.97\times10^{-6}\cdot 600} \approx e^{-0.00178} \approx 0.9982$$

This corresponds to a decrease of only:

$$(1 - 0.9982) \times 100 \approx 0.18\%$$

Even for longer intervals, such as $t = 1400$s:

$$e^{-\lambda t} \approx e^{-0.00416} \approx 0.996$$

which corresponds to a decrease of approximately 0.4%.

These variations are extremely small compared to the experimental uncertainties associated with the activity determination, such as counting statistics, peak fitting, and detector efficiency calibration. As a result, the expected decay signal is masked by the experimental scatter of the data.

Over the duration of the measurement sequence, the expected decrease was too small to be distinguished from the experimental scatter.

1.4.3 Experimental Cross Section

The obtained values show a consistent order of magnitude, lying in the range of approximately 6 to 10 mb, depending on the foil and the detector considered.

Measurement table

Au Foil	Detector	Meas. #	A_EOI [Bq]	σ [cm^2]	σ average values [cm^2]	σ [mb]	σ average values [mb]
Foil 1	1	1	1489.656	7.2308E-27	7.1831E-27	7.231	7.183
Foil 1	1	2	1471.461	7.142E-27		7.142	
Foil 1	1	3	1478.370	7.176E-27		7.176	
Foil 1	2	1	1253.507	6.085E-27	6.057E-27	6.085	6.057
Foil 1	2	2	1242.153	6.029E-27		6.029	
Foil 2	1	1	1127.961	1.016E-26	1.0276E-26	10.165	10.276
Foil 2	1	2	1153.920	1.040E-26		10.398	
Foil 2	1	3	1139.205	1.027E-26		10.266	
Foil 2	2	1	849.447	7.655E-27	8.372E-27	7.655	8.372
Foil 2	2	2	1008.591	9.089E-27		9.089	

Table 4 – Experimental cross-section values of Au-197 for each foil and detector, including average values.

A systematic difference between the two detectors can be observed, with Detector 2 generally providing lower cross-section values compared to Detector 1. This discrepancy is consistent with the differences previously observed in the activity determination and is likely related to uncertainties in the detector efficiency calibration and peak fitting procedure.

The cross-section values obtained for the two foils differ by about 40%, Foil 2 giving the higher values. This difference is within the overall scatter of the individual determinations, but it suggests a residual systematic effect related to the assumed geometry. Since both foils were irradiated using sources of the same Am–Be type, the same reference neutron-energy distribution was assumed for the two calculations [3].

The neutron flux used in the calculation was estimated from the Am–Be source assuming a simplified geometrical model and a literature-based neutron yield [6]. As discussed previously, the flux is highly sensitive to the assumed source-to-foil distance and to the value of the neutron yield, which introduces a non-negligible uncertainty in the final result.

Additional uncertainties arise from the activity determination, including counting statistics, peak fitting, and efficiency calibration, which propagate into the calculated cross section.

Averaging the ten individual determinations gives **8.12 ± 1.71 mb**, where the quoted uncertainty represents the standard deviation of the measured values. This value is an effective cross section obtained under the flux assumptions described in Section 1.3.8, and its absolute scale depends directly on them. It is therefore reported as a reference experimental result rather than as an independent absolute measurement, and the comparisons presented in the following sections should be read in this sense.

1.5 Comparisons

1.5.1 Comparison with EXFOR Data and Evaluated Libraries

The experimental cross section obtained in this work was compared with the available experimental measurements retrieved from the EXFOR database [8] and with the evaluated cross sections provided by ENDF/B-VIII.0, JEFF-3.3, JENDL-5, TENDL-2023, ROSFOND-2010, and CENDL-3.2 [9-14].

For the graphical comparison, the experimental result obtained in this work was associated with a representative neutron energy of approximately 4.2 MeV, corresponding to the commonly adopted average energy of an Am–Be neutron spectrum [15]. Since the Am–Be source produces a broad neutron-energy spectrum, the value represented at 4.2 MeV should be interpreted as an effective spectrum-averaged estimate plotted at a representative energy, rather than as a monoenergetic differential cross section.

As shown in Figure 8, the evaluated libraries present a similar decreasing trend with increasing neutron energy. The experimental value obtained in this work remains of the same order of magnitude as the evaluated-library predictions, although it lies slightly below the main evaluated-library trend

in the 4 MeV energy region. This difference may be partly associated with the simplified neutron-flux estimation, the broad energy distribution of the Am–Be source, and the uncertainties related to detector efficiency calibration, peak fitting, and activity determination.

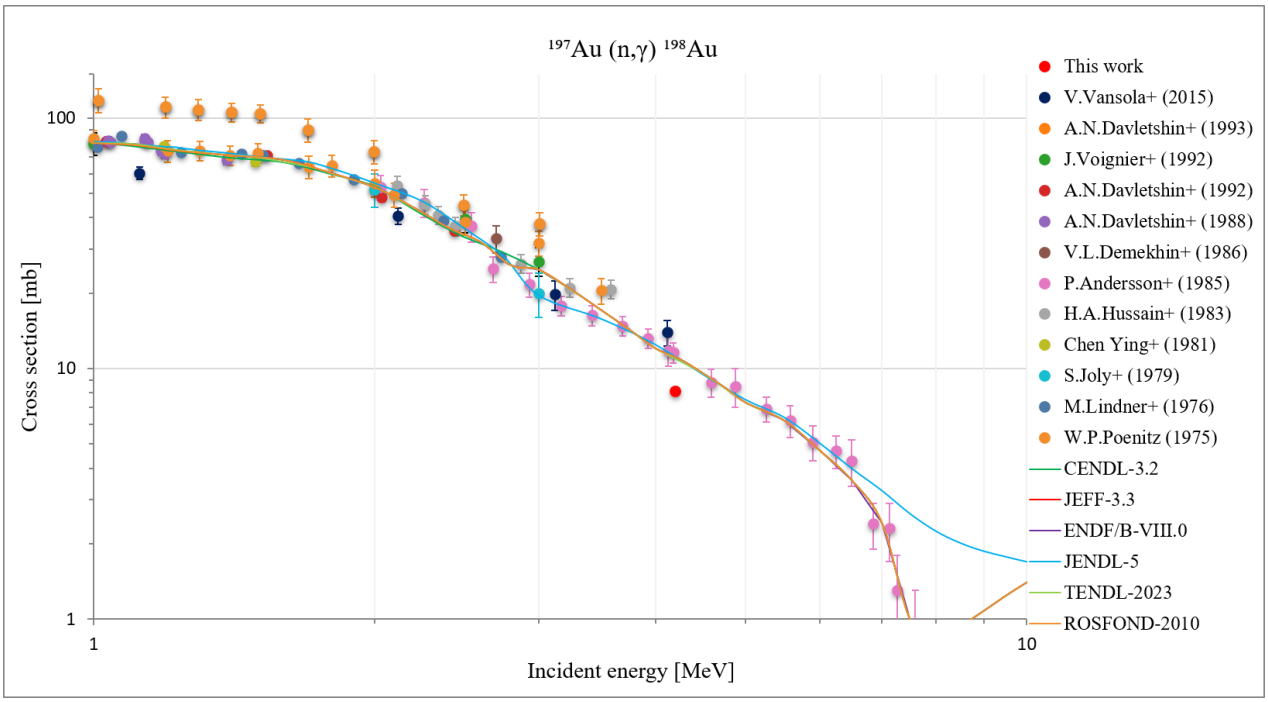

Figure 8 – Comparison between the experimental ^{197}Au(n,γ)^{198}Au cross-section value obtained in this work, EXFOR experimental data [8], and evaluated nuclear data libraries [9-14].

Since the evaluated-library data and the EXFOR measurements are generally tabulated on different energy grids, an interpolation procedure was applied to compare the datasets at the same neutron energies. For each EXFOR point, the two adjacent energy values in the evaluated dataset were selected. Linear-linear interpolation was used unless a different interpolation law was explicitly specified in the evaluated file. When the dataset prescribed log-log interpolation, the interpolation was performed in logarithmic energy and cross-section coordinates, consistently with the corresponding ENDF interpolation law [16].

For linear-linear interpolation, the interpolated library value was calculated as:

$$\sigma_{\mathrm{int}}(E_{\mathrm{EXFOR}}) = \sigma_{\mathrm{low}} + \frac{\sigma_{\mathrm{high}} - \sigma_{\mathrm{low}}}{E_{\mathrm{high}} - E_{\mathrm{low}}}(E_{\mathrm{EXFOR}} - E_{\mathrm{low}})$$

where E_{low} and E_{high} are the adjacent evaluated neutron-energy points, while $\sigma_{\mathrm{low}}$and $\sigma_{\mathrm{high}}$are the corresponding cross-section values. For datasets requiring log-log interpolation, the same linear relation was applied to $\ln(E)$and $\ln(\sigma)$. This preserves the interpolation law specified in the original evaluated dataset.

The relative difference between each interpolated library value and the corresponding EXFOR measurement was then calculated as:

$$\Delta_{\mathrm{rel}} = \frac{\sigma_{\mathrm{lib,int}} - \sigma_{\mathrm{EXFOR}}}{\sigma_{\mathrm{EXFOR}}} \times 100$$

With this convention, a positive value indicates that the evaluated library overestimates the corresponding EXFOR measurement, whereas a negative value indicates an underestimation. The interpolated values were then used for the point-by-point comparison with the EXFOR measurements. The complete comparison is reported in Appendix A, while a compact statistical summary is provided in Table 5.

	Mean relative difference [%]	**Mean absolute relative difference [%]**	**Median absolute relative difference [%]**
ENDF/B-VIII.0	-4.20	9.83	4.98
JEFF-3.3	-3.85	9.87	4.77
JENDL-5	0.66	13.36	4.43
TENDL-2023	-3.94	9.95	5.02
ROSFOND-2010	-3.85	9.87	4.77
CENDL-3.2	-4.21	10.38	6.10

Table 5 – Statistical summary of the relative differences between EXFOR data [8] and evaluated libraries for the $^{197}\mathrm{Au}(\mathrm{n},\gamma)^{198}\mathrm{Au}$ reaction [9-14].

The mean relative difference indicates the average bias of each evaluated library with respect to the EXFOR dataset, while the mean and median absolute relative differences quantify the overall deviation independently of the sign. Among the evaluated libraries, ENDF/B-VIII.0 shows the lowest

mean absolute relative difference, indicating the best average agreement with the EXFOR dataset. JEFF-3.3, ROSFOND-2010, and TENDL-2023 provide very similar results, with mean absolute deviations close to 10%. CENDL-3.2 shows a slightly larger deviation. JENDL-5 has the lowest median absolute relative difference, suggesting good agreement for many individual points, but its higher mean absolute relative difference indicates the presence of larger local deviations at some energies.

1.5.2 Comparison with TALYS Calculations

The experimental result was also compared with nuclear-reaction calculations performed through the TALYSworld online platform [17], which provides a web-based interface for running TALYS calculations. Different Level Density and Photon Strength Function models were selected in order to investigate the dependence of the calculated $^{197}Au(n,\gamma)^{198}Au$ cross section on the adopted nuclear-model inputs.

The Level Density model describes the number of nuclear states available at a given excitation energy and therefore influences the formation and statistical decay of the compound nucleus. The Photon Strength Function describes the average probability of gamma-ray emission during nuclear de-excitation. Since the $^{197}Au(n,\gamma)^{198}Au$ reaction proceeds through neutron capture followed by gamma emission, both model inputs can directly affect the calculated capture cross section [18]. A brief summary of the TALYS Level Density and Photon Strength Function options considered in this work is reported in Appendix B.

As shown in Figure 9, the different TALYSworld calculations lead to significantly different cross-section predictions, especially in the energy region of a few MeV. Among the model combinations considered, the experimental value obtained in this work lies closest to the LD2-based calculations, particularly the LD2–PSF1, LD2–PSF2, and LD2–PSF3 combinations. This indicates that the local agreement with the experimental point depends strongly on the selected Level Density model.

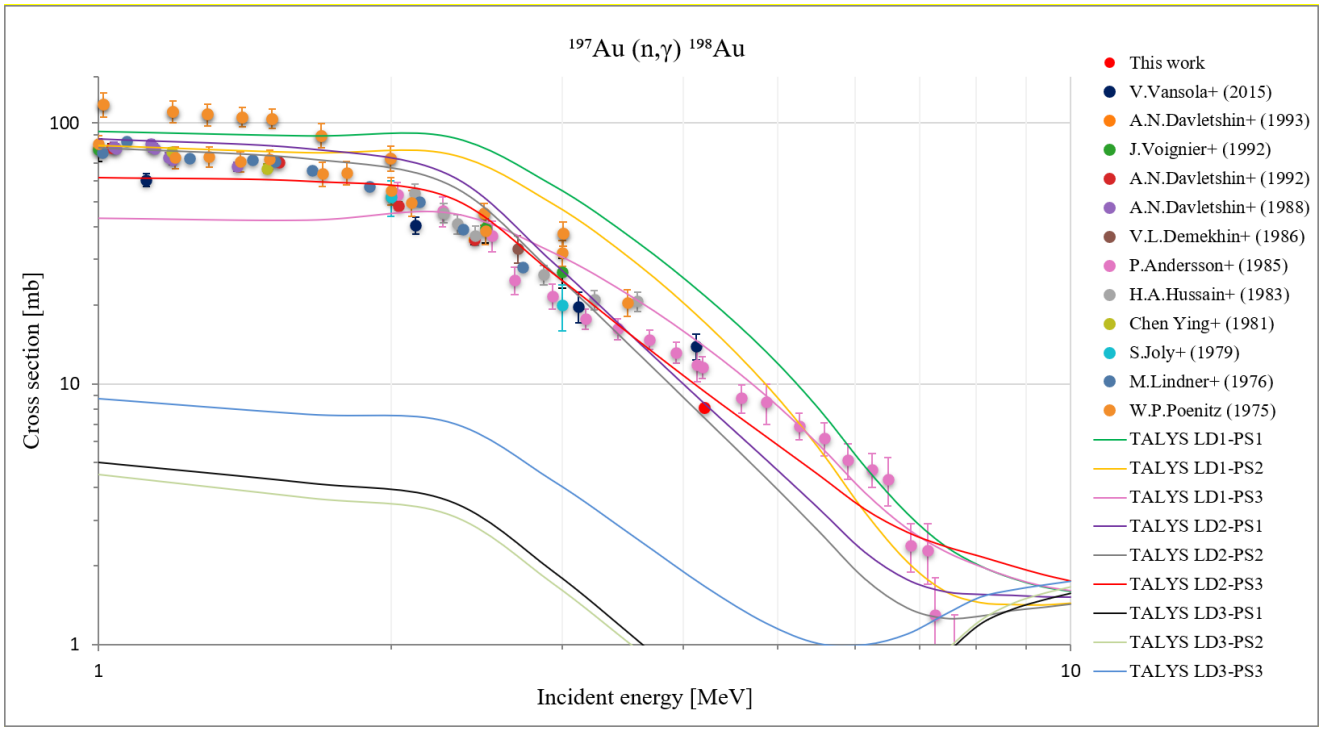

Figure 9 – Comparison between the experimental ^{197}Au(n,γ)^{198}Au cross section obtained in this work, the available EXFOR measurements [8], and TALYSworld calculations performed using different Level Density and Photon Strength Function models [17],[18].

The LD1-based calculations predict higher cross sections than the experimental value in the representative energy region, whereas the LD3-based calculations predict substantially lower values. The LD2-based curves therefore provide the closest local description of the present experimental result. However, this agreement should not be interpreted as a general validation of one specific TALYS model combination, since the complete set of calculations shows a considerable model spread.

The following local chi-square, empirical covariance, and sensitivity analyses provide a more complete quantitative assessment of this model dependence.

1.6 Statistical Analysis

1.6.1 Local Chi-square Analysis of TALYS Model Combinations

To quantitatively assess which TALYS model combination provides the closest agreement with the experimental cross-section value obtained in this work, a local chi-square analysis was performed. Unlike the empirical covariance analysis, which evaluates the spread among the TALYS predictions,

the chi-square analysis directly compares each TALYS curve with the experimental result at the energy of interest.

As discussed in Section 1.5.1, the experimental result was represented at a neutron energy of approximately 4.2 MeV, corresponding to the representative average energy adopted for the Am–Be source [15]. Since the TALYSworld energy grid did not contain a point exactly at 4.2 MeV, the closest available value, corresponding to 4.21 MeV, was used for the comparison.

For each TALYS model combination, the residual with respect to the experimental value was calculated as:

$$r_i = \sigma_{\mathrm{TALYS},i} - \sigma_{\mathrm{exp}}$$

where $\sigma_{\mathrm{TALYS},i}$ is the cross section predicted by the i-th TALYS model combination and $\sigma_{\mathrm{exp}}$is the experimental cross section obtained in this work. The residual was then normalized by the experimental uncertainty:

$$z_i = \frac{\sigma_{\mathrm{TALYS},i} - \sigma_{\mathrm{exp}}}{u_{\mathrm{exp}}}$$

The local chi-square contribution was then calculated as:

$$\chi_i^2 = \left(\frac{\sigma_{\mathrm{TALYS},i} - \sigma_{\mathrm{exp}}}{u_{\mathrm{exp}}} \right)^2$$

where $u_{\mathrm{exp}}$is the uncertainty associated with the experimental cross-section value. Since only one experimental point is considered, this analysis should be interpreted as a local agreement indicator rather than as a global goodness-of-fit test.

In this work, the experimental value used for the comparison was:

$$\sigma_{\mathrm{exp}} = 8.12 \pm 1.71 \text{ mb}$$

at approximately 4.2 MeV. The resulting local chi-square values are shown in Figure 10.

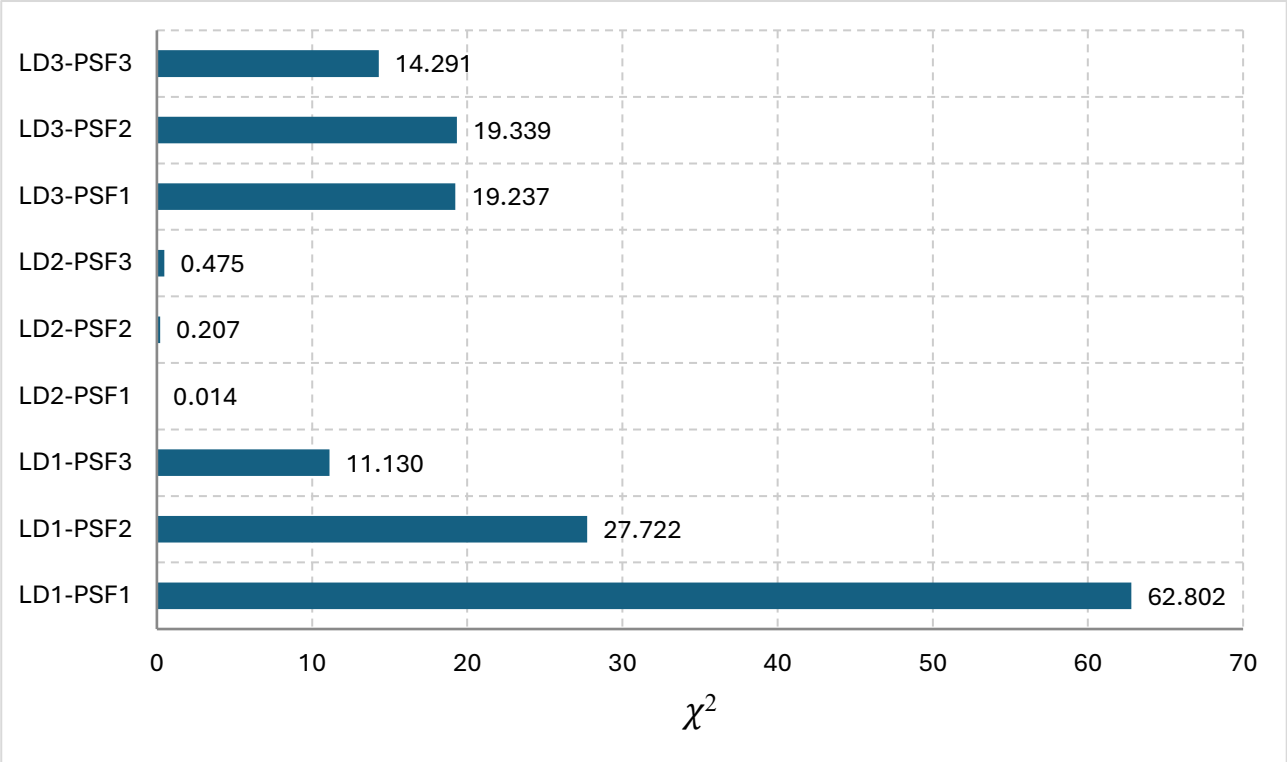

Figure 10 – Local chi-square comparison between the experimental $^{197}\mathrm{Au}(\mathrm{n},\gamma)^{198}\mathrm{Au}$ cross-section value and the TALYS model combinations at 4.21 MeV.

The lowest chi-square value is obtained for the LD2–PSF1 combination, with $\chi^2 \approx 0.014$. This means that, among the tested TALYSworld calculations, LD2–PSF1 is the closest to the experimental result at 4.21 MeV. The other LD2-based combinations also remain close to the measurement, with χ^2 values of approximately 0.207 for LD2–PSF2 and 0.475 for LD2–PSF3.

The LD1-based calculations give larger chi-square values because they predict cross sections higher than the experimental result in this energy region. The LD3-based calculations also deviate from the measurement, but in the opposite direction, since they predict much lower cross sections. At the representative Am–Be energy, the LD2-based TALYSworld calculations are the ones that reproduce most closely the experimental point.

Since only one experimental point is considered, this result should be interpreted only as a local agreement indicator. It should not be considered a global validation of the selected TALYS model combination over the full energy range.

1.6.2 Empirical Covariance Analysis of TALYS Model Predictions

To quantify the model spread associated with the selected nuclear-model options, an empirical covariance analysis was performed using the TALYSworld calculations generated by varying the Level Density and Photon Strength Function models [17],[18].

The analysis was based on nine model combinations, obtained by combining three Level Density models with three Photon Strength Function models. Each combination provides a different cross-section curve for the ^{197}Au(n,γ)^{198}Au reaction. Therefore, nine TALYSworld cross-section values were available at each incident neutron energy.

This procedure does not produce a formal evaluated nuclear-data covariance file. The calculated covariance describes only the empirical spread and energy-to-energy correlation generated by the selected TALYSworld model combinations. It should therefore be interpreted as a model-spread estimate rather than as a complete probabilistic evaluation of the theoretical uncertainty.

For each energy point, the mean TALYS cross section was calculated as:

$$\bar{\sigma}(E_i) = \frac{1}{N}\sum_{k=1}^{N} \sigma_k\,(E_i)$$

Where N=9 is the number of TALYS model combinations, and $\sigma_k(E_i)$is the cross section predicted by the k-th model at the energy E_i.

The deviation of each model from the mean value was then obtained as:

$$\Delta\sigma_k(E_i) = \sigma_k(E_i) - \bar{\sigma}(E_i)$$

The empirical covariance matrix was calculated as:

$$C_{ij} = \frac{1}{N-1}\sum_{k=1}^{N} \Delta\,\sigma_k(E_i)\Delta\sigma_k(E_j)$$

The diagonal terms of the covariance matrix represent the variance of the TALYS predictions at each energy. Therefore, the corresponding standard deviation was obtained as:

$$s(E_i) = \sqrt{C_{ii}}$$

This standard deviation was used to define the inner uncertainty band, corresponding to:

$$\bar{\sigma}(E_i) \pm s(E_i)$$

In addition, a full model envelope was calculated by taking the minimum and maximum TALYS predictions at each energy:

$$\sigma_{\min}(E_i) = \min[\sigma_k(E_i)]$$
$$\sigma_{\max}(E_i) = \max[\sigma_k(E_i)]$$

The resulting covariance band is shown in Figure 11. The solid line represents the mean TALYSworld prediction, the inner shaded region represents the mean ±1σ model uncertainty, and the outer shaded region represents the full minimum–maximum envelope.

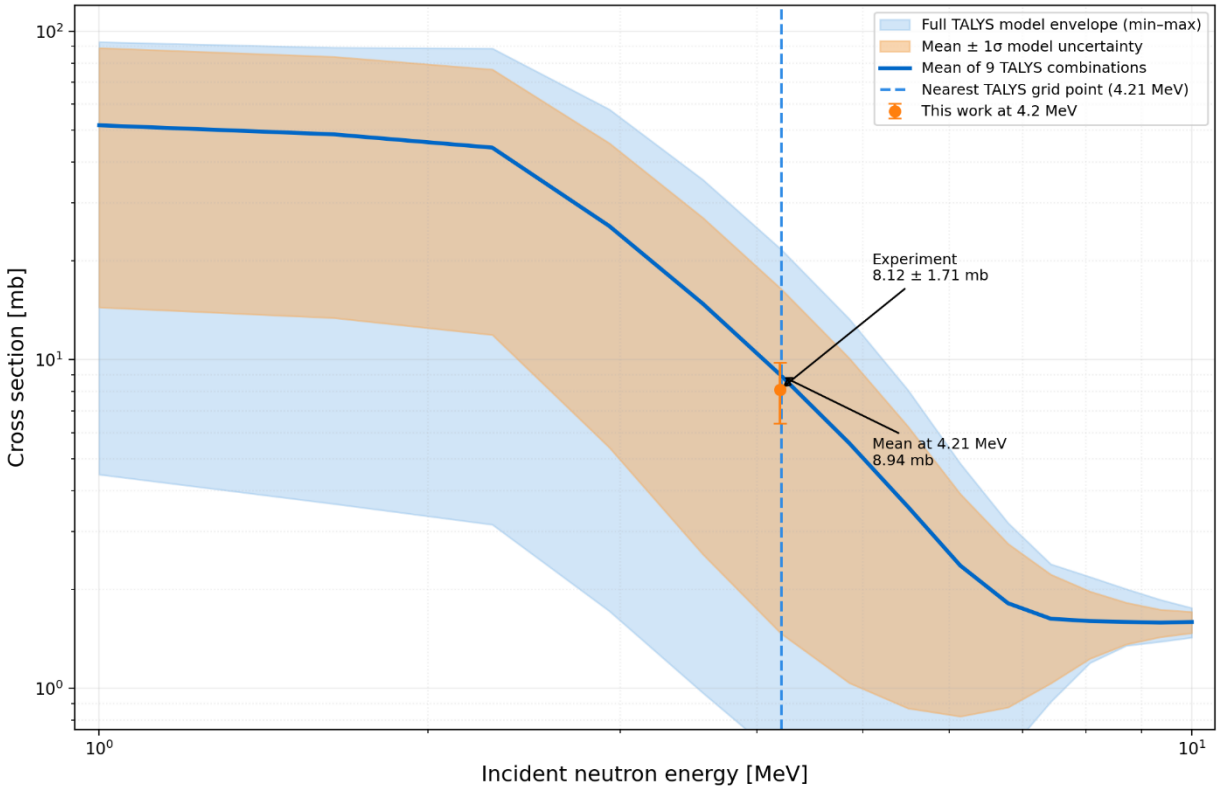

Figure 11 – Empirical model-spread representation for the ^{197}Au(n,γ)^{198}Au reaction, obtained from nine TALYSworld model combinations [17],[18] and compared with the experimental result obtained in this work at the representative neutron energy of approximately 4.2 MeV [15].

At the energy closest to the experimental value, namely 4.21 MeV, the mean TALYS cross section is approximately 8.94 mb, with a standard deviation of approximately 7.48 mb. This corresponds to a coefficient of variation of about 83.6%, showing that the TALYS prediction is strongly affected by the selected model combination in this energy region.

The experimental value obtained in this work is 8.12 ± 1.71 mb at approximately 4.2 MeV. This value is very close to the mean TALYS prediction at the nearest grid point, equal to approximately 8.94 mb, and lies within both the mean ±1σ model-spread band and the full TALYS model envelope. This indicates that the experimental result is consistent with the central region of the TALYSworld model spread at the representative Am–Be energy.

A relevant feature of Figure 11 is the asymmetric enlargement of the covariance band toward lower cross-section values. This behaviour is mainly associated with the three LD3-based calculations, which predict considerably lower values than the remaining TALYS combinations in the energy region of interest. To quantify this effect, the covariance analysis was repeated after excluding the LD3-based curves, while keeping only the six LD1- and LD2-based combinations. The comparison between the two cases is reported in Table 6.

	Mean TALYS [mb]	Std dev [mb]	CV [%]	Min–max envelope [mb]
With LD3	8.94	7.48	83.6	0.61–21.67
Without LD3	12.93	5.66	43.8	7.35–21.67

Table 6 – Effect of the LD3-based TALYS calculations on the covariance-band parameters at 4.21 MeV.

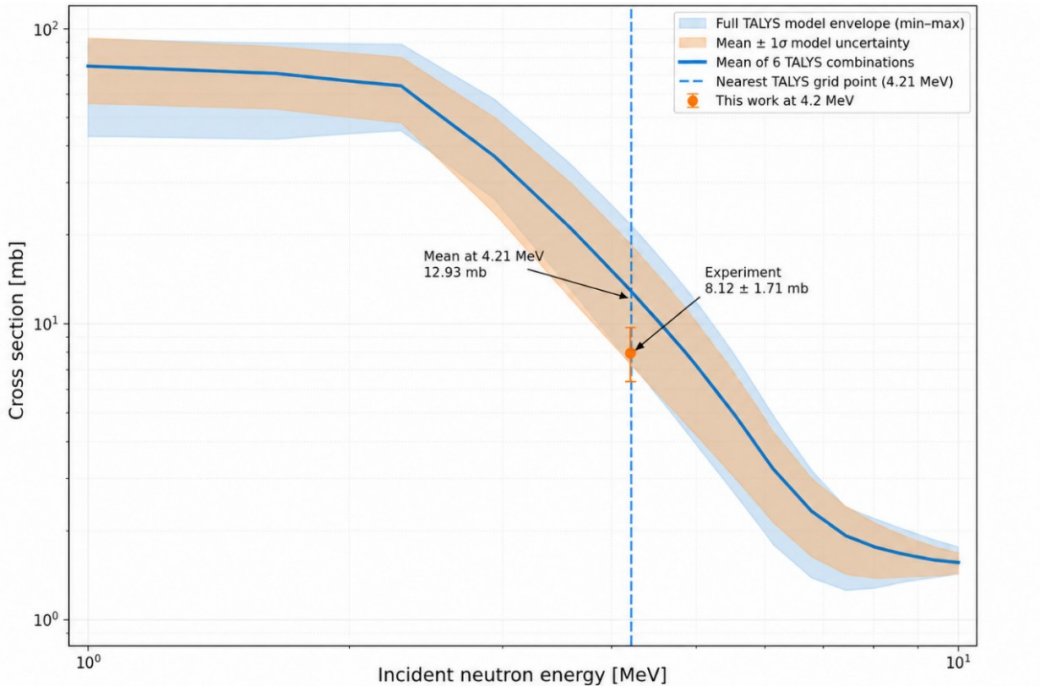

Figure 12 – Covariance band recalculated after excluding the LD3-based TALYS combinations.

After the exclusion of the LD3-based curves, the experimental point lies below the reduced mean TALYS prediction of 12.93 mb, but it remains within the reduced mean ±1σ band and inside the corresponding minimum–maximum envelope. This shows that the measurement is still compatible with the reduced TALYS model spread, although it is closer to the lower part of the reduced band than to its mean value. The exclusion of the LD3-based curves increases the mean TALYS prediction from 8.94 mb to 12.93 mb and reduces the coefficient of variation from 83.6% to 43.8%. At the same time, the upper boundary of the full model envelope remains unchanged, whereas the lower boundary shifts from 0.61 mb to 7.35 mb. This confirms that the LD3 combinations mainly affect the lower part of the envelope and are responsible for most of the enlarged model spread around the experimental energy.

Given the spread among the predictions, the comparison between the experimental result and the TALYSworld calculations should not be based exclusively on a single theoretical curve. The empirical covariance band provides a broader representation of the spread generated by the selected LD–PSF model combinations. In the complete nine-model ensemble, the experimental value is close to the mean TALYS prediction, while in the reduced six-model ensemble it remains within the uncertainty band but closer to its lower boundary. Nevertheless, these bands should be interpreted as empirical model-spread representations and not as formal confidence intervals.

1.6.3 Sensitivity Analysis of TALYS Model Inputs

To complement the covariance analysis, a sensitivity analysis was performed in order to identify which TALYS model input mainly controls the spread of the calculated ^{197}Au(n,γ)^{198}Au cross section. The analysis was based on the same nine TALYS calculations used for the covariance band, obtained by combining three Level Density models and three Photon Strength Function models [17],[18].

For each incident neutron energy, the nine cross-section values can be arranged in a 3x3 matrix:

$$\sigma_{ij}(E)$$

where i identifies the Level Density model and j identifies the Photon Strength Function model. In the present analysis, m = 3 Level Density models and n = 3 Photon Strength Function models were considered.

The average cross section at each energy was calculated as:

$$\bar{\sigma}(E) = \frac{1}{mn} \sum_{i=1}^{m} \sum_{j=1}^{n} \sigma_{ij}\,(E)$$

The mean cross section associated with each Level Density model was calculated as:

$$\bar{\sigma}_{i\cdot}(E) = \frac{1}{n} \sum_{j=1}^{n} \sigma_{ij}\,(E)$$

while the mean associated with each Photon Strength Function model was calculated as:

$$\bar{\sigma}_{\cdot j}(E) = \frac{1}{m} \sum_{i=1}^{m} \sigma_{ij}\,(E)$$

The total variability of the TALYS predictions was then expressed as:

$$SS_{\text{tot}} = \sum_{i=1}^{m} \sum_{j=1}^{n} \left[\sigma_{ij}(E) - \bar{\sigma}(E)\right]^2$$

This total variability was decomposed into three contributions: the contribution of the Level Density model, the contribution of the Photon Strength Function model, and the interaction between the two model choices.

The contribution associated with the Level Density model was calculated as:

$$SS_{\text{LD}}(E) = n \sum_{i=1}^{m} [\bar{\sigma}_{i\cdot}(E) - \bar{\sigma}(E)]^2$$

The contribution associated with the Photon Strength Function model was calculated as:

$$SS_{\text{PSF}}(E) = m \sum_{j=1}^{n} \left[\bar{\sigma}_{\cdot j}(E) - \bar{\sigma}(E)\right]^2$$

The non-additive interaction between the two model choices was calculated as:

$$SS_{\mathrm{int}}(E) = \sum_{i=1}^{m} \sum_{j=1}^{n} \left[\sigma_{ij}(E) - \bar{\sigma}_{i\cdot}(E) - \bar{\sigma}_{\cdot j}(E) + \bar{\sigma}(E)\right]^2$$

The decomposition therefore satisfies:

$$SS_{\mathrm{tot}} = SS_{\mathrm{LD}} + SS_{\mathrm{PSF}} + SS_{\mathrm{int}}$$

The corresponding relative contributions were calculated as:

$$C_{\mathrm{LD}} = \frac{SS_{\mathrm{LD}}}{SS_{\mathrm{tot}}} \times 100$$

$$C_{\mathrm{PSF}} = \frac{SS_{\mathrm{PSF}}}{SS_{\mathrm{tot}}} \times 100$$

$$C_{\mathrm{int}} = \frac{SS_{\mathrm{int}}}{SS_{\mathrm{tot}}} \times 100$$

where C_{LD}, C_{PSF}, and C_{int} represent the percentage contributions of the Level Density model, the Photon Strength Function model, and their interaction, respectively.

Only one deterministic TALYSworld prediction was available for each LD–PSF combination. Consequently, no independent residual-error term or statistical significance test could be estimated. The remaining non-additive contribution was assigned to the LD–PSF interaction. The resulting percentages should therefore be interpreted as a descriptive decomposition of the model spread generated by the selected options, rather than as probabilistic sensitivity indices or formal uncertainty estimates [19].

Around the experimental energy, the closest TALYSworld grid point is 4.21 MeV. Table 7 reports the nine calculated cross sections at this energy, together with the LD and PSF averages. The large variation among the LD averages, from 17.54 mb for LD1 to 0.97 mb for LD3, shows that the Level Density model has the strongest effect.

	PSF1 [mb]	PSF2 [mb]	PSF3 [mb]	**LD average [mb]**
LD1 [mb]	21.67	17.12	13.82	**17.54**
LD2 [mb]	8.33	7.35	9.30	**8.32**
LD3 [mb]	0.63	0.61	1.66	**0.97**
PSF average [mb]	**10.21**	**8.36**	**8.26**	—

Table 7 – TALYS cross sections at 4.21 MeV grouped by Level Density and Photon Strength Function models.

This is confirmed by the variance decomposition, which gives $C_{\mathrm{LD}} = 92.5\%$, $C_{\mathrm{PSF}} = 1.6\%$, and $C_{\mathrm{int}} = 5.9\%$. Therefore, near the experimental energy, the TALYS spread is mainly controlled by the Level Density model. The Photon Strength Function has only a minor influence in this region, while the interaction term remains limited.

The energy dependence of the sensitivity contributions is shown in Figure 13.

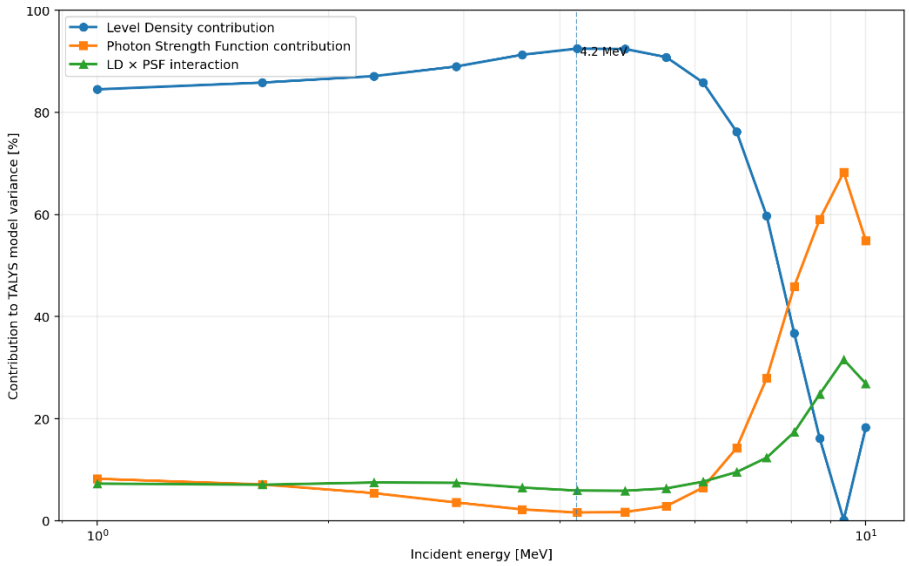

Figure 13 – Relative contributions of Level Density, Photon Strength Function, and LD–PSF interaction to the variance of the TALYS predictions for ^{197}Au(n,γ)^{198}Au.

The Level Density contribution dominates from 1 MeV up to approximately 7 MeV, including the region of the present measurement. This confirms that the widening of the covariance band around 4.2 MeV is mainly caused by the different Level Density prescriptions, especially by the LD3-based curves, which predict significantly lower cross sections than the other TALYS combinations.

At higher energies, the contribution of the Photon Strength Function increases and becomes dominant above approximately 8 MeV. However, this region is farther from the experimental energy considered in this work. Consequently, for the interpretation of the present experimental result, the most relevant model input is the Level Density model.

The sensitivity analysis also confirms and explains the behaviour already observed in the covariance band. While the covariance analysis shows the total model spread, the sensitivity analysis identifies its origin. In the energy region of interest, the uncertainty of the TALYS prediction is mainly associated with the adopted Level Density model, whereas the Photon Strength Function plays a secondary role.

Chapter 2 – Nuclear Data Analysis of Neutron Radiative Capture Reactions

2.1 Introduction

This part of the thesis extends the analysis from the experimental activation study of ^{197}Au to a broader nuclear-data investigation of neutron radiative-capture reactions. The first three target nuclides selected were ^{51}V, ^{103}Rh, and ^{209}Bi, representing the light-, medium-, and heavy-mass regions, respectively. Rhodium and bismuth are naturally monoisotopic, while natural vanadium is overwhelmingly composed of ^{51}V, with an isotopic abundance of approximately 99.75% [20]. These characteristics minimize ambiguities associated with contributions from different target isotopes.

The ^{232}Th(n,γ)^{233}Th reaction was subsequently included to extend the analysis to the actinide region and to provide a more complete investigation of heavy nuclei. Natural thorium is overwhelmingly dominated by ^{232}Th, with a representative isotopic abundance of approximately 99.98% [20].

The four reactions, ^{51}V(n,γ)^{52}V, ^{103}Rh(n,γ)^{104}Rh, ^{209}Bi(n,γ)^{210}Bi, and ^{232}Th(n,γ)^{233}Th, were therefore analysed in the neutron energy range from 1 to 30 MeV. Together, these reactions cover different regions of the Chart of Nuclides. Neutron radiative-capture data across these mass regions are relevant to neutron dosimetry, activation analysis, fusion-related applications, reactor safety, reactor physics, and nuclear fuel-cycle studies [21], [22].

The selection of these reactions was also motivated by the fact that the same delayed activation procedure used for gold would have some limitations here. These isotopes have less favourable decay characteristics, such as very short half-lives, weak or low-energy gamma emissions, or the absence of a suitable delayed gamma line. For this reason, as discussed in Section 2.2, these reactions were investigated through an analytical comparison of available experimental data, evaluated libraries, and TALYSworld calculations.

The objective of this part is to compare experimental cross-section data from the EXFOR database [8] with evaluated nuclear data libraries [9-14] and with nuclear-reaction calculations performed through the TALYSworld platform [17]. TALYSworld calculations were also performed using different Level Density and Photon Strength Function models to examine their effect on the calculated capture cross sections [18]. The empirical covariance and sensitivity methods introduced for the gold case were then applied to these simulations to quantify the model spread and identify its main sources.

2.2 Decay Behaviour of the Selected Reaction Products

A direct experimental extension of the activation and delayed gamma-spectrometry procedure adopted for ^{197}Au was not pursued for the four reactions considered in this part. The neutron-capture products of ^{51}V, ^{103}Rh, ^{209}Bi, and ^{232}Th exhibit decay characteristics that differ substantially from those of ^{198}Au, making the same laboratory procedure unsuitable or requiring a specifically redesigned experimental approach.

For vanadium and rhodium, the principal limitation is associated with the short half-lives of the activation products, which would require rapid transfer from the irradiation position to the detector and immediate acquisition of the gamma spectrum. In the rhodium case, the possible population of both ground and metastable states introduces an additional complication. For bismuth, the difficulty is instead related to the absence of a suitable gamma emission from the dominant decay branch and to the extremely long half-life of the metastable product. For thorium, the main experimental difficulty is associated with the low-energy and relatively weak gamma emission of ^{233}Th, rather than with an impractically short half-life.

For these reasons, the ^{197}Au activation experiment was not repeated for the four additional reactions. Their analysis was instead based on available EXFOR measurements, evaluated nuclear data libraries, and TALYSworld calculations.

The decay data for the corresponding capture products were obtained from the NuDat database [2] and are discussed below to clarify the experimental limitations associated with each case.

Reaction	Decay data					
	Parent nucleus	Daughter nucleus	Decay mode	Half-life	Representative Eγ (keV)	Iγ (%)
^{51}V(n,γ)^{52}V	$^{52}_{23}$V	$^{52}_{24}$Cr	β- (100%)	**3.743 m (5)**	1434.06 (1)	100

Table 8. Decay data relevant to the ^{51}V(n,γ)^{52}V reaction

The ^{51}V(n,γ)^{52}V reaction produces ^{52}V, which decays by β^- emission to ^{52}Cr. From a spectrometric point of view, this activation product is particularly favourable, since it emits a highly intense gamma ray at 1434.06 keV with an emission probability of 100%. However, its half-life of only 3.743 min represents a major experimental limitation. Such rapid decay would require the activated sample to be transferred to the detector and measured almost immediately after irradiation, with a very well-controlled and reproducible timing sequence. Even short delays between the end of irradiation and

the beginning of the acquisition would lead to a significant reduction in the available activity and would increase the sensitivity of the result to timing uncertainties.

Despite its favourable gamma emission, the short half-life of ^{52}V makes the same experimental procedure impractical unless the activated sample is transferred to the detector and measured much more rapidly.

Reaction	Decay data					
	Parent nucleus	Daughter nucleus	Decay mode	Half-life	Representative Eγ (keV)	Iγ (%)
^{103}Rh(n,γ)^{104}Rh	$^{104}_{45}$Rh	$^{104}_{46}$Pd	β- (99.55%)	**42.3 s (4)**	555.81 (4)	**2**
		$^{104}_{44}$Ru	ε (0.45%)		358.12 (15)	**0.016**
^{103}Rh(n,γ)^{104m}Rh	$^{104m}_{45}$Rh	$^{104}_{46}$Pd	β- (0.13%)	**4.34 m (3)**	555.81 (4)	**0.13**
		$^{104}_{45}$Rh	IT (99.87%)		**51.4225 (15)**	48.277

Table 9. Decay data relevant to the neutron-capture products of ^{103}Rh

The neutron-capture reaction on ^{103}Rh may populate both the ground state ^{104}Rh and the metastable state ^{104m}Rh. The ground state is particularly critical from an experimental point of view, since its half-life is only 42.3 s. This decay time is too short to allow a reliable off-line gamma-spectrum acquisition using the same transfer procedure and detection setup adopted for the gold measurement. In addition, although the 555.81 keV gamma line can be used as a reference for the main β^- decay branch, its emission intensity is only 2.0%, while the gamma line associated with the electron-capture branch is even weaker.

The metastable state ^{104m}Rh has a longer, but still short, half-life of 4.34 min. Its decay is mainly governed by isomeric transition to ^{104}Rh, with an intense gamma emission at 51.4225 keV. However, this low-energy line is experimentally challenging because attenuation in the sample, source holder, detector window, and surrounding materials may reduce the detected signal. In addition, the detector response and spectral background in this energy region may complicate reliable peak identification and net peak-area determination.

Therefore, the rhodium case would require a dedicated measurement protocol, with rapid and reproducible timing, careful treatment of the possible population of both nuclear states, and specific attention to low-energy gamma detection.

Reaction	Decay data					
	Parent nucleus	Daughter nucleus	Decay mode	Half-life	Representative Eγ (keV)	Iγ (%)
^{209}Bi(n,γ)^{210}Bi	$^{210}_{83}$Bi	$^{206}_{81}$Tl	α (1.32 x 10^{-4} %)	5.012 d (5)	-	-
		$^{210}_{84}$Po	β- (100%)		-	-
^{209}Bi(n,γ)^{210m}Bi	$^{210m}_{83}$Bi	$^{206}_{81}$Tl	α (100%)	**3.04 x 10^6 y (6)**	265.6 (5)	52

Table 10. Decay data relevant to the neutron-capture products of ^{209}Bi

The ^{209}Bi(n,γ) reaction presents a different experimental limitation compared with vanadium and rhodium. The ground-state product ^{210}Bi has a half-life of 5.012 d, which would be compatible with delayed measurements. However, its dominant decay branch is a β^- decay to ^{210}Po, with no suitable representative gamma emission available for the same type of gamma-spectrometric analysis. The very weak α-decay branch of ^{210}Bi is negligible from the point of view of the present approach.

A further complication is given by the possible formation of the metastable state ^{210m}Bi. Although this state is associated with gamma emissions, including the 265.6 keV line, its half-life is extremely long, equal to 3.04×10^6y. This makes the activity produced over a realistic irradiation time very limited and incompatible with a practical delayed gamma measurement. Therefore, in the bismuth case, the main difficulty is not related to a rapid decay, but rather to the absence of a useful gamma line for the main ^{210}Bi decay branch and to the extremely long-lived nature of the metastable product.

These decay characteristics help explain why the available experimental information for this reaction is limited and why some of the measurements reported in EXFOR rely on prompt-gamma techniques rather than on conventional delayed gamma spectrometry [8]. The role of this experimental technique is discussed further in Section 2.7.1.

Reaction	Decay data					
	Parent nucleus	Daughter nucleus	Decay mode	Half-life	Representative Eγ (keV)	Iγ (%)
$^{232}Th(n,\gamma)^{233}Th$	$^{233}_{90}Th$	$^{233}_{91}Pa$	β- (100%)	21.83 m (4)	**86.50 (1)**	**1.843**

Table 11. Decay data relevant to the $^{232}Th(n,\gamma)^{233}Th$ reaction

The $^{232}Th(n,\gamma)^{233}Th$ reaction produces ^{233}Th, which decays by β^- emission to ^{233}Pa with a half-life of 21.83 min. This half-life is compatible with delayed gamma-spectrometric measurements, provided that the transfer and acquisition times are accurately controlled. The main limitations are associated with the representative gamma line at 86.50 keV, which has an emission intensity of only 1.843%. Its low energy makes the measurement more sensitive to attenuation, self-absorption, detector-efficiency calibration, and background contributions. However, a dedicated experimental extension was not considered necessary in the present work because a comparatively extensive EXFOR dataset is already available for this reaction [8].

2.3 Data Collection

Experimental cross-section data for the selected neutron radiative-capture reactions were retrieved from the EXFOR database [8]. For each target, the experimental points retained between 1 and 30 MeV were collected together with the uncertainties reported in EXFOR, when available. The data were converted to consistent units, using MeV for the incident neutron energy and mb for the cross section.

The evaluated nuclear data were obtained from ENDF/B-VIII.0, JEFF-3.3, JENDL-5, TENDL-2023, ROSFOND-2010, and CENDL-3.2, depending on their availability for each reaction [9-14].

The theoretical analysis was performed using the TALYSworld platform [17], with the same model-variation strategy applied to all selected targets. Six Level Density models were combined with three Photon Strength Function models, resulting in eighteen TALYS model combinations for each reaction. The model options were selected according to the definitions reported in the TALYS manual [18]. The same model ensemble was used for the direct comparison with the experimental data and for the subsequent empirical covariance and sensitivity analyses.

2.4 Data Processing and Interpolation

The point-by-point comparisons between EXFOR measurements and evaluated nuclear data libraries were performed using the same interpolation and relative-difference procedure introduced in Section 1.5.1. For each experimental neutron energy, the corresponding evaluated-library cross section was obtained using the interpolation law specified in the original dataset [16].

The same procedure and sign convention were applied consistently to the ^{51}V, ^{103}Rh, ^{209}Bi, and ^{232}Th case studies. With this convention, a positive relative difference indicates that the evaluated library overestimates the corresponding EXFOR measurement, whereas a negative value indicates an underestimation. The complete point-by-point results are reported in Appendix A, while the principal statistical indicators are summarized in the corresponding case-study sections.

Throughout the following analyses, the empirical covariance bands are used exclusively to represent the model spread generated by the selected TALYSworld LD–PSF combinations. They should not be interpreted as formal confidence intervals or as evaluated nuclear-data covariance files.

2.5 Case Study of ^{51}V

The first reaction examined in Part 2 is $^{51}V(n,\gamma)^{52}V$. Experimental measurements, evaluated nuclear data libraries, and TALYSworld calculations were compared over the 1–30 MeV range. Particular attention was given to the dispersion of the experimental data near 14–15 MeV and to the influence of the Photon Strength Function on the TALYS predictions.

2.5.1 Comparison between EXFOR Data and Evaluated Libraries

The experimental cross-section data for the $^{51}V(n,\gamma)^{52}V$ reaction were retrieved from the EXFOR database [8] and compared with five evaluated nuclear data libraries: ENDF/B-VIII.0, JEFF-3.3, JENDL-5, TENDL-2023, and ROSFOND-2010 [9-13]. CENDL-3.2 was not included for this reaction because no corresponding evaluated dataset was available from the National Nuclear Data Center database at the time of data collection.

Since the EXFOR points and the evaluated libraries are generally tabulated on different energy grids, each library was interpolated at the experimental EXFOR energies according to the procedure described in Section 2.4.

The EXFOR measurements generally decrease with increasing neutron energy, but the agreement among the different datasets is not uniform. The dispersion becomes particularly evident around 14–15 MeV. In this region, the value reported by Majumder and Mitra is clearly separated from the other measurements: the authors reported a cross section of 0.07 mb at 14.8 MeV, with an uncertainty of 10% [23]. This value is markedly lower than both the other experimental measurements available in the same energy region and the evaluated-library predictions. The EXFOR history indicates that the value was revised from 0.49 mb to 0.07 mb according to the 1977 publication [8]. The revised value was retained in the present analysis, but its influence must be considered when interpreting the percentage-based statistical indicators.

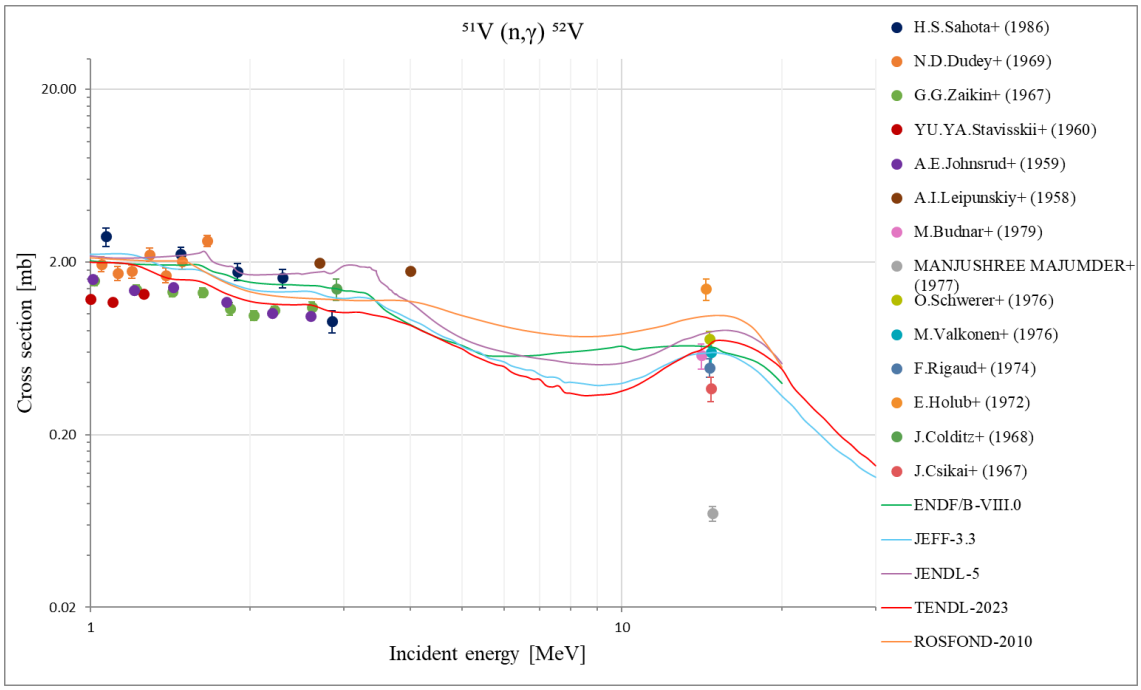

Figure 14 – Comparison between EXFOR experimental measurements [8] and evaluated nuclear data libraries [9-13] for the $^{51}V(n,\gamma)^{52}V$ reaction in the 1–30 MeV neutron-energy range.

The evaluated libraries follow the general downward trend of the cross section, although their agreement with the measurements varies across the energy range. Most of the low-energy EXFOR points remain relatively close to the evaluated curves. Around 14–15 MeV, however, the larger experimental dispersion makes the comparison more dependent on the individual dataset considered: library performance in this region cannot therefore be judged from a single measurement alone.

The relative differences calculated according to Section 2.4 are reported in Appendix A. Table 12 summarizes the mean relative difference and the mean and median absolute relative differences.

	Mean relative difference [%]	**Mean absolute relative difference [%]**	**Median absolute relative difference [%]**
ENDF/B-VIII.0	39.82	52.65	32.83
JEFF-3.3	36.46	51.43	32.57
JENDL-5	61.84	68.82	44.40
TENDL-2023	28.19	48.10	21.13
ROSFOND-2010	59.86	71.21	34.73

Table 12 – Statistical summary of the relative differences between experimental data retrieved from the EXFOR database [8] and evaluated nuclear data libraries [9-13] for the $^{51}V(n,\gamma)^{52}V$ reaction.

Among the five evaluated libraries, TENDL-2023 gives the lowest mean absolute relative difference, 48.10%, and the lowest median absolute relative difference, 21.13%. Nevertheless, the mean-based indicators are strongly influenced by the particularly low value of 0.07 mb reported by Majumder and Mitra at 14.8 MeV [23].

Since the relative difference is normalized by the experimental cross section, the small denominator associated with this measurement produces very large percentage deviations for all the evaluated libraries. The median absolute relative difference is less sensitive to this individual point and therefore provides a more representative indication of the typical deviation within the remaining dataset. All the evaluated libraries show positive mean relative differences, indicating an average tendency to overestimate the selected EXFOR measurements. JEFF-3.3 and ENDF/B-VIII.0 provide comparable results, while JENDL-5 and ROSFOND-2010 show larger average deviations.

2.5.2 Comparison with TALYS Calculations

The experimental data retrieved from EXFOR [8] were also compared with calculations performed through the TALYSworld platform [17] by varying the Level Density and Photon Strength Function models. These model choices affect the density of available compound-nucleus states and the description of gamma-ray de-excitation, respectively [18].

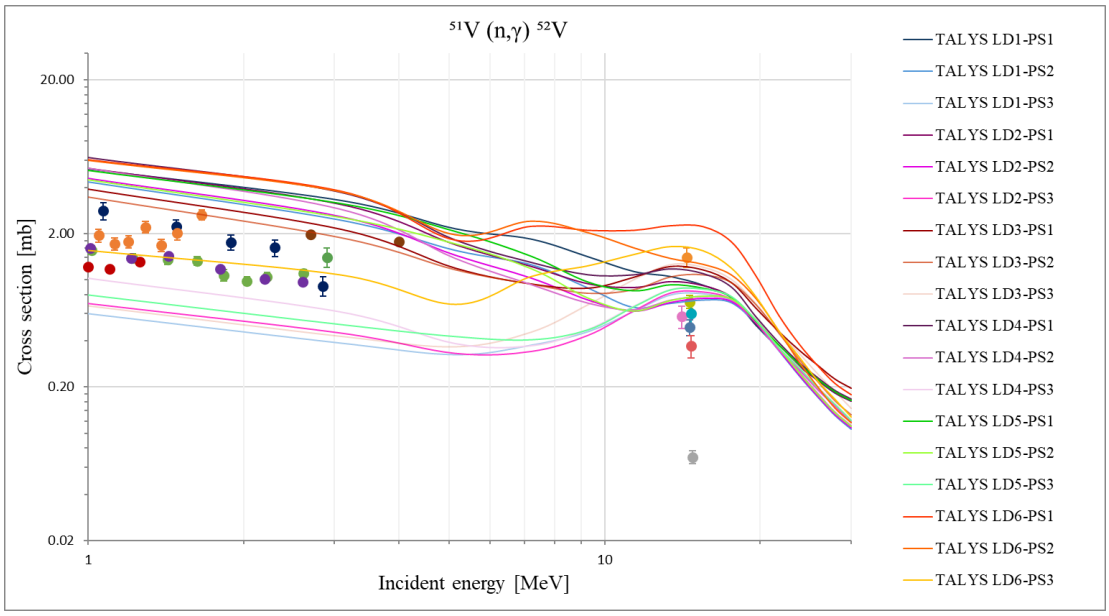

Figure 15 – Comparison between experimental data retrieved from the EXFOR database [8] and TALYSworld calculations for the $^{51}V(n,\gamma)^{52}V$ reaction, obtained by varying the Level Density and Photon Strength Function models [17], [18].

The TALYSworld calculations show a non-negligible dependence on the selected LD–PSF combination. Although the different curves reproduce the general decrease of the experimental cross section with increasing neutron energy, they exhibit a significant spread in magnitude. In particular, the PSF3-based calculations generally predict lower cross sections than the other PSF options over a large part of the investigated energy range.

No single calculation reproduces all the available EXFOR datasets over the complete energy interval. Nevertheless, the PSF3-based curves are closer to several of the lower experimental values and generally define the lower part of the calculated model range. Among the tested combinations, LD6–PSF3 and LD4–PSF3 provide comparatively close qualitative representations of the general experimental trend, although the apparent agreement remains dependent on the energy region and dataset considered.

The isolated value of 0.07 mb reported by Majumder and Mitra at 14.8 MeV lies substantially below the complete TALYSworld prediction range [23]. Therefore, this individual measurement was retained in the graphical comparison but was not used as the principal criterion for selecting the model combination that best represents the broader experimental trend.

2.5.3 Restricted Chi-square Analysis of the LD6–PSF3 TALYS Calculation

No experimental cross section was obtained for ^{51}V in the present work. The quantitative comparison was therefore limited to a subset of the EXFOR measurements, using LD6–PSF3 as the reference TALYS curve because it follows the low-energy experimental trend more closely than most of the other combinations.

Two low-energy EXFOR datasets were initially considered because of their proximity to the LD6–PSF3 curve. However, one of them does not report pointwise experimental uncertainties. Since the chi-square calculation requires an uncertainty for each measurement, the quantitative comparison was restricted to the eight points of the Zaikin dataset for which uncertainties are available in EXFOR [24].

The LD6–PSF3 curve was interpolated at the eight Zaikin energies, and the chi-square was calculated using the definition given in Section 1.6.1.

The resulting total chi-square was: $\chi^2 = 59.48$.

For N = 8 experimental points, corresponding to: $\chi^2/N = 7.44$.

The value of χ^2/N remains considerably higher than unity, indicating that the deviations between the LD6–PSF3 calculation and the selected experimental measurements are generally larger than would be expected from the reported pointwise uncertainties alone.

Because no model parameters were fitted in this analysis and the experimental subset was selected on the basis of its proximity to the calculated trend, χ^2/N should not be interpreted as a formal reduced chi-square or as a global goodness-of-fit statistic. It is used here only as a local weighted-discrepancy indicator.

LD6–PSF3 remains one of the closest descriptions of the Zaikin dataset, but the deviations at individual energies are still too large for this result to be treated as a validation over the full 1–30 MeV interval.

2.5.4 Empirical Covariance Analysis of TALYS Model Predictions for ^{51}V

For ^{51}V, the model spread was evaluated from the same eighteen LD–PSF combinations used in the direct TALYSworld comparison [17], [18]. The mean cross section, empirical standard deviation, and minimum–maximum envelope were calculated on the common energy grid and then compared with the measurements available in EXFOR [8].

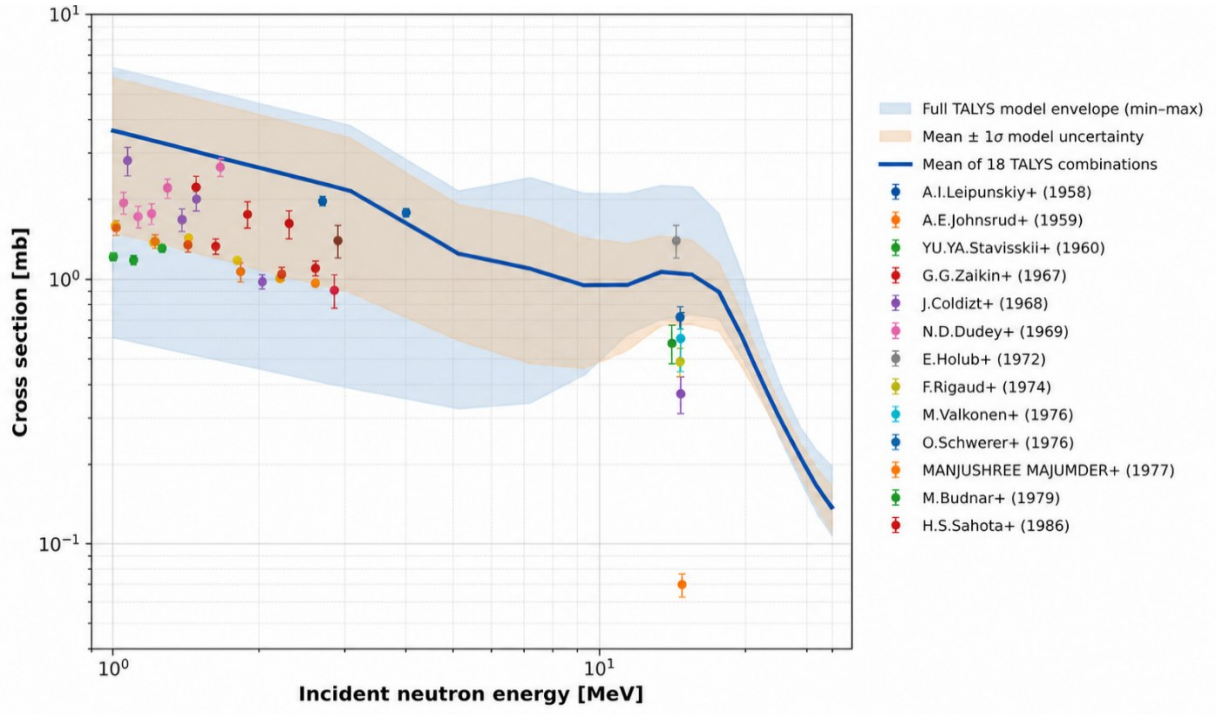

Figure 16 – Empirical TALYS covariance band for the $^{51}V(n,\gamma)^{52}V$ reaction, obtained from eighteen TALYS model combinations and compared with EXFOR experimental data.

As shown in Figure 16, the TALYS calculations reproduce the general decreasing trend of the $^{51}\mathrm{V}(n,\gamma)^{52}\mathrm{V}$ cross section with increasing neutron energy. The EXFOR data in the low-energy region, approximately between 1 and 4 MeV, are mostly located within the TALYS model envelope, although several points lie below the mean TALYS prediction. This indicates that the average TALYS calculation tends to slightly overestimate part of the experimental dataset in this region, while the full model spread still provides a reasonable coverage of the available measurements.

At 1 MeV, the mean TALYS cross section is approximately 3.64 mb, with a standard deviation of about 2.14 mb. This corresponds to a coefficient of variation of approximately 58.6%, showing that the calculated cross section is strongly affected by the selected nuclear model combination. As the neutron energy increases, the relative spread gradually decreases: the coefficient of variation is about 53% at 5.14 MeV, 35% at 15.5 MeV, and around 20% at 30 MeV. Therefore, the model dependence is more pronounced in the lower-energy region and becomes less significant at higher neutron energies.

A relevant feature of the covariance band is the role of the Photon Strength Function model. In contrast to the gold case, where the lower part of the envelope was mainly affected by a specific Level Density model, for ^{51}V the lowest TALYS predictions are generally associated with the PSF3-based calculations. For almost all Level Density models, the use of Photon Strength Function 3 shifts the calculated cross section toward lower values. As a consequence, the PSF3 curves strongly influence the lower boundary of the full model envelope and contribute significantly to the asymmetric shape of the covariance band. The same tendency was already visible in the direct TALYSworld comparison, where the PSF3-based curves were closer to several of the lower EXFOR values. The covariance band shows, however, that this agreement occurs within a relatively broad model range.

In the energy region around 14–15 MeV, the EXFOR measurements show a comparatively large dispersion. Most of the experimental points remain relatively close to the TALYSworld model envelope, whereas the value of 0.07 mb reported by Majumder and Mitra at 14.8 MeV lies substantially below both the other measurements and the complete calculated range [23]. The EXFOR history documents that this value was revised from 0.49 mb to 0.07 mb according to the original publication [8]. The revised value was retained for completeness, but it should not be regarded as representative of the general experimental trend in this energy region.

This measurement does not affect the numerical calculation of the empirical covariance band, since the band is derived exclusively from the eighteen TALYSworld calculations. Nevertheless, it strongly influences the visual comparison between the experimental measurements and the model envelope.

The band should therefore be interpreted as a representation of the calculated model spread and not as an interval expected to contain every individual experimental point.

For vanadium, the largest model dependence is found in the low-energy region and is mainly associated with the selected Photon Strength Function. The complete envelope shows the range generated by the investigated TALYSworld options, but it is not a formal confidence interval or a complete estimate of theoretical uncertainty.

2.5.5 Sensitivity Analysis of TALYS Model Inputs for ^{51}V

For the vanadium reaction, the eighteen TALYSworld calculations were analysed using the two-factor sum-of-squares decomposition described in Section 1.6.3 [17-19]. The discussion below considers how the contributions of the Level Density model, the Photon Strength Function model, and their interaction vary with neutron energy.

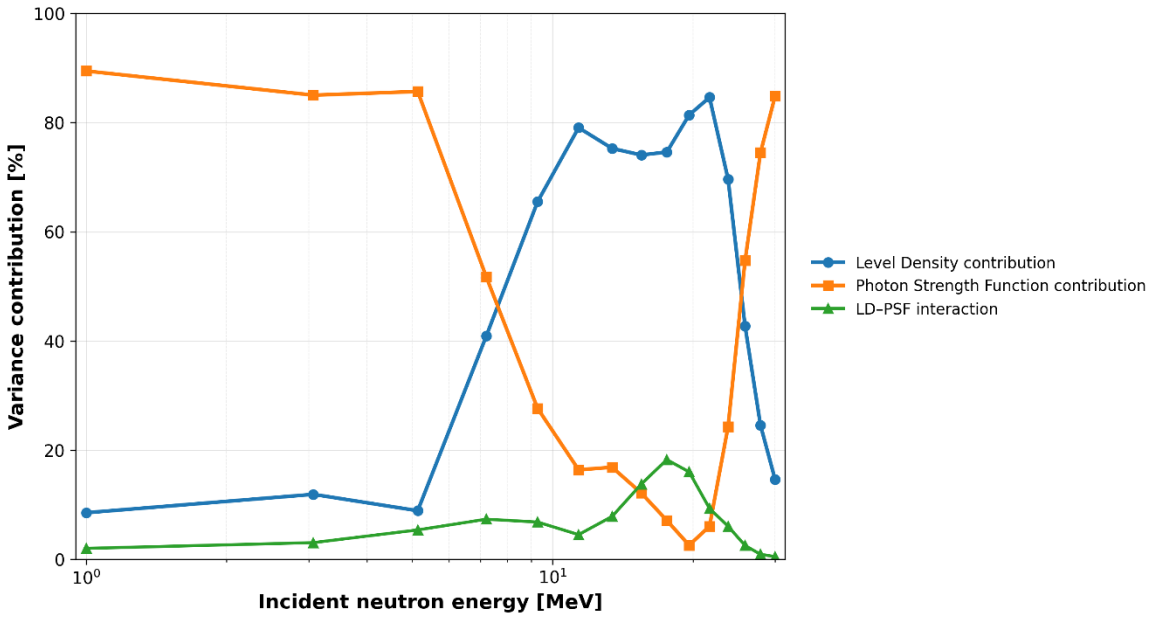

Figure 17 – Relative contributions of the Level Density model, Photon Strength Function model, and LD–PSF interaction to the total spread of the 18 TALYSworld predictions for the ^{51}V(n,γ)^{52}V reaction [17-19].

For the ^{51}V(n,γ)^{52}V reaction, the Photon Strength Function is the dominant source of model variability in the low-energy region. Between 1 and 5 MeV, the PSF contribution remains very high, with values of about 89.5% at 1 MeV, 85.0% at 3.07 MeV, and 85.7% at 5.14 MeV. This confirms what was

already observed in the covariance analysis: the lower TALYS curves are mainly associated with the PSF3-based calculations, which strongly affect the shape of the model envelope in this energy range.

At approximately 7 MeV, the sensitivity becomes more balanced. At 7.21 MeV, the PSF contribution is still the largest one, around 51.7%, but the Level Density contribution increases significantly to about 40.9%. This indicates a transition region in which both nuclear model inputs influence the calculated capture cross section.

From approximately 9 MeV to 24 MeV, the Level Density model becomes the dominant source of variability. In this region, the LD contribution reaches values between about 65% and 85%, with a maximum of approximately 84.6% at 21.71 MeV. Therefore, while the low-energy behaviour is mainly controlled by the Photon Strength Function, the intermediate-energy region is more sensitive to the selected Level Density model.

At higher energies, above approximately 25 MeV, the Photon Strength Function contribution increases again and becomes dominant. In particular, the PSF contribution rises to about 54.8% at 25.87 MeV, 74.5% at 27.92 MeV, and 84.8% at 30 MeV. This suggests that the sensitivity of the $^{51}V(n,\gamma)^{52}V$ reaction is not controlled by a single model input over the entire energy range, but changes depending on the incident neutron energy.

The interaction term remains generally smaller than the two main effects, although it is not negligible in some regions. Its largest values occur in the intermediate-energy range, reaching about 18.3% at 17.58 MeV and 16.0% at 19.63 MeV. This means that, in this region, part of the TALYS spread cannot be attributed independently to either LD or PSF alone, but results from the combined effect of the two model choices.

The sensitivity analysis helps explain the shape of the covariance band. At low neutron energies, the TALYS envelope is mainly controlled by the Photon Strength Function, particularly by the PSF3-based curves, while the Level Density model becomes more influential in the intermediate-energy region. The origin of the model spread therefore changes across the investigated energy range rather than being controlled by a single model input.

2.6 Case Study of ^{103}Rh

The second reaction considered is ^{103}Rh(n,γ)^{104}Rh. The comparison with evaluated libraries and TALYSworld calculations is complicated by the pronounced dispersion of the EXFOR measurements around 14–15 MeV, where a cluster of relatively high cross-section values lies well above the remaining experimental points. Another distinctive feature of this case is the large TALYS model spread produced by the LD3–PSF1 and LD3–PSF2 combinations.

2.6.1 Comparison between EXFOR Data and Evaluated Libraries

The experimental cross-section data for the ^{103}Rh(n,γ)^{104}Rh reaction were retrieved from the EXFOR database [8] and compared with six evaluated nuclear data libraries: ENDF/B-VIII.0, JEFF-3.3, JENDL-5, TENDL-2023, ROSFOND-2010, and CENDL-3.2 [9-14].

Since the EXFOR measurements and the evaluated-library data are tabulated on different energy grids, each evaluated curve was interpolated at the corresponding experimental energies using the procedure described in Section 2.4.

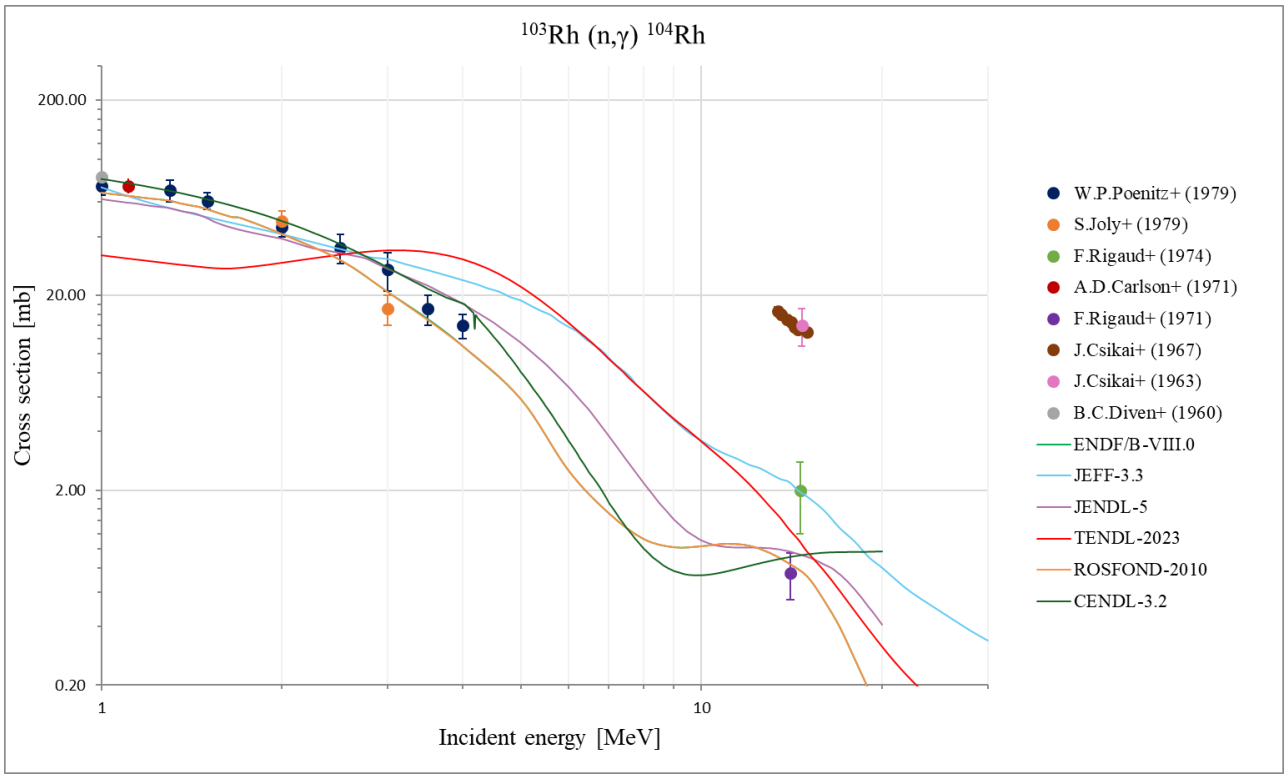

Figure 18 – Comparison between experimental data retrieved from the EXFOR database [8] and evaluated nuclear data libraries [9-14] for the ^{103}Rh(n,γ)^{104}Rh reaction in the 1–30 MeV neutron-energy range.

Between 1 and 4 MeV, the experimental cross section decreases fairly regularly, and the evaluated libraries reproduce this trend despite some differences in magnitude. The situation is less uniform around 14–15 MeV, where a cluster of experimental values lies substantially above both the evaluated-library curves and the other measurements available in the same energy region. These high cross-section values come from two early studies led by Csikai, published in 1963 and 1967 [25], [26]. Given both the age of these measurements and the lack of independent confirmation from different research groups, this cluster should be interpreted with caution. The statistical comparison is therefore strongly influenced by this group of measurements.

The point-by-point relative differences were calculated using the interpolated library values. The full results are reported in Appendix A, while Table 13 gives the main statistical indicators.

	Mean relative difference [%]	**Mean absolute relative difference [%]**	**Median absolute relative difference [%]**
ENDF/B-VIII.0	-42.34	45.38	21.93
JEFF-3.3	-16.20	53.80	64.60
JENDL-5	-35.40	49.27	30.67
TENDL-2023	-33.64	70.53	78.31
ROSFOND-2010	-42.14	45.18	21.93
CENDL-3.2	-29.01	44.25	28.25

Table 13 – Statistical summary of the relative differences between experimental data retrieved from the EXFOR database [8] and evaluated nuclear data libraries [9-14] for the ^{103}Rh(n,γ)^{104}Rh reaction.

CENDL-3.2 gives the lowest mean absolute relative difference, 44.25%, while ENDF/B-VIII.0 and ROSFOND-2010 share the lowest median absolute relative difference, 21.93%. The three libraries therefore show comparable overall performance when the complete EXFOR dataset is considered.

JEFF-3.3 has the smallest magnitude of the mean relative difference, but its considerably larger absolute indicators show that this low average bias results partly from compensating positive and negative deviations. TENDL-2023 presents the largest mean absolute and median absolute relative differences among the considered evaluations.

All six libraries have negative mean relative differences, indicating an average tendency to underestimate the selected EXFOR measurements. However, this result is strongly influenced by the cluster of high experimental values around 14–15 MeV.

2.6.2 Comparison with TALYS Calculations

Figure 19 compares the EXFOR measurements [8] with eighteen TALYSworld calculations obtained using different Level Density and Photon Strength Function models [17], [18].

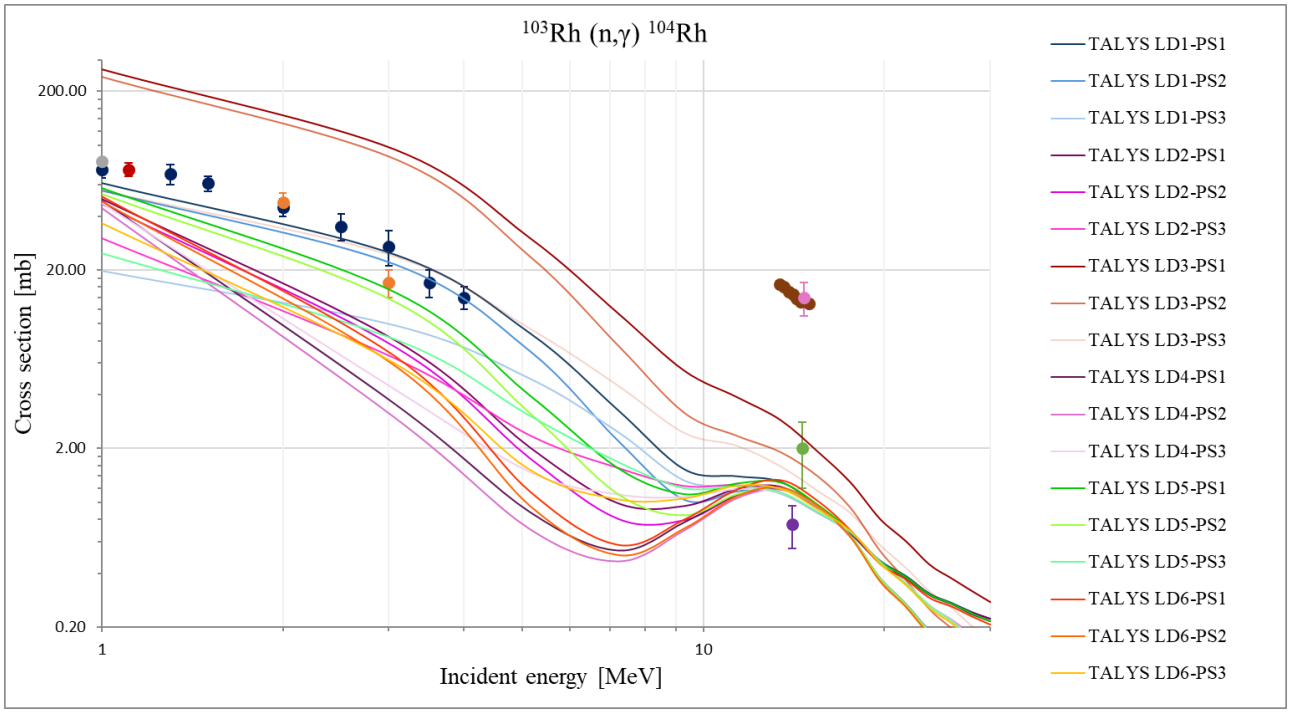

Figure 19 – Comparison between EXFOR data [8] and TALYSworld calculations for the ^{103}Rh(n,γ)^{104}Rh reaction, obtained using different Level Density and Photon Strength Function models [17], [18].

The most evident feature of the TALYSworld comparison is the wide separation among the LD–PSF combinations, especially at low and intermediate neutron energies. Despite this spread, most curves reproduce the general decrease of the capture cross section with increasing energy.

The LD3–PSF1 and LD3–PSF2 calculations predict substantially higher cross sections than the remaining model combinations below approximately 10 MeV. These two curves therefore strongly affect the upper part of the calculated model range and the mean prediction obtained from the complete eighteen-model ensemble.

In the low-energy region, the measurements reported by Poenitz provide a relatively coherent decreasing trend [27]. Within the 1–4 MeV interval considered in the present analysis, the LD1–PSF1 calculation gives one of the closest qualitative representations of the Poenitz dataset. This model combination was therefore selected for the restricted chi-square analysis presented in Section 2.6.3.

The comparison becomes more difficult to understand around 14–15 MeV. The high cross-section measurements reported by Csikai and co-workers [25], [26] lie above the complete TALYSworld range, while the lower values available at similar energies are closer to the calculations. The apparent level of agreement therefore depends strongly on which experimental dataset is considered.

For the rhodium reaction, the model spread is largely influenced by the high LD3–PSF1 and LD3–PSF2 predictions. The LD1–PSF1 calculation is examined locally against the Poenitz dataset in the following restricted chi-square analysis, while all eighteen TALYSworld calculations are retained for the covariance and sensitivity analyses.

2.6.3 Restricted Chi-square Analysis of the LD1–PSF1 TALYS Calculation

For the rhodium case, the restricted chi-square comparison was based on the LD1–PSF1 calculation and the low-energy measurements reported by Poenitz [27]. This TALYSworld combination was selected because it follows the experimental trend between 1 and 4 MeV more closely than most of the other tested models.

The quantitative comparison was restricted to eight Poenitz measurements between 1 and 4 MeV for which pointwise experimental uncertainties are available in EXFOR [8]. Restricting the analysis to a single experimental dataset avoids combining measurements obtained by different authors under different experimental conditions.

The LD1–PSF1 curve was interpolated at the eight experimental energies, and the chi-square was calculated according to the definition given in Section 1.6.1. The resulting total chi-square was:

$$\chi^2 = 11.42$$

for $N = 8$ experimental points, corresponding to:

$$\frac{\chi^2}{N} = 1.43$$

The value of χ^2/N is moderately higher than unity, showing that some differences remain between the LD1–PSF1 calculation and the Poenitz measurements when the reported uncertainties are used as weights. Even so, LD1–PSF1 gives a reasonably close description of the low-energy trend.

No model parameters were fitted during this comparison, and both the experimental subset and the TALYSworld combination were selected after examining the graphical agreement. For this reason, χ^2/N is used here only as a local weighted-discrepancy indicator, not as a formal reduced chi-square or a validation of the model over the full 1–30 MeV range.

2.6.4 Empirical Covariance Analysis of TALYS Model Predictions for ^{103}Rh

For rhodium, the covariance band was constructed from all eighteen TALYSworld calculations obtained from the six Level Density and three Photon Strength Function models [17], [18]. The mean cross section, empirical standard deviation, and minimum–maximum range were evaluated on the common energy grid and compared with the EXFOR measurements [8].

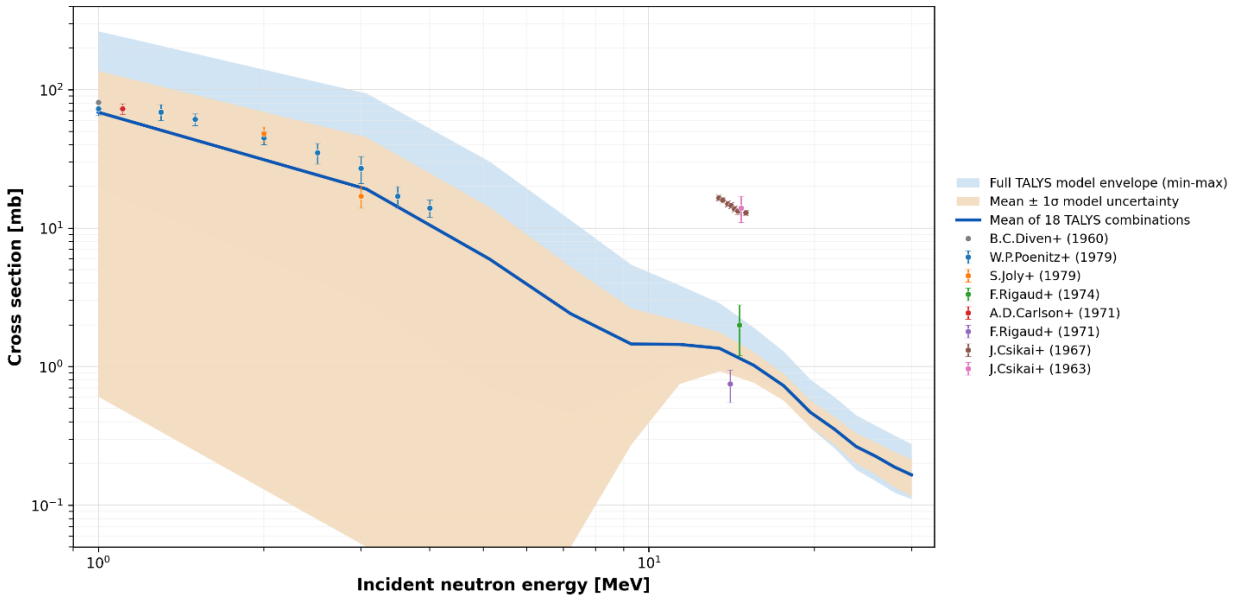

Figure 20 – Empirical model-spread representation for the ^{103}Rh(n,γ)^{104}Rh reaction, obtained from eighteen TALYSworld LD–PSF combinations [17], [18] and compared with experimental data retrieved from EXFOR [8].

The mean TALYSworld prediction decreases progressively over the investigated energy range, from approximately 68.7 mb at 1 MeV to 0.17 mb at 30 MeV. However, both the complete model envelope and the mean ±1σ model-spread band are particularly broad in the low- and intermediate-energy regions.

The relative model spread is especially large between approximately 1 and 7 MeV. The coefficient of variation is about 99.1% at 1 MeV, increases to 137.4% at 3.07 MeV, and remains similarly high, at 137.2%, at 5.14 MeV. At 7.21 MeV, it is still above 118%. These values show that the calculated cross section in this energy region is strongly dependent on the selected LD–PSF combination.

The broad model envelope is mainly caused by the LD3–PSF1 and LD3–PSF2 calculations, which predict substantially higher cross sections than the remaining model combinations. At 1 MeV, for example, the complete ensemble spans from approximately 19.8 mb to 264.5 mb. The upper boundary is therefore controlled by these two LD3-based calculations, which also strongly affect the mean prediction and empirical standard deviation.

The effect of these high predictions is also visible in the mean ±1σ band. At 3.07, 5.14, and 7.21 MeV, the calculated lower boundary becomes formally negative because the empirical standard deviation exceeds the mean prediction. This mathematical result does not imply physically negative cross sections. Instead, it indicates that the arithmetic mean ±1σ representation is not well suited to describing the strongly asymmetric model distribution in this energy region.

Since negative values cannot be represented on the logarithmic vertical axis, the corresponding lower boundary is not directly visible in the figure. The complete model envelope should therefore be considered together with the numerical covariance parameters. Overall, the full-model representation describes the complete spread generated by the selected TALYSworld options, but it should not be interpreted as a formal confidence interval or as a compact representation of the central behaviour of most calculations.

Because LD3–PSF1 and LD3–PSF2 control much of the upper part of the low-energy envelope, the covariance band was recalculated without these two curves. The resulting representation is based on the remaining sixteen TALYSworld combinations and is shown in Figure 21.

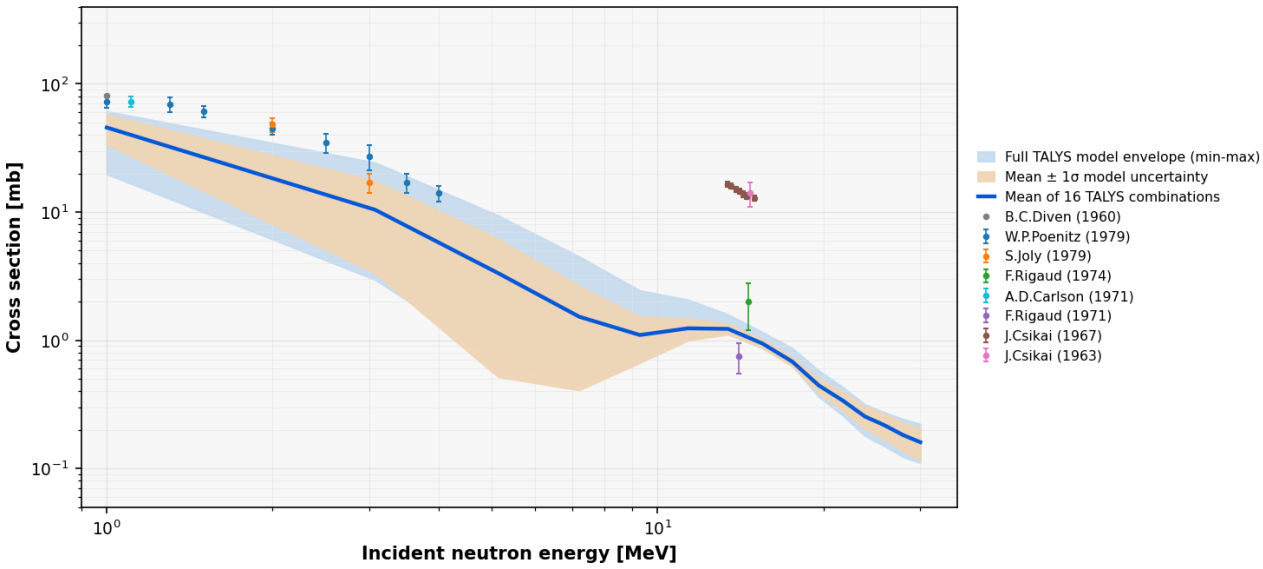

Figure 21 – Reduced empirical model-spread representation for the ^{103}Rh(n,γ)^{104}Rh reaction, recalculated using sixteen TALYSworld combinations after excluding LD3–PSF1 and LD3–PSF2 [17], [18]. Experimental measurements were retrieved from EXFOR [8].

The reduced model-spread band is significantly narrower, particularly below approximately 10 MeV. At 1 MeV, the mean cross section decreases from 68.7 mb to 45.7 mb, while the empirical standard deviation decreases from 68.1 mb to 11.9 mb. Consequently, the coefficient of variation is reduced from 99.1% to 26.1%.

A substantial reduction is also observed at 3.07 MeV, where the coefficient of variation decreases from 137.4% to 67.9%, as well as at 5.14 MeV. These changes confirm that LD3–PSF1 and LD3–PSF2 are primarily responsible for the exceptionally broad model spread in the low-energy region.

The effect of their exclusion becomes progressively less pronounced as the neutron energy increases. At 9.29 MeV, the coefficient of variation decreases from 81.1% to 39.0%, while at 15.5 MeV it decreases from 24.9% to 7.2%. Above approximately 20 MeV, the difference between the complete and reduced model ensembles becomes comparatively small. The two excluded calculations therefore mainly affect the low- and intermediate-energy regions.

The narrower band makes the comparison with the experimental data easier to interpret. The low-energy measurements reported by Poenitz [27] generally remain above the reduced TALYSworld mean, although several points fall within or close to the minimum–maximum range. At 14–15 MeV, the measurements reported by Csikai and co-workers [25], [26] still lie well above the calculated range, while the lower experimental values at similar energies are closer to the TALYSworld predictions.

Therefore, excluding LD3–PSF1 and LD3–PSF2 substantially reduces the calculated spread but does not eliminate all discrepancies between the TALYSworld predictions and the experimental database. These discrepancies reflect both the dependence of the calculations on the selected nuclear-model options and the dispersion among the available experimental measurements.

The comparison between the two bands shows that LD3–PSF1 and LD3–PSF2 are mainly responsible for the exceptionally large model spread observed for the ^{103}Rh(n,γ)^{104}Rh reaction. Once these two combinations are excluded, the band becomes considerably narrower and the mean prediction better represents the central group of the remaining TALYSworld calculations. Nevertheless, the reduced band remains an empirical representation of the investigated model spread and should not be interpreted as a formal uncertainty or confidence interval.

2.6.5 Sensitivity Analysis of TALYS Model Inputs for ^{103}Rh

The eighteen TALYSworld calculations for the ^{103}Rh(n,γ)^{104}Rh reaction were examined using the two-factor sum-of-squares method described in Section 1.6.3 [17-19]. The analysis separates the contributions of the Level Density model, the Photon Strength Function model, and their interaction as a function of neutron energy.

The Level Density model is the dominant source of TALYSworld model spread over most of the investigated energy range, from 1 MeV to approximately 20 MeV.

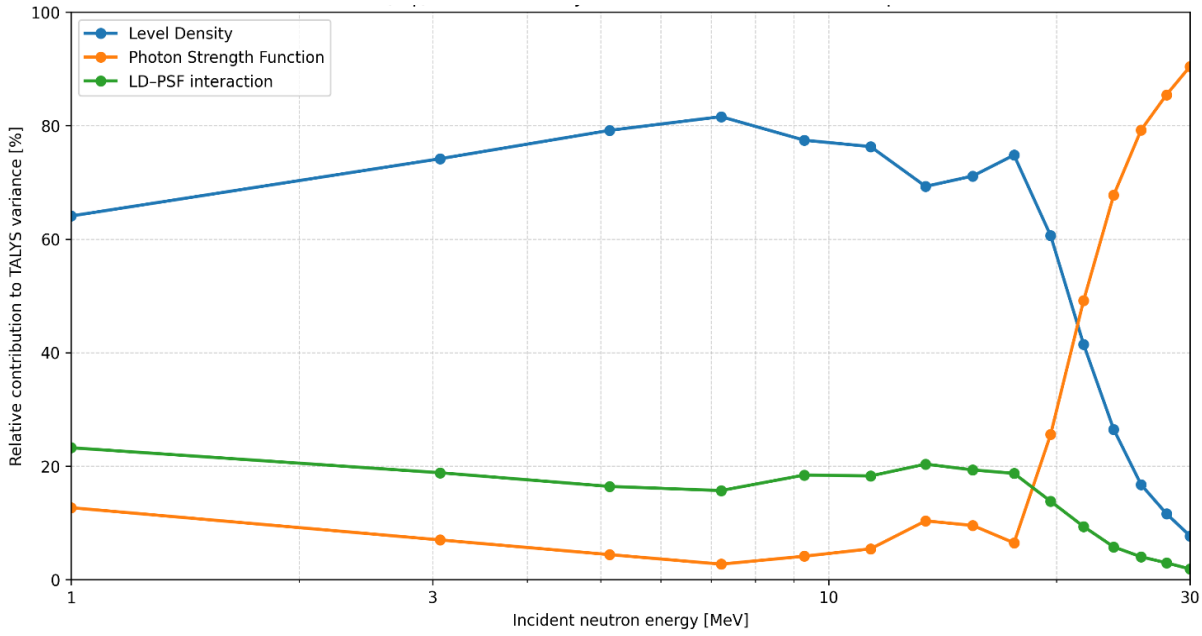

Figure 22 – Relative contributions of the Level Density model, Photon Strength Function model, and LD–PSF interaction to the total spread of the eighteen TALYSworld predictions for the ^{103}Rh(n,γ)^{104}Rh reaction [17-19].

At 1 MeV, the LD contribution accounts for approximately 64.1% of the total sum of squares, whereas the Photon Strength Function contribution is about 12.7%. The dominance of the Level Density model becomes more pronounced between approximately 3 and 17 MeV, where its contribution generally ranges from about 69% to 82%, reaching a maximum of approximately 81.6% at 7.21 MeV. Therefore, the differences among the TALYSworld predictions in this energy interval are mainly controlled by the selected Level Density prescription.

The Photon Strength Function contribution remains comparatively limited throughout the low- and intermediate-energy regions, generally below 11% up to approximately 17.6 MeV. Its influence then increases markedly above 20 MeV. At 21.71 MeV, the PSF contribution reaches approximately 49.2%, compared with 41.5% for the LD contribution. The Photon Strength Function becomes progressively dominant at higher energies, contributing approximately 67.8% at 23.79 MeV, 79.3% at 25.86 MeV, and 90.4% at 30 MeV.

The LD–PSF interaction is not negligible in the low- and intermediate-energy regions. It contributes approximately 23.2% at 1 MeV and generally remains between about 16% and 20% over much of the energy range below 20 MeV. This indicates that part of the calculated spread cannot be attributed independently to either LD or PSF alone, but results from the combined effect of the two model choices. At higher energies, the interaction contribution progressively decreases and falls below approximately 6% above 24 MeV.

Finally, the source of the TALYSworld spread changes with neutron energy. The Level Density model governs most of the variability up to approximately 20 MeV, while the Photon Strength Function becomes progressively more influential at higher energies and dominates above about 22 MeV.

2.7 Case Study of ^{209}Bi

The third case study concerns the ^{209}Bi(n,γ)^{210}Bi reaction, selected as representative of the heavy-mass region among the neutron radiative-capture reactions considered in this work. Experimental measurements retrieved from EXFOR were compared with evaluated nuclear data libraries and with TALYSworld calculations obtained by varying the Level Density and Photon Strength Function models [8], [17], [18].

Within the investigated 1–30 MeV neutron-energy range, the experimental database retained for this reaction is considerably more limited than those available for the vanadium and rhodium cases [8]. This limited availability is consistent with the experimental difficulties associated with the decay properties discussed in Section 2.2. The ground-state product ^{210}Bi does not provide a suitable representative delayed gamma emission for the activation procedure adopted in the gold experiment, while the metastable state ^{210m}Bi has an extremely long half-life [2].

The experimental measurements retained in the present analysis were therefore obtained using prompt-gamma techniques rather than conventional delayed gamma spectrometry. The following sections compare these measurements with evaluated nuclear data libraries and TALYSworld calculations and examine the agreement and model dependence through restricted chi-square, empirical covariance, and sensitivity analyses.

2.7.1 Experimental Data and Prompt-Gamma Measurements

The experimental cross-section data for the ^{209}Bi(n,γ)^{210}Bi reaction were retrieved from the EXFOR database [8]. Only measurements within the 1–30 MeV neutron-energy range were retained in order to maintain the same interval adopted for the other reactions considered in this work.

The selected dataset consists of four low-energy measurements reported by Voignier et al. [28], together with one measurement reported by Budnar et al. at 14.1 MeV [29]. Consequently, only five experimental cross-section values were retained for the present bismuth analysis.

A conventional delayed activation measurement requires the target to be irradiated and subsequently transferred to a detector, where radiation emitted by the decay of the activation product is measured. This procedure is most suitable when the reaction product has a practical half-life and emits a sufficiently intense and identifiable delayed gamma ray.

For the bismuth reaction, the ground-state product ^{210}Bi has a half-life compatible with delayed measurement, but its dominant β^- decay does not provide a suitable representative gamma line for the same type of gamma-spectrometric procedure adopted for ^{198}Au. The metastable product ^{210m}Bi is

associated with gamma emissions, but its extremely long half-life makes the activity induced during a realistic irradiation period impractically low [2].

The measurements retained in this work were instead obtained using prompt-gamma spectrometry. In this method, the detected photons are emitted during the rapid de-excitation of the compound nucleus following neutron capture, rather than during the later radioactive decay of the activation product. The gamma radiation is therefore measured during irradiation, in direct association with the neutron-capture event [30].

Prompt-gamma analysis is particularly valuable when neutron capture does not produce a radionuclide with suitable delayed gamma emissions. However, it requires a dedicated in-beam experimental configuration. Reliable results depend on the characterization of the neutron field and detector efficiency, the reconstruction of the capture-gamma spectrum, and corrections for background, gamma attenuation, neutron scattering, and other experimental effects.

The limited number of retained measurements and the substantial separation between the low-energy Voignier dataset and the single high-energy Budnar value must be considered when interpreting the following comparisons.

2.7.2 Comparison between EXFOR Data and Evaluated Libraries

The experimental cross-section data for the $^{209}Bi(n,\gamma)^{210}Bi$ reaction were retrieved from the EXFOR database [8] and compared with six evaluated nuclear data libraries: ENDF/B-VIII.0, JEFF-3.3, JENDL-5, TENDL-2023, ROSFOND-2010, and CENDL-3.2 [9-14]. Each evaluated curve was interpolated at the corresponding experimental neutron energies using the procedure described in Section 2.4.

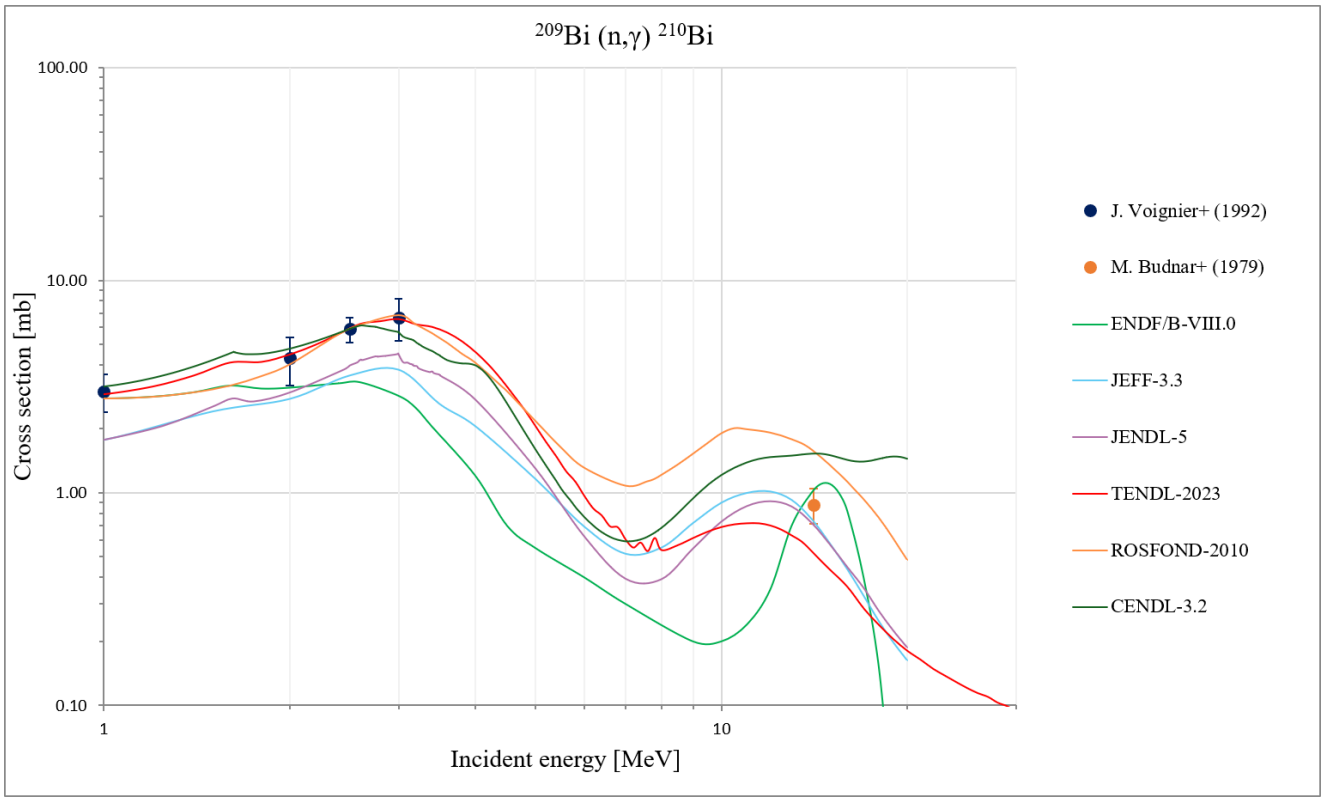

Figure 23 – Comparison between the experimental measurements reported by Voignier et al. [28] and Budnar et al. [29], retrieved from the EXFOR database [8], and evaluated nuclear data libraries [9-14] for the ^{209}Bi(n,γ)^{210}Bi reaction.

Within the investigated 1–30 MeV neutron-energy range, the retained experimental dataset consists of four low-energy measurements reported by Voignier et al. [28] and one measurement at 14.1 MeV reported by Budnar et al. [29]. This limited and non-uniform energy coverage must be considered when interpreting both the graphical comparison and the statistical indicators.

The Voignier measurements show an increase in the capture cross section between 1 and 3 MeV. In this region, TENDL-2023 and ROSFOND-2010 most closely reproduce both the magnitude and the increasing experimental trend. CENDL-3.2 also remains close to several of these measurements, whereas ENDF/B-VIII.0, JEFF-3.3, and JENDL-5 increasingly underestimate the experimental cross section toward 3 MeV.

At higher energy, ENDF/B-VIII.0 provides the closest agreement with the Budnar measurement at 14.1 MeV. JEFF-3.3 and JENDL-5 also remain relatively close to the experimental value, although both underestimate it. TENDL-2023 produces a more pronounced underestimation, whereas ROSFOND-2010 and CENDL-3.2 overestimate the measured cross section.

The relative performance of the evaluated libraries changes across the investigated energy range. TENDL-2023 and ROSFOND-2010 provide the closest descriptions of the four low-energy

measurements, whereas ENDF/B-VIII.0 gives the closest agreement with the single retained high-energy measurement.

To quantify the comparison, the relative difference between each interpolated library value and the corresponding EXFOR measurement was calculated. The complete point-by-point comparison is reported in Appendix A, while the principal statistical indicators are summarized in Table 14.

	Mean relative difference [%]	**Mean absolute relative difference [%]**	**Median absolute relative difference [%]**
ENDF/B-VIII.0	-24.08	30.45	27.44
JEFF-3.3	-34.92	34.92	39.34
JENDL-5	-31.57	31.57	32.91
TENDL-2023	-8.56	10.06	3.26
ROSFOND-2010	13.37	19.11	6.51
CENDL-3.2	15.34	21.09	11.12

Table 14 – Statistical summary of the relative differences between experimental data retrieved from the EXFOR database [8] and evaluated nuclear data libraries [9-14] for the $^{209}Bi(n,\gamma)^{210}Bi$ reaction.

TENDL-2023 provides the lowest mean absolute relative difference, equal to 10.06%, and the lowest median absolute relative difference, equal to 3.26%. ROSFOND-2010 gives the second-lowest mean absolute relative difference, equal to 19.11%, and a median absolute relative difference of 6.51%. These results mainly reflect the close agreement of the two libraries with the four Voignier measurements, which represent most of the retained experimental dataset.

CENDL-3.2 also provides comparatively good global indicators, with a mean absolute relative difference of 21.09%. ENDF/B-VIII.0 has a higher mean absolute relative difference of 30.45%, but gives the closest agreement with the single high-energy measurement reported by Budnar et al. Consequently, the global statistical indicators are dominated by the four low-energy Voignier measurements and do not fully describe the energy-dependent performance of the evaluated libraries.

The negative mean relative differences obtained for ENDF/B-VIII.0, JEFF-3.3, JENDL-5, and TENDL-2023 indicate an average tendency to underestimate the retained experimental

measurements. In contrast, the positive mean relative differences obtained for ROSFOND-2010 and CENDL-3.2 indicate an average tendency to overestimate them.

Overall, TENDL-2023 provides the smallest deviations across the complete selected dataset, followed by ROSFOND-2010 and CENDL-3.2. Nevertheless, no single evaluated library gives the best agreement in both the low- and high-energy regions. These conclusions should be interpreted cautiously because they are based on only five experimental measurements, four of which belong to the same low-energy dataset.

2.7.3 Comparison with TALYS Calculations

The experimental data retrieved from EXFOR [8] were also compared with TALYSworld calculations obtained by varying the Level Density and Photon Strength Function models [17], [18]. As for the previous case studies, the aim of this comparison was to evaluate the model dependence of the calculated capture cross section and to identify the model combinations providing the closest agreement with the retained experimental measurements.

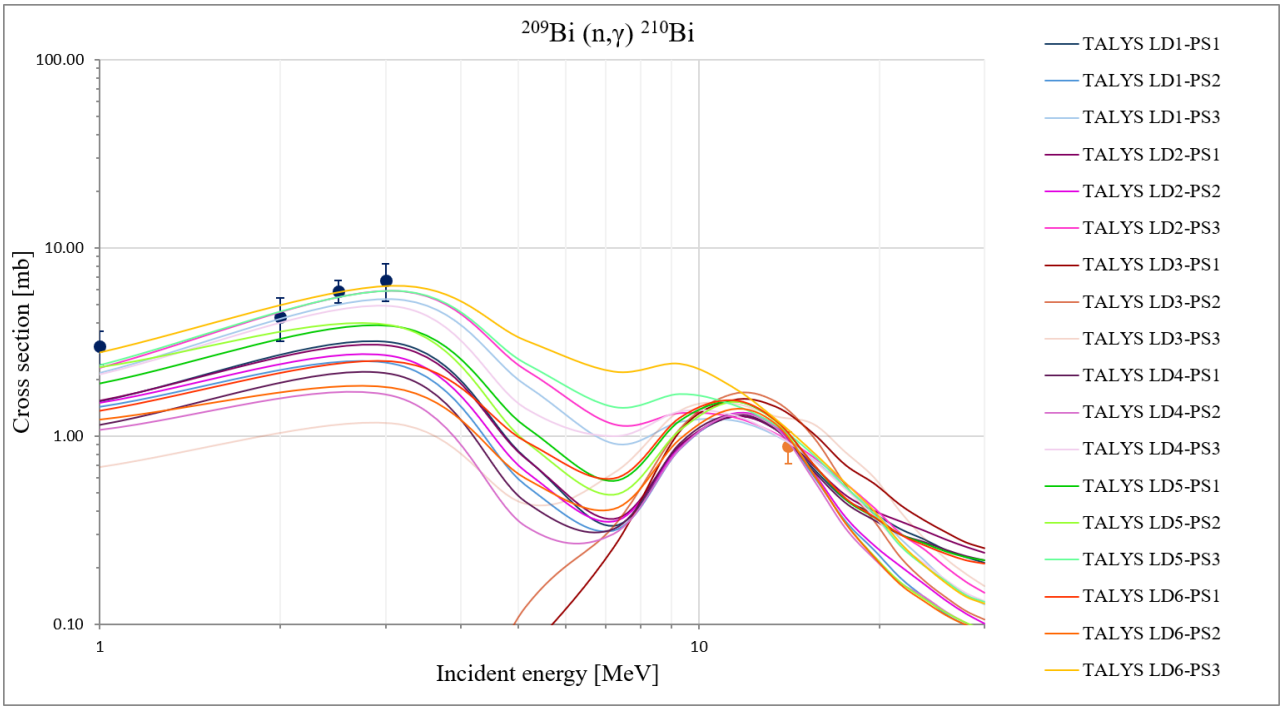

Figure 24 – Comparison between experimental data reported by Voignier et al. [28] and Budnar et al. [29] and TALYSworld calculations for the ^{209}Bi(n,γ)^{210}Bi reaction, obtained by varying the Level Density and Photon Strength Function models [17], [18].

Figure 24 shows that the TALYSworld calculations reproduce the general order of magnitude and the overall energy dependence of the retained EXFOR measurements. However, a non-negligible spread is observed among the different LD–PSF combinations, particularly in the low- and intermediate-energy regions.

Between 1 and 3 MeV, the Voignier measurements show an increasing trend of the capture cross section [28]. Most TALYSworld calculations reproduce this qualitative behaviour, although the predicted magnitude depends significantly on the selected Level Density and Photon Strength Function models.

Among the tested combinations, LD6–PSF3 provides the closest agreement with the Voignier dataset. This calculation follows both the magnitude and the increasing trend of the four experimental measurements in the 1–3 MeV interval. For this reason, LD6–PSF3 was selected for the restricted chi-square analysis presented in Section 2.7.4.

The TALYSworld curves also exhibit a clear model spread, especially in the low- and intermediate-energy regions. An important feature is the behaviour of the LD3–PSF1 and LD3–PSF2 combinations, which predict substantially lower cross-section values than the other calculations around the minimum of the curves. These two simulations therefore strongly influence the lower part of the complete model envelope and are examined separately in the reduced empirical covariance analysis.

At higher energy, the experimental measurement reported by Budnar et al. at 14.1 MeV lies within the range of the TALYSworld predictions [29]. In this region, the different model combinations are more compact than in the low-energy interval, although some model-dependent spread remains visible.

Overall, the direct comparison confirms that the calculated $^{209}Bi(n,\gamma)^{210}Bi$ cross section is sensitive to the selected LD–PSF combination. The dependence is particularly evident below approximately 10 MeV, while the calculations become more closely grouped at higher neutron energies. This model spread is examined quantitatively through the restricted chi-square, empirical covariance, and sensitivity analyses presented in the following sections.

2.7.4 Restricted Chi-square Analysis of the LD6–PSF3 TALYS Calculation

Since no experimental cross-section value was obtained in the present work for the $^{209}Bi(n,\gamma)^{210}Bi$ reaction, the chi-square analysis was performed by comparing a selected TALYSworld calculation with a restricted subset of the EXFOR measurements. As discussed in Section 2.7.3, the LD6–PSF3

combination provides the closest agreement with the four low-energy measurements reported by Voignier et al. [28] and was therefore selected for the quantitative comparison.

The analysis was restricted to the Voignier dataset in order to compare the calculation with measurements obtained within the same experimental campaign and over a continuous low-energy interval. The LD6–PSF3 curve was interpolated at the four experimental neutron energies between 1 and 3 MeV and compared with the corresponding EXFOR values using the chi-square definition introduced in Section 1.6.1.

The resulting total chi-square is:

$$\chi^2 = 0.776$$

for $N = 4$ experimental points, corresponding to:

$$\frac{\chi^2}{N} = 0.194$$

This low value indicates that the differences between the LD6–PSF3 calculation and the selected Voignier measurements are small compared with the reported experimental uncertainties. This agrees with the graphical comparison in Section 2.7.3, where the curve follows both the magnitude and the increasing trend of the measurements between 1 and 3 MeV.

However, this result should be interpreted as a restricted weighted-discrepancy indicator rather than as a formal goodness-of-fit test. No model parameters were fitted to the selected measurements, and the LD6–PSF3 combination was identified on the basis of its agreement with the same experimental dataset. Moreover, the analysis includes only four points from a single experimental campaign and does not include the high-energy measurement reported by Budnar et al. at 14.1 MeV [29].

The result therefore supports the local agreement of the LD6–PSF3 calculation with the Voignier dataset, but it does not constitute a general validation of this model combination over the complete 1–30 MeV neutron-energy range.

2.7.5 Empirical Covariance Analysis of TALYS Model Predictions for ^{209}Bi

The empirical covariance approach introduced in Section 1.6.2 was applied to the ^{209}Bi(n,γ)^{210}Bi reaction using the complete ensemble of eighteen TALYSworld calculations obtained by combining six Level Density models with three Photon Strength Function models [17], [18].

At each neutron energy, the mean cross section, empirical standard deviation, and complete minimum–maximum model envelope were calculated from the eighteen predictions. The resulting model-spread representation was compared with the experimental measurements retrieved from EXFOR [8] and retained in the present analysis.

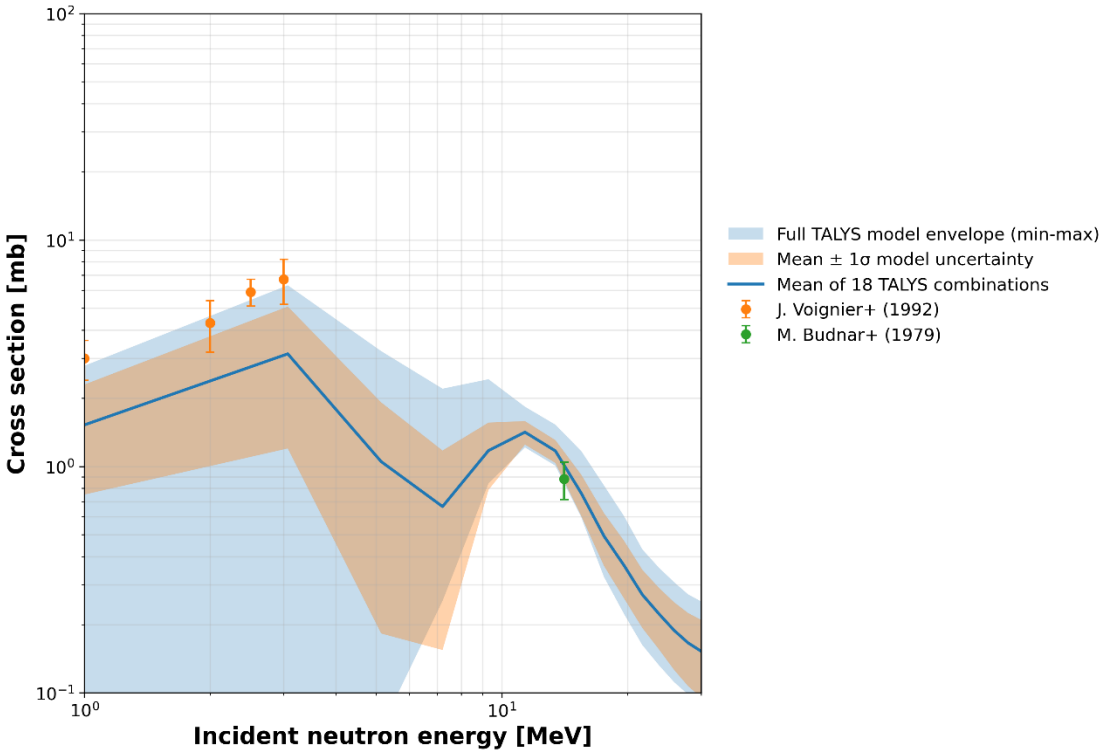

Figure 25 – Empirical model-spread representation for the ^{209}Bi(n,γ)^{210}Bi reaction, obtained from eighteen TALYSworld LD–PSF combinations [17], [18] and compared with the experimental measurements reported by Voignier et al. [28] and Budnar et al. [29].

The TALYSworld calculations reproduce the general order of magnitude and energy dependence of the available experimental data. However, a broad model envelope is observed in the low-energy region, particularly between approximately 1 and 7 MeV.

At 1 MeV, the mean TALYS cross section is approximately 1.52 mb, with an empirical standard deviation of 0.77 mb and a coefficient of variation of 50.7%. The relative model spread is largest around 5–7 MeV, where the coefficient of variation reaches approximately 82.6% at 5.14 MeV and 76.7% at 7.21 MeV. These values indicate a strong dependence of the calculated capture cross section on the selected LD–PSF combination in this energy region.

The four Voignier measurements between 1 and 3 MeV [28] are located within the full TALYS model envelope and generally above the mean prediction. This indicates that several TALYS combinations

underestimate the measured cross sections, although the complete ensemble covers the experimental trend.

The width and asymmetry of the low-energy envelope are strongly influenced by the LD3–PSF1 and LD3–PSF2 calculations. These two combinations predict substantially lower cross sections than the remaining models, particularly near 1–3 MeV. The very low lower boundaries are determined by the two LD3-based calculations and also reduce the ensemble mean.

Above approximately 9–10 MeV, the TALYS predictions become more closely grouped. The experimental value reported by Budnar et al. at 14.1 MeV [29] lies within the lower part of the complete TALYS model envelope, indicating consistency with the range generated by the investigated model combinations.

To isolate the influence of the two low LD3-based predictions, the empirical covariance analysis was repeated after excluding the LD3–PSF1 and LD3–PSF2 combinations.

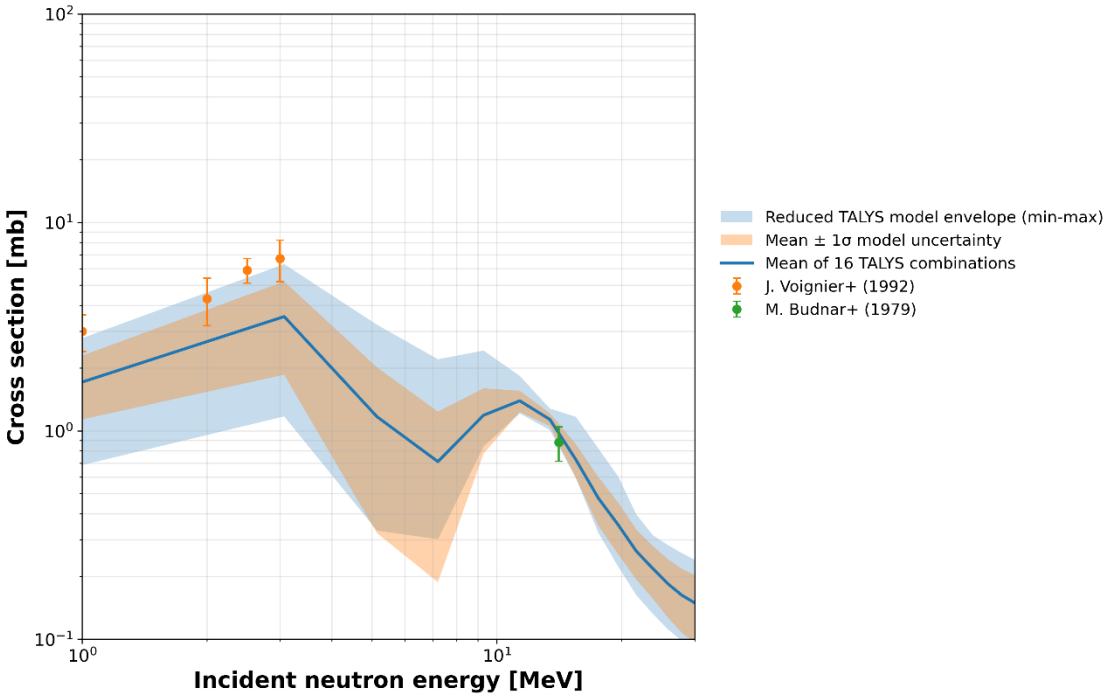

Figure 26 – Reduced empirical model-spread representation for the ^{209}Bi(n,γ)^{210}Bi reaction, recalculated using sixteen TALYSworld combinations after excluding LD3–PSF1 and LD3–PSF2 [17], [18], and compared with the experimental measurements reported by Voignier et al. [28] and Budnar et al. [29].

The exclusion of LD3–PSF1 and LD3–PSF2 produces a substantial reduction of the lower part of the model envelope in the low-energy region. At 1 MeV, the minimum predicted cross section increases from approximately 0.013 to 0.685 mb, while the coefficient of variation decreases from 50.7% to 33.8%. At 3.07 MeV, the lower envelope boundary increases from approximately 0.010 to 1.17 mb, and the coefficient of variation decreases from 61.8% to 47.4%. The mean cross section also increases from 1.52 to 1.71 mb at 1 MeV and from 3.14 to 3.53 mb at 3.07 MeV.

The reduction is less pronounced around 5–7 MeV. At 5.14 MeV, the coefficient of variation decreases from approximately 82.6% to 72.4%, showing that a substantial model dependence remains even after the two lowest calculations are excluded. The residual spread therefore cannot be attributed exclusively to LD3–PSF1 and LD3–PSF2 but also reflects differences among the remaining LD–PSF combinations.

The reduced mean prediction follows the low-energy experimental trend more closely, although the Voignier measurements remain near the upper part of the model envelope. Above approximately 9–10 MeV, the differences between the complete and reduced ensembles become comparatively limited. The Budnar measurement at 14.1 MeV remains within or close to the lower part of the reduced model envelope.

The reduced analysis is intended only as a diagnostic assessment of the influence of LD3–PSF1 and LD3–PSF2. Their exclusion is not based on an independent statistical rejection criterion, and the reduced band should not replace the complete eighteen-model representation. The full ensemble remains the primary description of the spread generated by the investigated TALYSworld options, while the reduced calculation clarifies the origin of the pronounced downward extension observed at low neutron energies.

Overall, the empirical covariance analysis shows that the ^{209}Bi(n,γ)^{210}Bi reaction is strongly dependent on the selected TALYS model combination below approximately 7 MeV. LD3–PSF1 and LD3–PSF2 account for a substantial part of the lower extension of the model envelope, but a non-negligible spread remains after their exclusion. At higher energies, the TALYS predictions become more compact and provide a more consistent description of the available experimental information. Both the complete and reduced bands represent empirical model spread and should not be interpreted as formal confidence intervals or evaluated nuclear-data covariances.

2.7.6 Sensitivity Analysis of TALYS Model Inputs for ^{209}Bi

The same two-factor sum-of-squares decomposition introduced in Section 1.6.3 was applied to the eighteen TALYSworld predictions for the ^{209}Bi(n,γ)^{210}Bi reaction [17-19]. Since the methodology was

already described for the gold case, the present discussion focuses on the energy-dependent contributions of the Level Density model, the Photon Strength Function model, and their LD–PSF interaction.

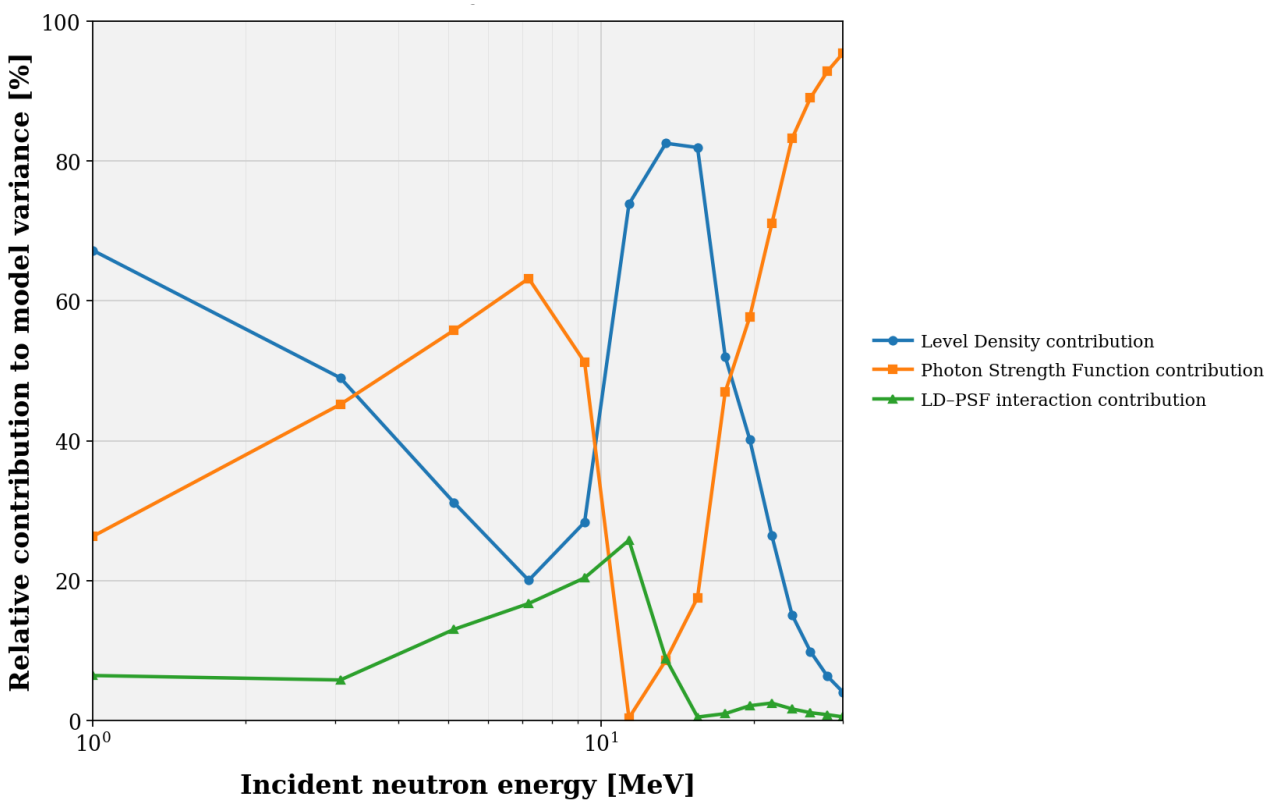

Figure 27 – Relative contributions of the Level Density model, Photon Strength Function model, and LD–PSF interaction to the total spread of the eighteen TALYSworld predictions for the ^{209}Bi(n,γ)^{210}Bi reaction [17-19].

At low energy, the Level Density model provides the largest contribution to the TALYS spread. This behaviour is consistent with the covariance analysis, where the widest part of the model envelope was strongly influenced by specific LD-dependent combinations.

Between approximately 3 and 9 MeV, the relative importance of the Photon Strength Function increases. In particular, the PSF contribution becomes dominant over part of this interval, indicating that the calculated capture cross section is increasingly affected by the description of gamma-ray de-excitation.

In the intermediate-energy region, approximately between 11 and 17 MeV, the Level Density model becomes dominant again. The differences among the TALYS predictions in this interval are therefore mainly associated with the adopted level-density prescription.

At higher neutron energies, above approximately 20 MeV, the Photon Strength Function becomes the principal source of variability, while the Level Density and interaction contributions decrease. The interaction term remains generally secondary, although it is not negligible in some parts of the intermediate-energy range.

For $^{209}Bi(n,\gamma)^{210}Bi$, the dominant source of the TALYSworld model spread changes noticeably with neutron energy. The Level Density model is more influential at low and intermediate energies, whereas the Photon Strength Function becomes increasingly important at higher energies. These results complement the covariance analysis by identifying the model inputs responsible for the observed spread.

2.8 Case Study of ^{232}Th

The last reaction considered is ^{232}Th(n,γ)^{233}Th, which extends the analysis to the actinide region. The experimental measurements retrieved from EXFOR were compared with evaluated nuclear data libraries and with TALYSworld calculations obtained using different Level Density and Photon Strength Function models [8], [17], [18].

Compared with the ^{209}Bi(n,γ)^{210}Bi case, the ^{232}Th(n,γ)^{233}Th reaction is supported by a substantially larger experimental database within the investigated energy range. The available measurements cover both the low-energy region, where the capture cross section decreases rapidly with increasing neutron energy, and the higher-energy region, where the cross section reaches values of a few millibarns or less [8].

Only measurements between 1 and 30 MeV were considered, following the same energy interval used for the other reactions. The EXFOR data published between 1958 and 1963 were excluded because the later measurements available from 1976 onward already provided sufficient experimental coverage [8]. This chronological selection was defined before comparing the data with the evaluated libraries or TALYS calculations.

2.8.1 Comparison between EXFOR Data and Evaluated Libraries

The selected EXFOR measurements for the ^{232}Th(n,γ)^{233}Th reaction [8] were compared with five evaluated nuclear data libraries: ENDF/B-VIII.0, JEFF-3.3, JENDL-5, ROSFOND-2010, and CENDL-3.2 [9-11], [13], [14].

TENDL-2023 was not included in the comparison because the dataset retrieved for this reaction was numerically identical to the ENDF/B-VIII.0 evaluation over the investigated energy range and was therefore not treated as an independent curve [12]. The retrieved ENDF/B-VIII.0 and JEFF-3.3 datasets were also numerically identical. However, both were retained because they are formally distributed as separate evaluated libraries and the comparison was performed independently for each library.

Each evaluated curve was interpolated at the corresponding experimental neutron energies using the procedure described in Section 2.4.

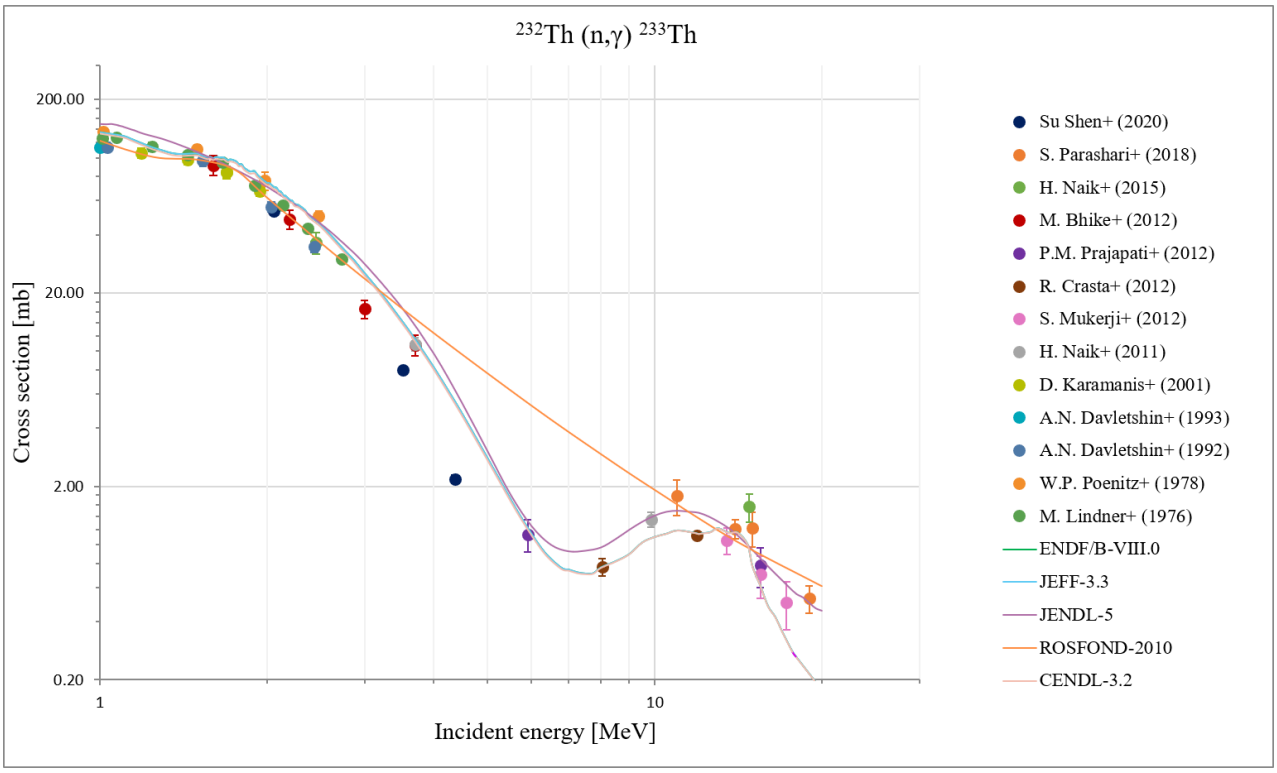

Figure 28 – Comparison between experimental data retrieved from the EXFOR database [8] and evaluated nuclear data libraries [9-11], [13], [14] for the ^{232}Th(n,γ)^{233}Th reaction in the 1–30 MeV neutron-energy range.

Between approximately 1 and 5 MeV, the measured values fall from around 100 mb to only a few millibarns. The evaluated libraries reproduce this general behaviour and remain close to most measurements, particularly below about 2 MeV.

A larger dispersion is observed between approximately 3 and 5 MeV. Some measurements reported in EXFOR, including points attributed to Su Shen et al. and Bhike et al., lie below the main evaluated-library trend [8]. These values produce comparatively large local relative differences and have a noticeable influence on the mean-based statistical indicators.

Between 3 and 14 MeV, ROSFOND-2010 contains fewer tabulated energy points than the other libraries, resulting in a smoother interpolated trend. It does not reproduce the local minimum and the rise observed in the other evaluations and therefore overestimates several measurements in this region.

Above approximately 8–10 MeV, the cross section decreases to values close to or below 1 mb. The experimental data are more dispersed in this region, although the evaluated libraries generally reproduce the order of magnitude of the measurements.

Appendix A contains the complete point-by-point results, while Table 15 reports the main statistical indicators.

	Mean relative difference [%]	Mean absolute relative difference [%]	Median absolute relative difference [%]
ENDF/B-VIII.0	8.95	21.46	14.95
JEFF-3.3	8.95	21.46	14.95
JENDL-5	19.28	23.98	18.41
ROSFOND-2010	32.76	40.59	10.83
CENDL-3.2	6.72	19.91	12.84

Table 15 – Statistical summary of the relative differences between experimental data retrieved from the EXFOR database [8] and evaluated nuclear data libraries [9-11], [13], [14] for the ^{232}Th(n,γ)^{233}Th reaction.

CENDL-3.2 provides the lowest mean absolute relative difference, equal to 19.91%, and the smallest average bias, equal to 6.72%. ENDF/B-VIII.0 and JEFF-3.3 give identical statistical results because the retrieved datasets contain the same numerical values for this reaction. JENDL-5 shows a slightly larger overall deviation. ROSFOND-2010 has the lowest median absolute relative difference, indicating comparatively small deviations for several individual measurements. However, its substantially larger mean absolute relative difference shows that a limited number of larger discrepancies strongly affect its average performance.

All the evaluated libraries reproduce the general energy dependence of the ^{232}Th(n,γ)^{233}Th cross section. For the selected EXFOR dataset, CENDL-3.2 gives the most balanced agreement, although the relative performance of the libraries still varies with neutron energy and with the local dispersion of the experimental measurements.

2.8.2 Comparison with TALYS Calculations

Figure 29 compares the selected EXFOR measurements [8] with eighteen TALYSworld calculations obtained using different Level Density and Photon Strength Function models [17], [18].

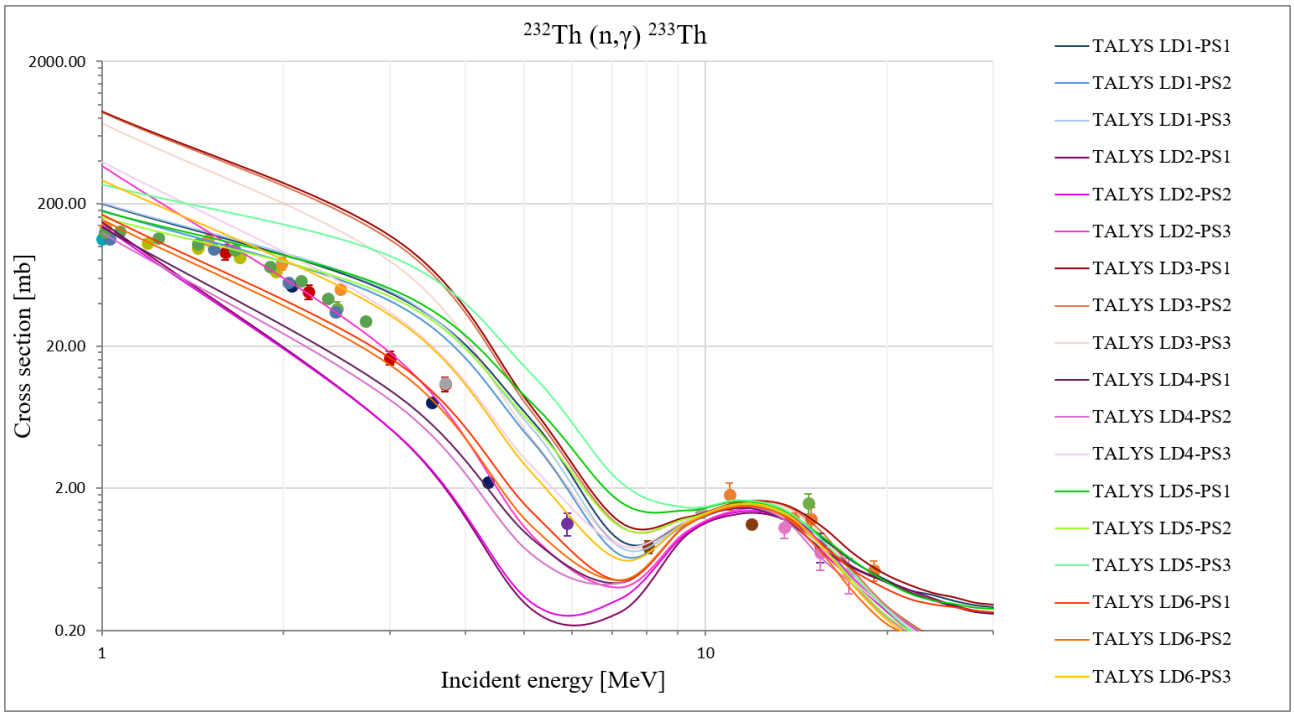

Figure 29 – Comparison between experimental data retrieved from the EXFOR database [8] and TALYSworld calculations for the $^{232}Th(n,\gamma)^{233}Th$ reaction, obtained by varying the Level Density and Photon Strength Function models [17], [18].

The TALYSworld calculations reproduce the overall energy dependence of the $^{232}Th(n,\gamma)^{233}Th$ cross section. A pronounced decrease is observed from the low-energy region to approximately 5–7 MeV, followed by a minimum and a smaller structure at higher neutron energies. The EXFOR measurements follow the same general behaviour, although a noticeable dispersion is present among the different experimental datasets.

Between approximately 1 and 4 MeV, most of the experimental measurements lie within or close to the range of TALYSworld predictions. However, the calculated cross section shows a marked dependence on the selected LD–PSF combination. In particular, the LD3-based calculations predict substantially higher cross-section values than most of the remaining combinations and strongly influence the upper part of the model range in the low-energy region.

Most of the TALYSworld curves outside the LD3 group follow the decreasing experimental trend more closely. The measurements reported by Bhike et al. between approximately 1.6 and 3.7 MeV [31] fall within an interval where the model predictions are still clearly separated. For this reason, the Bhike dataset was selected for the restricted chi-square analysis in Section 2.8.3.

Above approximately 8–10 MeV, the TALYSworld calculations become more closely grouped and generally reproduce the order of magnitude of the available EXFOR measurements. Some differences

remain between individual experimental datasets and model combinations, but the model spread is less pronounced than in the low-energy region.

The calculated ^{232}Th(n,γ)^{233}Th cross section is particularly sensitive to the selected nuclear-model inputs at low and intermediate neutron energies. The influence of the LD3-based calculations on the complete model spread is examined further in the empirical covariance analysis presented in Section 2.8.4.

2.8.3 Restricted Chi-square Analysis of the LD4–PSF1 TALYS Calculation

Since no thorium cross section was measured in the present work, the restricted chi-square comparison was based on the four measurements reported by Bhike et al. between 1.6 and 3.7 MeV [31]. Using a single experimental dataset avoids combining measurements obtained by different authors and under different experimental conditions.

Among the eighteen TALYSworld calculations considered, LD4–PSF1 produced the lowest chi-square value with respect to the Bhike dataset. The calculated curve was interpolated at the corresponding experimental neutron energies and compared with the measured cross sections using the chi-square definition introduced in Section 1.6.1.

The resulting total chi-square is:

$$\chi^2 = 21.81$$

for $N = 4$ experimental points, corresponding to:

$$\frac{\chi^2}{N} = 5.45$$

Although LD4–PSF1 is the closest TALYS curve to the selected Bhike dataset, the value of $\frac{\chi^2}{N}$ remains considerably higher than unity. The differences between the calculation and the measurements are therefore large compared with the reported experimental uncertainties.

The largest contributions to the chi-square arise from the measurements at 2.20 and 3.70 MeV. At 2.20 MeV, the LD4–PSF1 calculation overestimates the experimental cross section, whereas at 3.70 MeV it underestimates it.

LD4–PSF1 gives the best local agreement with the Bhike dataset among the calculations considered, but significant differences remain. This local comparison does not validate the model over the complete 1–30 MeV neutron-energy range.

2.8.4 Empirical Covariance Analysis of TALYS Model Predictions for ^{232}Th

Figure 30 presents the model spread obtained from the eighteen TALYSworld LD–PSF combinations considered for the ^{232}Th(n,γ)^{233}Th reaction [17], [18], together with the experimental measurements retrieved from EXFOR [8].

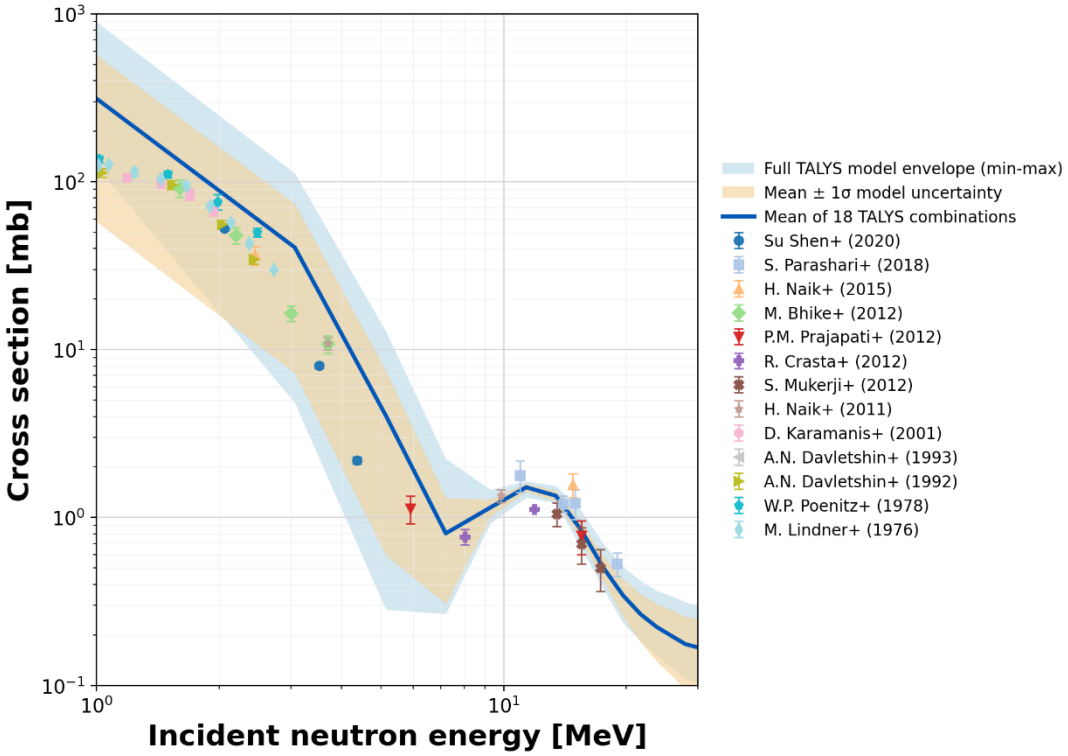

Figure 30 – Empirical model-spread representation for the ^{232}Th(n,γ)^{233}Th reaction, obtained from eighteen TALYSworld LD–PSF combinations [17], [18] and compared with experimental data retrieved from EXFOR [8].

The mean TALYSworld prediction follows the general decrease of the capture cross section, but the model range remains broad below approximately 7 MeV. In this region, the three LD3-based calculations predict considerably higher values than most of the other combinations and largely determine the upper part of the envelope.

The EXFOR measurements generally follow the same decreasing trend. Several points in the low-energy region lie below the TALYSworld mean but remain within or close to the complete model envelope. Above approximately 10 MeV, the calculated curves become more closely grouped and the available experimental measurements generally remain within or near the predicted range.

The band was then recalculated without LD3–PSF1, LD3–PSF2, and LD3–PSF3, leaving fifteen TALYSworld combinations.

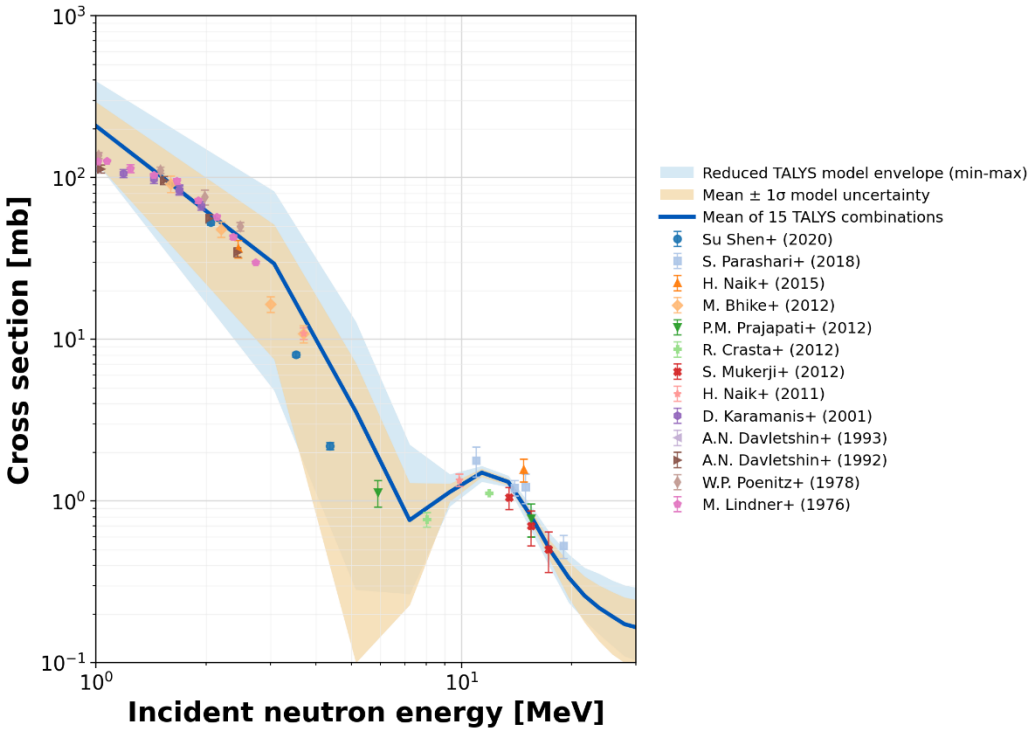

Figure 31 – Reduced empirical model-spread representation for the ^{232}Th(n,γ)^{233}Th reaction, recalculated using fifteen TALYSworld combinations after excluding the three LD3-based calculations [17], [18], and compared with experimental data retrieved from EXFOR [8].

After removing the LD3-based calculations, the model envelope becomes considerably narrower in the low-energy region. The reduced mean curve provides a more representative description of the central group of TALYSworld predictions and follows the experimental trend more closely between approximately 1 and 4 MeV.

A substantial spread nevertheless remains between approximately 3 and 7 MeV. Around 5 MeV, the lower boundary of the mean ±1σ band approaches the lower limit of the logarithmic vertical axis. This feature results from the large relative spread among the remaining model predictions and should not be interpreted as a physical prediction of a vanishing cross section.

Once the LD3-based calculations are removed, the low-energy envelope becomes narrower, but the remaining TALYS curves still show a clear model dependence. The reduced band is therefore used only to isolate the influence of the LD3 group, while the complete ensemble remains the reference representation. Neither band should be interpreted as a formal confidence interval or as an evaluated nuclear-data covariance.

2.8.5 Sensitivity Analysis of TALYS Model Inputs for ^{232}Th

Figure 32 shows the contributions of the Level Density model, the Photon Strength Function model, and their interaction to the spread of the eighteen TALYSworld predictions [17-19].

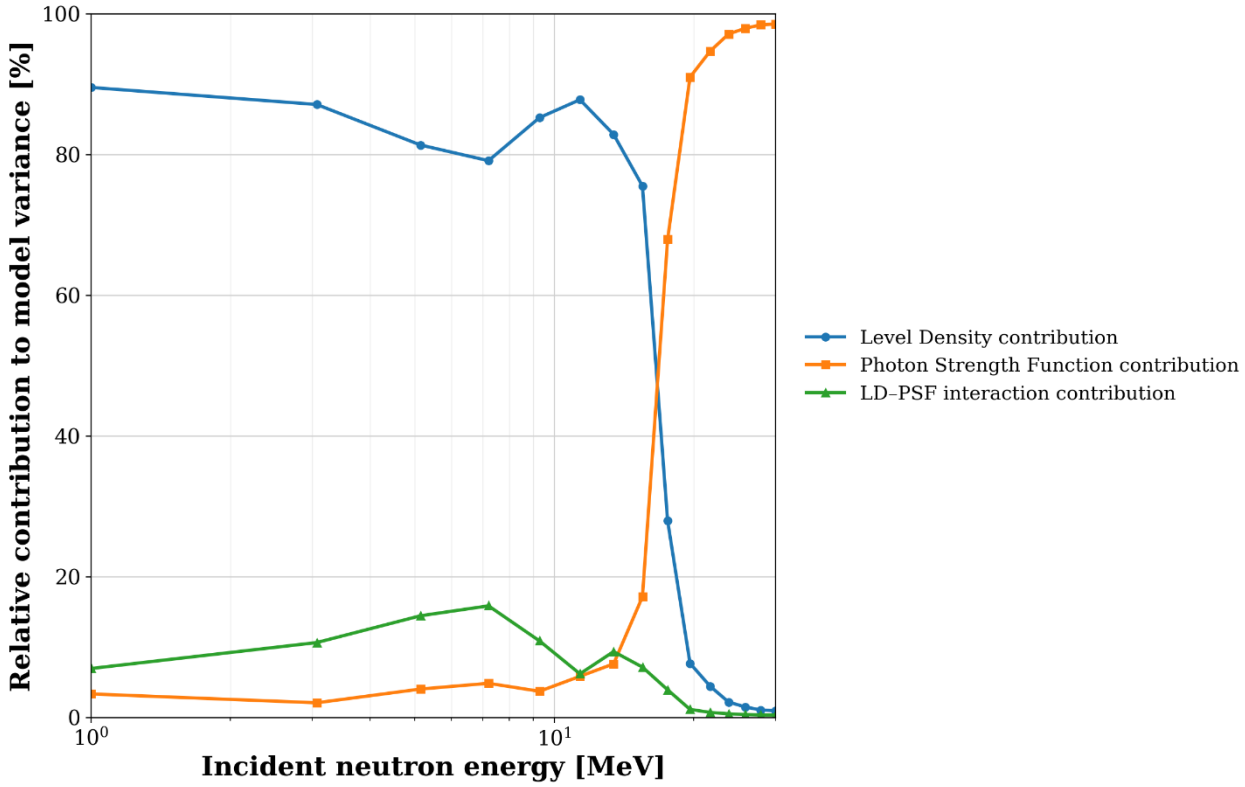

Figure 32 – Relative contributions of the Level Density model, Photon Strength Function model, and LD–PSF interaction to the total spread of the eighteen TALYSworld predictions for the ^{232}Th(n,γ)^{233}Th reaction [17-19].

The Level Density model dominates the calculated spread from approximately 1 to 17 MeV. This is also the region in which the LD3-based calculations produce the largest separation among the TALYSworld predictions.

Within the same energy interval, the Photon Strength Function has a comparatively limited influence. The interaction between LD and PSF remains secondary, although it contributes to the model spread in part of the intermediate-energy region.

A clear change in sensitivity occurs above approximately 17–18 MeV. As the neutron energy increases, the Level Density contribution decreases, while the Photon Strength Function becomes progressively more important. Above approximately 20 MeV, the PSF model represents the main source of variability among the TALYSworld predictions.

Chapter 3 – Summary and Conclusions

3.1 Summary

3.1.1 ^{197}Au Experiment

The first part of this work focused on the experimental activation of natural gold through the ^{197}Au(n,γ)^{198}Au reaction. Gold was used as activation material because natural gold is essentially composed of ^{197}Au and because the produced radionuclide, ^{198}Au, has favourable decay characteristics for delayed gamma-ray spectrometry. In particular, the 411.8 keV gamma emission of ^{198}Au provides a clear reference peak for activity determination.

Two gold foils were irradiated using two Am–Be neutron sources with different activities and were then measured with the NaI(Tl) and $LaBr_3$(Ce) detectors. After checking the detector calibration and estimating the detector efficiencies at the 411.8 keV gamma line, the activity of each foil was calculated from the data extracted from the Gamwin software for the different measurements, including the net peak area, live time, real time, and cooling time.

The resulting activity values were consistent within each detector, but Detector 2 generally gave lower values than Detector 1. This systematic difference was also reflected in the cross-section results and may be related to uncertainties in detector-efficiency calibration, peak fitting, and measurement geometry.

The experimental cross section was calculated using the activation equation, including the estimated neutron flux, the number of ^{197}Au target atoms, and the saturation factor associated with the irradiation time. The values obtained from the different foils and detectors were of the same order of magnitude, mostly between about 6 and 10 mb. By combining the measurements, an effective cross section of 8.12 ± 1.71 mb was obtained at a representative neutron energy of approximately 4.2 MeV. This result should be interpreted as an effective value associated with the Am–Be neutron spectrum, rather than as a strictly monoenergetic cross section. The Am–Be source produces a broad neutron-energy distribution, and the neutron flux was estimated using a simplified geometrical approach and a literature-based neutron yield. For this reason, the result is affected not only by counting and detector-related uncertainties, but also by the assumptions used in the neutron-flux estimation.

The experimental results were compared with available EXFOR measurements and evaluated nuclear data libraries, as well as with the simulations obtained from TALYSworld. In addition, three statistical analyses were performed to support the interpretation of the data: a local chi-square analysis, an empirical covariance analysis, and a sensitivity analysis. These approaches were used to assess the consistency between experimental and theoretical results and to explore the variability associated

with different nuclear-model inputs. The detailed discussion of the outcomes of these comparisons and analyses is presented in the final conclusions.

3.1.2 Four Selected Radiative-Capture Reactions

The second part of this thesis extended the analysis to four additional neutron radiative-capture reactions: $^{51}V(n,\gamma)^{52}V$, $^{103}Rh(n,\gamma)^{104}Rh$, $^{209}Bi(n,\gamma)^{210}Bi$, and $^{232}Th(n,\gamma)^{233}Th$. These reactions were selected to cover different mass regions, from a light nucleus to an actinide target, and were analysed in the neutron-energy range from 1 to 30 MeV. For each reaction, experimental data from EXFOR were compared with evaluated nuclear data libraries and with TALYSworld calculations obtained by varying the Level Density and Photon Strength Function models.

For $^{51}V(n,\gamma)^{52}V$, the experimental database showed a noticeable dispersion, especially around 14–15 MeV. The low value reported by Majumder and Mitra had a strong effect on the percentage-based statistical indicators, since the relative differences are normalized by the experimental cross section. Among the evaluated libraries, TENDL-2023 provided the lowest mean and median absolute relative differences for the selected dataset. The TALYSworld comparison reproduced the general decreasing trend of the cross section, although the agreement depended on the energy region and on the experimental subset considered. The LD6–PSF3 calculation was used for the restricted chi-square comparison with the Zaikin dataset, but the resulting value still indicated deviations larger than the reported experimental uncertainties.

For $^{103}Rh(n,\gamma)^{104}Rh$, the main feature of the experimental database was the strong dispersion around 14–15 MeV. In this region, the high values reported by Csikai and co-workers were clearly separated from the lower experimental points available at similar energies. This strongly affected the comparison with the evaluated libraries, which generally tended to underestimate the selected dataset. Among the libraries considered, CENDL-3.2 gave the lowest mean absolute relative difference, while ENDF/B-VIII.0 and ROSFOND-2010 gave the lowest median absolute relative difference. In the TALYSworld comparison, the LD1–PSF1 calculation was selected for the restricted chi-square analysis against the low-energy Poenitz dataset, where it provided a reasonably close local description of the experimental trend.

For $^{209}Bi(n,\gamma)^{210}Bi$, the retained experimental dataset was more limited than for vanadium and rhodium. It consisted of four low-energy measurements reported by Voignier et al. and one measurement at 14.1 MeV reported by Budnar et al. This limited energy coverage made the statistical interpretation more sensitive to the individual datasets included in the comparison. TENDL-2023 gave the best overall statistical agreement with the retained measurements, mainly because of its close

agreement with the low-energy Voignier points. At higher energy, however, ENDF/B-VIII.0 was closer to the Budnar measurement. Among the TALYSworld calculations, LD6–PSF3 was selected for the restricted chi-square comparison with the Voignier dataset and provided a good local agreement within the reported experimental uncertainties.

For ^{232}Th(n,γ)^{233}Th, the available experimental database was more extensive and covered a wider part of the investigated energy range. The evaluated libraries reproduced the general decrease of the cross section with increasing neutron energy, although local discrepancies were present where the experimental data were more dispersed. CENDL-3.2 provided the most balanced agreement with the selected EXFOR dataset, while ENDF/B-VIII.0 and JEFF-3.3 gave identical statistical results because the retrieved datasets were numerically the same for this reaction. In the TALYSworld comparison, the Bhike dataset was used for the restricted chi-square analysis, and LD4–PSF1 gave the closest local agreement among the tested calculations. However, the resulting chi-square value remained significantly larger than unity, showing that noticeable differences were still present.

3.2 Conclusions

The experimental result obtained for ^{197}Au represents the central point of the first part of this thesis. The effective cross section of 8.12 ± 1.71 mb, associated with a representative neutron energy of approximately 4.2 MeV, is lower than the main evaluated-library trend in the same energy region, but it remains of the same order of magnitude. This result is also particularly relevant when compared with the TALYSworld model spread. At the closest TALYS energy point, 4.21 MeV, the mean prediction of the complete nine-model ensemble is approximately 8.94 mb, very close to the experimental value. The point also lies within the mean ±1σ model-spread band and inside the full minimum–maximum model envelope.

This agreement with the TALYS mean is an important outcome, but it should not be overinterpreted. The result is based on a single effective experimental point obtained with a broad Am–Be neutron spectrum, and therefore it cannot validate a specific nuclear model over the full energy range. Locally, the best agreement is obtained with the LD2-based TALYS calculations, especially LD2–PSF1, as also indicated by the local chi-square analysis. However, the broader covariance analysis shows that the experimental point is not only close to one individual curve, but also consistent with the central region of the complete TALYS model ensemble. This is more meaningful than selecting a single "best" model, because the model spread itself is part of the uncertainty in the theoretical description.

The extension of the work to ^{51}V, ^{103}Rh, ^{209}Bi, and ^{232}Th was not developed as a direct repetition of the gold activation experiment. The decay properties of the corresponding capture products make the

same experimental approach more complicated: some products decay too rapidly, others do not provide a convenient delayed gamma emission, and others would require a more dedicated low-energy gamma-measurement setup. For this reason, the second part of the thesis was developed as an analytical study based on EXFOR data, evaluated libraries, and TALYSworld calculations. This choice allowed the same comparison tools used for gold to be applied to a wider group of reactions, even without performing new irradiations.

The comparison with evaluated libraries showed that there is no single library that performs best for all reactions and all energy regions. The agreement depends strongly on the isotope considered, the neutron-energy interval, and the experimental dataset used as reference. In some cases, the statistical indicators were strongly affected by isolated or dispersed EXFOR measurements. This was especially evident when a small number of points dominated the mean relative differences. Therefore, global statistical indicators are useful, but they must be read together with the graphical comparison and with the experimental context of the data.

The TALYSworld calculations showed an even clearer reaction dependence. The model spread was not uniform across the five reactions, and in several cases it was controlled by a small number of curves separated from the main group of simulations. A common pattern was observed for four isotopes out of five, including gold: the LD3-based calculations were often clearly detached from the other TALYS curves and strongly affected the model envelope. In gold and bismuth, LD3-based curves mainly influenced the lower part of the band; in rhodium and thorium, specific LD3-based combinations controlled the upper part of the spread. Vanadium was the main exception, since its low-energy spread was more strongly associated with PSF3-based calculations.

This behaviour is important because it explains why the empirical covariance bands are often wide and asymmetric at low neutron energies. When a few TALYS model combinations are far from the others, they increase the minimum–maximum envelope and affect the mean and standard deviation of the ensemble. The reduced covariance analyses showed this effect clearly: after excluding the most detached curves, the bands became narrower and the central trend of the remaining simulations became easier to interpret. However, these reduced bands should be seen only as diagnostic tools. The full model ensemble remains necessary to represent the complete range of model behaviours considered in the analysis.

The sensitivity analyses confirmed that the origin of the model spread changes with neutron energy. For gold and vanadium, an inversion between the dominant contributions of the Level Density model and the Photon Strength Function occurs around 8 MeV. For rhodium and thorium, a similar change appears at higher energies, around 18–20 MeV. Bismuth shows a less regular behaviour, with more

than one change in the dominant contribution and no single clear transition over the whole investigated range. This means that the role of LD and PSF cannot be generalized without considering both the reaction and the energy interval.

These transitions are also connected to the shape of the TALYS bands. In the first part of the energy range, the calculated curves are usually more separated and the model envelope is wider. In this region, the Level Density model often has a strong influence, especially when one LD family is clearly detached from the others. At higher neutron energies, the TALYS curves tend to move closer together and the minimum–maximum envelope becomes narrower. In this region, the Photon Strength Function can become more relevant, and in some cases it becomes the dominant source of variability. The sensitivity analysis therefore gives a physical interpretation of the covariance bands: it does not only show that the models differ, but also indicates which nuclear-model input is mainly responsible for the difference.

Overall, the results of this thesis show that neutron-capture cross-section analysis cannot rely on a single source of information. The experimental ^{197}Au result provides a direct reference point and is consistent with the central TALYS model-spread region at the representative Am–Be energy. The analytical study of ^{51}V, ^{103}Rh, ^{209}Bi, and ^{232}Th shows that evaluated libraries, EXFOR data, and TALYS calculations may agree well in some regions but differ significantly in others. These differences are caused by both experimental-data dispersion and nuclear-model dependence.

The empirical covariance and sensitivity analyses were therefore useful as interpretative tools. They should not be considered formal uncertainty evaluations, but they help identify the size of the model spread, the model combinations responsible for it, and the energy regions where the theoretical predictions are less stable. From this point of view, the main conclusion is that neutron-capture predictions strongly depend on the isotope and the energy region, and that experimental measurements, evaluated libraries, and nuclear-model calculations should be used together rather than treated as interchangeable sources.

Future improvements should focus first on a better characterization of the neutron field and of the source-to-sample geometry. This would reduce the uncertainties associated with the neutron-flux estimation and would make the experimental result easier to compare with evaluated data and TALYS calculations. For the other reactions, dedicated experimental setups would be required, depending on the half-life and gamma-emission characteristics of each activation product. Even within these limitations, the combined approach adopted in this work provides a useful framework for connecting activation measurements with nuclear-data evaluation and model-uncertainty analysis.

Finally, measurements, evaluated nuclear-data libraries, and model calculations should be regarded as complementary, not interchangeable, sources of information.

Bibliography

[1] International Atomic Energy Agency (IAEA), “Neutron activation analysis,” Vienna, Austria. [Online]. Available: https://www.iaea.org/topics/neutron-activation-analysis.

[2] National Nuclear Data Center (NNDC), “NuDat 3.0,” Brookhaven National Laboratory, Upton, NY, USA. [Online]. Available: https://www.nndc.bnl.gov/nudat3/

[3] H. Ito, K. Wada, T. Yano, Y. Hino, Y. Ommura, M. Harada, A. Minamino, and M. Ishitsuka, “Analyzing the neutron and γ-ray emission properties of an americium–beryllium tagged neutron source,” Nuclear Instruments and Methods in Physics Research Section A: Accelerators, Spectrometers, Detectors and Associated Equipment, vol. 1057, Art. no. 168701, Dec. 2023, doi: 10.1016/j.nima.2023.168701.

[4] K. Amgarou and M. Herranz, “State-of-the-art and challenges of non-destructive techniques for in-situ radiological characterization of nuclear facilities to be dismantled,” Nuclear Engineering and Technology, vol. 53, no. 11, pp. 3491–3504, Nov. 2021, doi: 10.1016/j.net.2021.05.031.

[5] International Atomic Energy Agency, Software for Nuclear Spectrometry, IAEA-TECDOC-1049, Vienna, Austria, 1998.

[6] M. R. Winberg and R. S. Garcia, National Low-Level Waste Management Program Radionuclide Report Series, Volume 14: Americium-241, Report DOE/LLW-130, Idaho National Engineering Laboratory, Lockheed Idaho Technologies Company, Idaho Falls, ID, USA, Sep. 1995.

[7] U.S. Nuclear Regulatory Commission, “Neutron Activation and Activation Analysis,” H-122 Basic Health Physics, Module 28, Washington, DC, USA, Nov. 26, 2009. [Online]. Available: https://www.nrc.gov/docs/ML1122/ML11229A714.pdf.

[8] International Atomic Energy Agency (IAEA), “EXFOR: Experimental Nuclear Reaction Data,” Nuclear Data Section, Vienna, Austria. [Online]. Available: https://www-nds.iaea.org/exfor.

[9] D. A. Brown, M. B. Chadwick, R. Capote, et al., “ENDF/B-VIII.0: The 8th major release of the nuclear reaction data library with CIELO-project cross sections, new standards and thermal scattering data,” Nuclear Data Sheets, vol. 148, pp. 1–142, 2018, doi: 10.1016/j.nds.2018.02.001.

[10] A. J. M. Plompen, O. Cabellos, C. De Saint Jean, et al., “The joint evaluated fission and fusion nuclear data library, JEFF-3.3,” European Physical Journal A, vol. 56, Art. no. 181, 2020, doi: 10.1140/epja/s10050-020-00141-9.

[11] O. Iwamoto, N. Iwamoto, S. Kunieda, F. Minato, S. Nakayama, Y. Abe, et al., “Japanese evaluated nuclear data library version 5: JENDL-5,” Journal of Nuclear Science and Technology, vol. 60, no. 1, pp. 1–60, 2023, doi: 10.1080/00223131.2022.2141903.

[12] TENDL Project, “TENDL-2023: TALYS-based Evaluated Nuclear Data Library,” 2023. [Online]. Available: https://tendl.imperial.ac.uk/tendl_2023/tendl2023.html.

[13] OECD Nuclear Energy Agency, “RUSFOND-2010,” Evaluated Nuclear Data Library Descriptions, OECD-NEA Data Bank, Paris, France. [Online]. Available: https://www.oecd-nea.org/jcms/pl_20505/evaluated-nuclear-data-library-descriptions.

[14] Z. Ge, R. Xu, H. Wu, et al., “CENDL-3.2: The new version of Chinese general purpose evaluated nuclear data library,” EPJ Web of Conferences, vol. 239, Art. no. 09001, 2020, doi: 10.1051/epjconf/202023909001.

[15] U.S. Nuclear Regulatory Commission, “Neutron Sources,” Basic Health Physics, H-122, Washington, DC, USA, 2010.

[16] Cross Sections Evaluation Working Group, ENDF-6 Formats Manual: Data Formats and Procedures for the Evaluated Nuclear Data Files ENDF/B-VI, ENDF/B-VII and ENDF/B-VIII, D. A. Brown, Ed., CSEWG Document ENDF-102, Report BNL-224854-2023-INRE. Upton, NY, USA: National Nuclear Data Center, Brookhaven National Laboratory, Sep. 2023. [Online]. Available: https://www.nndc.bnl.gov/endfdocs/ENDF-102-2023.pdf

[17] International Atomic Energy Agency (IAEA), “TALYSworld,” Nuclear Data Section, Vienna, Austria. [Online]. Available: https://nds.iaea.org/relnsd/talys/talys.html.

[18] A. J. Koning, S. Hilaire, and S. Goriely, TALYS-2.2: Simulation of Nuclear Reactions, 2025. [Online]. Available: https://nds.iaea.org/talys/tutorials/talys.pdf.

[19] National Institute of Standards and Technology (NIST), “Models and calculations for the two-way ANOVA,” NIST/SEMATECH e-Handbook of Statistical Methods, Gaithersburg, MD, USA. [Online]. Available: https://www.itl.nist.gov/div898/handbook/prc/section4/prc438.htm.

[20] J. R. de Laeter, J. K. Böhlke, P. De Bièvre, et al., “Atomic weights of the elements: Review 2000,” Pure and Applied Chemistry, vol. 75, no. 6, pp. 683–800, 2003, doi: 10.1351/pac200375060683.

[21] H. Lemmel, “Nuclear data for science & technology: Centres for development,” IAEA Bulletin, vol. 38, no. 2, pp. 34–38, Jun. 1996. [Online]. Available: https://www.iaea.org/sites/default/files/2025-09/vol382_0.pdf.

[22] A. J. Koning, J. Blomgren, R. Jacqmin, et al., Nuclear Data for Sustainable Nuclear Energy: Final Report of a Coordinated Action on Nuclear Data for Industrial Development in Europe (CANDIDE), EUR 23977 EN, JRC 53801. Luxembourg: Office for Official Publications of the European Communities, 2009, doi: 10.2787/14636.

[23] M. Majumder and B. Mitra, “Capture cross section of 14-MeV neutrons,” Transactions of the Bose Research Institute, vol. 40, no. 3, p. 81, 1977.

[24] G. G. Zaikin, I. A. Korzh, N. T. Sklyar, and I. A. Totskii, “Cross sections for the radiative capture of fast neutrons by Ti-50 and V-51,” Soviet Atomic Energy, vol. 23, pp. 742–744, Jul. 1967, doi: 10.1007/BF01565732.

[25] J. Csikai, J. Bacsó, and A. Daróczy, “Investigation of the cross-section of neutron reactions in the nucleus Rh-103,” Nuclear Physics, vol. 41, pp. 316–322, 1963, doi: 10.1016/0029-5582(63)90509-1.

[26] J. Csikai, G. Petö, M. Buczkó, Z. Miligy, and N. A. Eissa, “Radiative capture cross sections for 14.7 MeV neutrons,” Nuclear Physics A, vol. 95, no. 1, pp. 229–234, 1967, doi: 10.1016/0375-9474(67)90164-9.

[27] W. P. Poenitz, “Fast neutron capture cross section measurements, evaluations and model calculations of fission product nuclei,” in Proceedings of the NEANDC Specialists’ Meeting on Neutron Cross Sections of Fission Product Nuclei, Bologna, Italy, Dec. 12–14, 1979, NEANDC(E)-209L, p. 85, 1980.

[28] J. Voignier, S. Joly, and G. Grenier, “Capture cross sections and gamma-ray spectra from the interaction of 0.5- to 3.0-MeV neutrons with nuclei in the mass range A = 45 to 238,” Nuclear Science and Engineering, vol. 112, no. 1, pp. 87–94, 1992, doi: 10.13182/NSE91-92N.

[29] M. Budnar, F. Cvelbar, E. Hodgson, et al., “Prompt gamma-ray spectra and integrated cross sections for the radiative capture of 14 MeV neutrons for 28 natural targets in the mass region from 12 to 208,” Report INDC(YUG)-6, International Atomic Energy Agency, Vienna, Austria, 1979.

[30] M. R. Abdelnour, J. Liu, K. Hossny, A. M. Wajid, W. Li, and Z. Liu, “Prompt gamma neutron activation analysis: A review of applications, design, analytics, challenges, and prospects,” Radiation Physics and Chemistry, vol. 234, Art. no. 112693, Sep. 2025, doi: 10.1016/j.radphyschem.2025.112693.

[31] M. Bhike, B. J. Roy, A. Saxena, R. K. Choudhury, and S. Ganesan, “Measurement of ^{232}Th(n,γ)^{233}Th, ^{98}Mo(n,γ)^{99}Mo, ^{186}W(n,γ)^{187}W, ^{115}In(n,γ)^{116m1}In, and ^{92}Mo(n,p)^{92m}Nb cross sections in the energy range of 1.6 to 3.7 MeV,” Nuclear Science and Engineering, vol. 170, pp. 44–53, 2012, doi: 10.13182/NSE10-63.

Appendix

Appendix A - Point-by-point comparison between EXFOR data and evaluated libraries

Au-197 experimental (n,γ) EXFOR			ENDF/B-VIII.0		JEFF-3.3		JENDL-5		TENDL-2023		ROSFOND-2010		CENDL-3.2	
Target	Energy [eV]	σ exp [b]	σ interp [b]	Rel. difference [%]	σ interp [b]	Rel. difference [%]	σ interp [b]	Rel. difference [%]	σ interp [b]	Rel. difference [%]	σ interp [b]	Rel. difference [%]	σ interp [b]	Rel. difference [%]
Au-197	1.12E+06	0.060	0.0782	29.38	0.0776	28.31	0.0783	29.51	0.0782	29.41	0.0776	28.31	0.0766	26.78
Au-197	2.12E+06	0.041	0.0474	16.71	0.0476	17.36	0.0507	24.80	0.0474	16.76	0.0476	17.36	0.0473	16.64
Au-197	3.12E+06	0.020	0.0227	14.87	0.0228	15.46	0.0185	-6.20	0.0228	15.13	0.0228	15.46	0.0228	15.46
Au-197	4.12E+06	0.014	0.0115	-17.66	0.0115	-17.50	0.0116	-16.54	0.0115	-17.87	0.0115	-17.50	0.0115	-17.50
Au-197	1.00E+06	0.081	0.0794	-1.35	0.0798	-0.87	0.0804	-0.12	0.0794	-1.35	0.0798	-0.87	0.0803	-0.25
Au-197	1.00E+06	0.079	0.0794	0.52	0.0798	1.01	0.0804	1.78	0.0794	0.53	0.0798	1.01	0.0803	1.65
Au-197	2.00E+06	0.052	0.0530	2.00	0.0530	1.88	0.0550	5.77	0.0530	2.00	0.0530	1.88	0.0534	2.69
Au-197	2.50E+06	0.040	0.0341	-14.04	0.0342	-13.75	0.0361	-8.98	0.0341	-14.05	0.0342	-13.75	0.0334	-15.87
Au-197	3.00E+06	0.027	0.0248	-7.45	0.0248	-7.45	0.0196	-26.90	0.0248	-7.45	0.0248	-7.45	0.0248	-7.45
Au-197	1.03E+06	0.080	0.0793	-1.42	0.0793	-1.36	0.0802	-0.30	0.0793	-1.41	0.0793	-1.36	0.0794	-1.28
Au-197	1.53E+06	0.071	0.0691	-2.53	0.0691	-2.58	0.0695	-1.99	0.0686	-3.21	0.0691	-2.58	0.0675	-4.84
Au-197	2.04E+06	0.048	0.0513	6.33	0.0514	6.59	0.0536	11.27	0.0513	6.47	0.0514	6.59	0.0516	7.02
Au-197	2.44E+06	0.036	0.0357	0.17	0.0357	0.32	0.0385	8.15	0.0357	0.17	0.0357	0.32	0.0351	-1.43
Au-197	1.04E+06	0.081	0.0792	-2.19	0.0792	-2.23	0.0801	-1.11	0.0792	-2.19	0.0792	-2.23	0.0792	-2.28
Au-197	1.04E+06	0.080	0.0792	-1.00	0.0791	-1.11	0.0801	0.08	0.0792	-1.00	0.0791	-1.11	0.0790	-1.25
Au-197	1.13E+06	0.083	0.0777	-6.34	0.0772	-7.04	0.0781	-5.96	0.0778	-6.30	0.0772	-7.04	0.0763	-8.13
Au-197	1.14E+06	0.081	0.0777	-4.11	0.0771	-4.82	0.0780	-3.69	0.0777	-4.07	0.0771	-4.82	0.0762	-5.93
Au-197	1.14E+06	0.080	0.0774	-3.22	0.0769	-3.89	0.0779	-2.68	0.0775	-3.17	0.0769	-3.89	0.0760	-5.00
Au-197	1.18E+06	0.074	0.0761	2.80	0.0757	2.31	0.0771	4.16	0.0761	2.86	0.0757	2.31	0.0749	1.19
Au-197	1.19E+06	0.072	0.0757	5.16	0.0754	4.69	0.0769	6.76	0.0757	5.19	0.0754	4.69	0.0746	3.56
Au-197	1.39E+06	0.068	0.0713	4.79	0.0712	4.72	0.0725	6.65	0.0713	4.85	0.0712	4.72	0.0697	2.44
Au-197	2.70E+06	0.033	0.0287	-12.97	0.0289	-12.37	0.0294	-10.81	0.0287	-13.00	0.0289	-12.37	0.0299	-9.35
Au-197	2.03E+06	0.053	0.0515	-2.74	0.0516	-2.56	0.0539	1.61	0.0516	-2.63	0.0516	-2.56	0.0519	-2.10
Au-197	2.26E+06	0.046	0.0416	-9.57	0.0418	-9.12	0.0461	0.15	0.0416	-9.58	0.0418	-9.12	0.0411	-10.63
Au-197	2.54E+06	0.037	0.0333	-10.07	0.0333	-9.90	0.0346	-6.38	0.0333	-10.07	0.0333	-9.90	0.0327	-11.61
Au-197	2.68E+06	0.025	0.0293	17.32	0.0295	18.12	0.0300	20.09	0.0294	17.47	0.0295	18.12	0.0303	21.05
Au-197	2.93E+06	0.022	0.0252	16.00	0.0252	16.00	0.0216	-0.50	0.0252	15.95	0.0252	16.00	0.0260	19.77
Au-197	3.17E+06	0.018	0.0219	23.04	0.0220	23.63	0.0181	1.90	0.0219	23.10	0.0220	23.63	0.0220	23.63
Au-197	3.42E+06	0.016	0.0182	11.45	0.0183	12.02	0.0163	0.06	0.0182	11.46	0.0183	12.02	0.0183	12.02
Au-197	3.69E+06	0.015	0.0150	1.05	0.0150	1.39	0.0144	-2.82	0.0150	1.30	0.0150	1.39	0.0150	1.39
Au-197	3.93E+06	0.013	0.0126	-4.20	0.0127	-3.84	0.0129	-2.53	0.0127	-3.88	0.0127	-3.84	0.0127	-3.84
Au-197	4.13E+06	0.012	0.0114	-3.08	0.0115	-2.90	0.0116	-1.94	0.0114	-3.37	0.0115	-2.90	0.0115	-2.90
Au-197	4.18E+06	0.012	0.0112	-3.30	0.0112	-3.19	0.0113	-3.02	0.0112	-3.85	0.0112	-3.19	0.0112	-3.19
Au-197	4.59E+06	0.009	0.0091	3.75	0.0092	3.98	0.0091	2.99	0.0092	4.00	0.0092	3.98	0.0092	3.98
Au-197	4.87E+06	0.009	0.0079	-7.64	0.0079	-7.35	0.0080	-6.39	0.0079	-7.09	0.0079	-7.35	0.0079	-7.35
Au-197	5.26E+06	0.007	0.0067	-2.84	0.0067	-2.38	0.0069	-0.20	0.0067	-2.38	0.0067	-2.38	0.0067	-2.38
Au-197	5.58E+06	0.006	0.0059	-4.34	0.0060	-3.79	0.0061	-1.02	0.0060	-3.84	0.0060	-3.79	0.0060	-3.79
Au-197	5.90E+06	0.005	0.0050	-2.37	0.0050	-1.65	0.0053	3.51	0.0050	-1.92	0.0050	-1.65	0.0050	-1.65
Au-197	6.25E+06	0.005	0.0041	-12.79	0.0041	-11.77	0.0045	-4.81	0.0041	-11.95	0.0041	-11.77	0.0041	-11.77
Au-197	6.49E+06	0.004	0.0036	-16.40	0.0036	-16.33	0.0040	-6.88	0.0036	-16.34	0.0036	-16.33	0.0036	-16.33
Au-197	6.85E+06	0.002	0.0027	12.89	0.0028	15.12	0.0035	43.90	0.0028	15.12	0.0028	15.13	0.0028	15.13
Au-197	7.13E+06	0.002	0.0019	-16.95	0.0020	-11.01	0.0031	33.75	0.0020	-11.01	0.0020	-11.01	0.0020	-11.01
Au-197	7.26E+06	0.001	0.0015	16.52	0.0017	29.12	0.0029	123.88	0.0017	29.12	0.0017	29.13	0.0017	29.13
Au-197	7.60E+06	0.001	0.0010	19.85	0.0010	20.32	0.0025	218.54	0.0010	20.32	0.0010	20.35	0.0010	20.35
Au-197	2.12E+06	0.054	0.0476	-11.77	0.0478	-11.29	0.0508	-5.77	0.0476	-11.76	0.0478	-11.29	0.0475	-11.80
Au-197	2.27E+06	0.045	0.0414	-8.49	0.0416	-8.02	0.0458	1.28	0.0414	-8.50	0.0416	-8.02	0.0409	-9.53
Au-197	2.34E+06	0.041	0.0385	-6.00	0.0387	-5.51	0.0423	3.24	0.0386	-5.90	0.0387	-5.51	0.0382	-6.94
Au-197	2.44E+06	0.037	0.0355	-4.33	0.0356	-4.16	0.0382	3.06	0.0355	-4.32	0.0356	-4.16	0.0349	-5.91
Au-197	2.87E+06	0.026	0.0255	-2.74	0.0255	-2.73	0.0235	-10.40	0.0255	-2.78	0.0255	-2.73	0.0270	3.02
Au-197	3.24E+06	0.021	0.0209	-0.54	0.0209	-0.46	0.0176	-16.12	0.0209	-0.70	0.0209	-0.46	0.0209	-0.46
Au-197	3.59E+06	0.021	0.0161	-22.26	0.0162	-21.93	0.0151	-26.92	0.0162	-21.96	0.0162	-21.93	0.0162	-21.93
Au-197	1.19E+06	0.077	0.0758	-2.09	0.0754	-2.54	0.0769	-0.64	0.0758	-2.06	0.0754	-2.54	0.0746	-3.59
Au-197	1.49E+06	0.067	0.0697	4.09	0.0697	4.03	0.0702	4.78	0.0697	4.02	0.0697	4.03	0.0681	1.63
Au-197	2.00E+06	0.052	0.0530	2.00	0.0530	1.88	0.0550	5.77	0.0530	2.00	0.0530	1.88	0.0534	2.69
Au-197	3.00E+06	0.020	0.0248	24.02	0.0248	24.02	0.0196	-2.04	0.0248	24.01	0.0248	24.02	0.0248	24.02
Au-197	1.01E+06	0.077	0.0794	3.07	0.0796	3.42	0.0803	4.31	0.0794	3.07	0.0796	3.42	0.0800	3.88
Au-197	1.07E+06	0.085	0.0791	-6.99	0.0787	-7.47	0.0794	-6.60	0.0791	-6.99	0.0787	-7.47	0.0781	-8.08
Au-197	1.24E+06	0.073	0.0742	1.61	0.0739	1.26	0.0759	3.94	0.0744	1.96	0.0739	1.26	0.0732	0.26
Au-197	1.44E+06	0.072	0.0705	-2.13	0.0704	-2.17	0.0714	-0.90	0.0705	-2.12	0.0704	-2.17	0.0688	-4.42
Au-197	1.52E+06	0.071	0.0693	-2.40	0.0693	-2.45	0.0697	-1.85	0.0690	-2.84	0.0693	-2.45	0.0677	-4.70
Au-197	1.66E+06	0.066	0.0656	-0.59	0.0657	-0.42	0.0675	2.24	0.0651	-1.39	0.0657	-0.42	0.0644	-2.38
Au-197	1.90E+06	0.057	0.0564	-0.99	0.0566	-0.72	0.0589	3.41	0.0564	-1.00	0.0566	-0.72	0.0565	-0.88
Au-197	2.14E+06	0.050	0.0465	-6.92	0.0467	-6.51	0.0500	-0.03	0.0465	-6.95	0.0467	-6.51	0.0463	-7.34
Au-197	2.37E+06	0.039	0.0375	-3.76	0.0376	-3.48	0.0411	5.36	0.0376	-3.71	0.0376	-3.48	0.0371	-4.88
Au-197	2.73E+06	0.028	0.0278	-0.65	0.0280	0.00	0.0286	2.07	0.0279	-0.52	0.0280	0.00	0.0294	4.97
Au-197	1.00E+06	0.083	0.0794	-4.32	0.0798	-3.86	0.0804	-3.13	0.0794	-4.32	0.0798	-3.86	0.0803	-3.25
Au-197	1.20E+06	0.074	0.0755	2.11	0.0751	1.67	0.0767	3.81	0.0755	2.11	0.0751	1.67	0.0743	0.59
Au-197	1.30E+06	0.074	0.0729	-1.59	0.0728	-1.82	0.0743	0.27	0.0729	-1.63	0.0728	-1.82	0.0717	-3.19
Au-197	1.40E+06	0.071	0.0711	0.08	0.0710	0.03	0.0723	1.85	0.0711	0.14	0.0710	0.03	0.0694	-2.25
Au-197	1.50E+06	0.073	0.0696	-4.01	0.0696	-4.06	0.0700	-3.47	0.0695	-4.08	0.0696	-4.06	0.0680	-6.28
Au-197	1.70E+06	0.064	0.0640	0.08	0.0641	0.38	0.0668	4.54	0.0640	0.10	0.0641	0.38	0.0631	-1.33
Au-197	1.80E+06	0.065	0.0602	-6.76	0.0602	-6.81	0.0629	-2.66	0.0600	-7.14	0.0602	-6.81	0.0596	-7.74
Au-197	2.00E+06	0.055	0.0530	-3.74	0.0530	-3.85	0.0550	-0.18	0.0530	-3.74	0.0530	-3.85	0.0534	-3.09
Au-197	2.10E+06	0.049	0.0483	-2.26	0.0485	-1.77	0.0513	3.92	0.0483	-2.32	0.0485	-1.77	0.0484	-2.13
Au-197	2.50E+06	0.039	0.0341	-11.36	0.0342	-11.06	0.0361	-6.14	0.0341	-11.37	0.0342	-11.06	0.0334	-13.25
Au-197	3.00E+06	0.032	0.0248	-22.00	0.0248	-22.00	0.0196	-38.39	0.0248	-22.00	0.0248	-22.00	0.0248	-22.00
Au-197	3.50E+06	0.021	0.0171	-16.51	0.0171	-16.51	0.0158	-22.97	0.0171	-16.51	0.0171	-16.51	0.0171	-16.51
Au-197	1.01E+06	0.118	0.0794	-32.70	0.0796	-32.48	0.0803	-31.89	0.0794	-32.69	0.0796	-32.48	0.0799	-32.21
Au-197	1.19E+06	0.111	0.0757	-31.69	0.0753	-32.00	0.0768	-30.64	0.0757	-31.68	0.0753	-32.00	0.0745	-32.73
Au-197	1.30E+06	0.108	0.0730	-32.46	0.0728	-32.62	0.0744	-31.14	0.0730	-32.45	0.0728	-32.62	0.0719	-33.53
Au-197	1.41E+06	0.106	0.0710	-32.73	0.0709	-32.76	0.0722	-31.59	0.0710	-32.70	0.0709	-32.76	0.0693	-34.30
Au-197	1.51E+06	0.104	0.0695	-33.34	0.0694	-33.38	0.0698	-32.97	0.0693	-33.50	0.0694	-33.38	0.0678	-34.91
Au-197	1.70E+06	0.090	0.0641	-28.52	0.0643	-28.30	0.0669	-25.43	0.0641	-28.55	0.0643	-28.30	0.0632	-29.54
Au-197	2.00E+06	0.073	0.0531	-27.65	0.0530	-27.74	0.0551	-24.98	0.0531	-27.65	0.0530	-27.74	0.0535	-27.17
Au-197	2.49E+06	0.045	0.0343	-23.81	0.0344	-23.55	0.0364	-19.16	0.0343	-23.80	0.0344	-23.55	0.0336	-25.37
Au-197	3.01E+06	0.038	0.0247	-34.64	0.0247	-34.61	0.0195	-48.29	0.0247	-34.62	0.0247	-34.61	0.0247	-34.61

Table A.1 – Point-by-point comparison for $^{197}Au(n,\gamma)^{198}Au$

V-51 experimental (n,γ) EXFOR			ENDF/B-VIII.0		JEFF-3.3		JENDL-5		TENDL-2023		ROSFOND-2010	
Target	Energy [eV]	σ exp [b]	σ interp [b]	Relative difference [%]	σ interp [b]	Relative difference [%]	σ interp [b]	Relative difference [%]	σ interp [b]	Relative difference [%]	σ interp [b]	Relative difference [%]
V-51	1.07E+06	0.0028	0.0020	-28.90	0.0022	-21.17	0.0021	-24.23	0.0020	-29.69	0.0021	-25.37
V-51	1.48E+06	0.0022	0.0019	-13.45	0.0018	-17.66	0.0022	-1.62	0.0016	-28.48	0.0020	-8.44
V-51	1.89E+06	0.0018	0.0016	-9.61	0.0015	-16.36	0.0018	0.85	0.0013	-28.70	0.0015	-14.99
V-51	2.30E+06	0.0016	0.0015	-8.64	0.0013	-16.83	0.0017	5.17	0.0011	-29.83	0.0013	-19.57
V-51	2.85E+06	0.0009	0.0014	55.11	0.0013	37.67	0.0017	89.83	0.0010	14.15	0.0012	34.73
V-51	1.05E+06	0.0020	0.0020	3.05	0.0022	13.69	0.0021	9.86	0.0020	1.67	0.0021	7.90
V-51	1.13E+06	0.0017	0.0020	14.77	0.0022	28.51	0.0021	22.76	0.0020	13.89	0.0021	20.93
V-51	1.20E+06	0.0018	0.0020	10.22	0.0022	24.53	0.0021	19.21	0.0019	9.43	0.0021	16.24
V-51	1.29E+06	0.0022	0.0019	-12.51	0.0020	-7.66	0.0021	-3.69	0.0018	-19.12	0.0020	-7.72
V-51	1.39E+06	0.0017	0.0019	14.54	0.0019	11.64	0.0022	28.06	0.0016	-2.54	0.0020	21.20
V-51	1.49E+06	0.0020	0.0019	-4.42	0.0018	-9.16	0.0022	8.79	0.0016	-21.13	0.0020	1.12
V-51	1.66E+06	0.0027	0.0018	-30.91	0.0017	-35.05	0.0022	-16.75	0.0015	-44.14	0.0018	-31.56
V-51	1.02E+06	0.0016	0.0020	29.91	0.0022	42.29	0.0022	38.58	0.0020	27.71	0.0021	35.51
V-51	1.22E+06	0.0014	0.0019	40.03	0.0022	56.01	0.0021	52.09	0.0019	36.96	0.0021	47.51
V-51	1.43E+06	0.0014	0.0019	42.41	0.0018	36.47	0.0022	60.31	0.0016	18.90	0.0020	50.72
V-51	1.63E+06	0.0013	0.0019	41.70	0.0018	32.57	0.0023	71.64	0.0015	14.23	0.0019	39.77
V-51	1.83E+06	0.0011	0.0017	54.73	0.0015	41.88	0.0019	76.36	0.0013	20.92	0.0016	47.53
V-51	2.03E+06	0.0010	0.0015	55.22	0.0014	40.97	0.0017	72.48	0.0012	20.15	0.0013	36.82
V-51	2.22E+06	0.0011	0.0015	41.49	0.0013	28.22	0.0017	61.70	0.0011	8.69	0.0013	25.16
V-51	2.61E+06	0.0011	0.0015	32.83	0.0013	22.41	0.0017	57.77	0.0011	2.25	0.0013	14.51
V-51	1.00E+06	0.0012	0.0020	66.80	0.0022	82.06	0.0022	78.03	0.0020	63.71	0.0021	73.69
V-51	1.10E+06	0.0012	0.0020	67.97	0.0022	87.51	0.0021	78.98	0.0020	66.66	0.0021	76.93
V-51	1.26E+06	0.0013	0.0019	48.03	0.0021	60.11	0.0021	62.00	0.0018	40.39	0.0020	55.77
V-51	1.01E+06	0.0016	0.0020	26.86	0.0022	38.77	0.0022	35.35	0.0020	24.64	0.0021	32.24
V-51	1.21E+06	0.0014	0.0019	41.17	0.0022	58.42	0.0021	53.05	0.0019	39.12	0.0021	48.80
V-51	1.43E+06	0.0014	0.0019	34.43	0.0018	28.74	0.0022	51.47	0.0016	12.14	0.0020	42.27
V-51	1.80E+06	0.0012	0.0017	43.05	0.0015	30.61	0.0019	60.59	0.0013	11.29	0.0016	37.27
V-51	2.20E+06	0.0010	0.0015	47.23	0.0013	33.27	0.0017	68.03	0.0011	13.11	0.0013	30.40
V-51	2.60E+06	0.0010	0.0015	50.72	0.0014	39.28	0.0017	78.71	0.0011	16.39	0.0013	30.00
V-51	2.70E+06	0.0020	0.0015	-26.24	0.0013	-33.72	0.0018	-10.97	0.0011	-44.82	0.0012	-36.70
V-51	4.00E+06	0.0018	0.0009	-51.29	0.0009	-47.83	0.0012	-34.49	0.0009	-51.62	0.0012	-33.48
V-51	1.41E+07	0.0006	0.0007	13.18	0.0006	2.82	0.0008	32.98	0.0006	8.26	0.0010	67.76
V-51	1.48E+07	0.0001	0.0006	815.14	0.0006	752.75	0.0008	1031.47	0.0007	874.18	0.0010	1298.86
V-51	1.46E+07	0.0007	0.0006	-10.53	0.0006	-17.27	0.0008	9.17	0.0007	-8.01	0.0010	35.61
V-51	1.47E+07	0.0006	0.0006	7.07	0.0006	-0.62	0.0008	31.50	0.0007	12.02	0.0010	62.97
V-51	1.46E+07	0.0005	0.0006	31.47	0.0006	21.56	0.0008	60.41	0.0007	35.16	0.0010	99.27
V-51	1.44E+07	0.0014	0.0006	-53.77	0.0006	-57.57	0.0008	-44.40	0.0006	-53.93	0.0010	-30.54
V-51	2.90E+06	0.0014	0.0014	0.36	0.0012	-11.07	0.0018	27.55	0.0010	-26.27	0.0012	-12.93
V-51	1.47E+07	0.0004	0.0006	73.62	0.0006	61.16	0.0008	113.25	0.0007	81.65	0.0010	164.27

Table A.2 – Point-by-point comparison for $^{51}V(n,\gamma)^{52}V$

Note: The highlighted row indicates the low EXFOR value reported by Manjushree Majumder (1977) around 14.8 MeV. Because the relative differences are normalized by this particularly small experimental value, the point strongly affects the mean-based percentage indicators.[23]

Rh-103 experimental (n,γ) EXFOR			ENDF/B-VIII.0		JEFF-3.3		JENDL-5		TENDL-2023		ROSFOND-2010		CENDL-3.2	
Target	Energy [eV]	σ exp [b]	σ interp [b]	Relative difference [%]	σ interp [b]	Relative difference [%]	σ interp [b]	Relative difference [%]	σ interp [b]	Relative difference [%]	σ interp [b]	Relative difference [%]	σ interp [b]	Relative difference [%]
Rh-103	1.00E+06	**0.0730**	**0.0672**	-7.89	**0.0715**	-2.04	**0.0624**	-14.55	**0.0321**	-56.05	**0.0672**	-7.90	**0.0790**	8.21
Rh-103	1.30E+06	**0.0690**	**0.0611**	-11.42	**0.0564**	-18.31	**0.0559**	-18.96	**0.0292**	-57.71	**0.0611**	-11.42	**0.0687**	-0.47
Rh-103	1.50E+06	**0.0610**	**0.0553**	-9.41	**0.0505**	-17.23	**0.0497**	-18.55	**0.0279**	-54.25	**0.0553**	-9.41	**0.0622**	1.90
Rh-103	2.00E+06	**0.0450**	**0.0412**	-8.39	**0.0411**	-8.59	**0.0389**	-13.47	**0.0294**	-34.67	**0.0412**	-8.39	**0.0480**	6.67
Rh-103	2.50E+06	**0.0350**	**0.0303**	-13.30	**0.0346**	-1.22	**0.0330**	-5.63	**0.0323**	-7.68	**0.0303**	-13.30	**0.0365**	4.33
Rh-103	3.00E+06	**0.0270**	**0.0208**	-23.04	**0.0307**	13.62	**0.0274**	1.30	**0.0340**	25.84	**0.0208**	-23.03	**0.0277**	2.61
Rh-103	3.50E+06	**0.0170**	**0.0151**	-11.21	**0.0269**	58.34	**0.0224**	31.77	**0.0333**	95.83	**0.0159**	-6.61	**0.0216**	26.88
Rh-103	4.00E+06	**0.0140**	**0.0110**	-21.62	**0.0239**	70.85	**0.0181**	29.56	**0.0306**	118.68	**0.0110**	-21.62	**0.0181**	29.63
Rh-103	2.00E+06	**0.0480**	**0.0412**	-14.11	**0.0411**	-14.31	**0.0389**	-18.88	**0.0294**	-38.75	**0.0412**	-14.11	**0.0480**	0.00
Rh-103	3.00E+06	**0.0170**	**0.0208**	22.24	**0.0307**	80.45	**0.0274**	60.89	**0.0340**	99.86	**0.0208**	22.24	**0.0277**	62.98
Rh-103	1.46E+07	**0.0020**	**0.0008**	-61.47	**0.0020**	-1.90	**0.0009**	-53.18	**0.0011**	-45.66	**0.0008**	-61.49	**0.0009**	-53.60
Rh-103	1.11E+06	**0.0730**	**0.0648**	-11.27	**0.0652**	-10.65	**0.0597**	-18.20	**0.0310**	-57.60	**0.0648**	-11.27	**0.0752**	3.01
Rh-103	1.41E+07	**0.0008**	**0.0008**	11.22	**0.0022**	190.35	**0.0010**	29.12	**0.0012**	65.63	**0.0008**	11.19	**0.0009**	21.39
Rh-103	1.34E+07	**0.0166**	**0.0009**	-94.52	**0.0023**	-86.02	**0.0010**	-93.99	**0.0015**	-90.99	**0.0009**	-94.52	**0.0009**	-94.67
Rh-103	1.36E+07	**0.0160**	**0.0009**	-94.46	**0.0023**	-85.79	**0.0010**	-93.81	**0.0014**	-91.15	**0.0009**	-94.46	**0.0009**	-94.42
Rh-103	1.39E+07	**0.0150**	**0.0009**	-94.32	**0.0022**	-85.19	**0.0010**	-93.49	**0.0013**	-91.34	**0.0009**	-94.32	**0.0009**	-93.97
Rh-103	1.41E+07	**0.0146**	**0.0008**	-94.32	**0.0022**	-85.20	**0.0010**	-93.38	**0.0012**	-91.57	**0.0008**	-94.32	**0.0009**	-93.75
Rh-103	1.43E+07	**0.0138**	**0.0008**	-94.16	**0.0021**	-84.97	**0.0010**	-93.08	**0.0012**	-91.50	**0.0008**	-94.16	**0.0009**	-93.34
Rh-103	1.45E+07	**0.0133**	**0.0008**	-94.12	**0.0020**	-85.05	**0.0009**	-92.91	**0.0011**	-91.61	**0.0008**	-94.12	**0.0009**	-93.05
Rh-103	1.50E+07	**0.0129**	**0.0007**	-94.39	**0.0019**	-85.62	**0.0009**	-92.94	**0.0010**	-92.49	**0.0007**	-94.40	**0.0009**	-92.72
Rh-103	1.47E+07	**0.0140**	**0.0008**	-94.58	**0.0019**	-86.18	**0.0009**	-93.36	**0.0011**	-92.45	**0.0008**	-94.58	**0.0009**	-93.35
Rh-103	1.00E+06	**0.0810**	**0.0672**	-16.99	**0.0715**	-11.71	**0.0624**	-22.99	**0.0321**	-60.39	**0.0672**	-16.99	**0.0790**	-2.48

Table A.3 – Point-by-point comparison for the $^{103}\mathrm{Rh}(\mathrm{n},\gamma)^{104}\mathrm{Rh}$

Bi-209 experimental (n,γ) EXFOR			ENDF/B-VIII.0		JEFF-3.3		JENDL-5		TENDL-2023		ROSFOND-2010		CENDL-3.2	
Target	Energy [eV]	σ exp [b]	σ interp [b]	Relative difference [%]	σ interp [b]	Relative difference [%]	σ interp [b]	Relative difference [%]	σ interp [b]	Relative difference [%]	σ interp [b]	Relative difference [%]	σ interp [b]	Relative difference [%]
Bi-209	1.00E+06	**0.003**	**0.00278**	-7.333333333	**0.00178**	-40.66666667	**0.001773**	-40.90006667	**0.00290222**	-3.2593	**0.00278**	-7.333333333	**0.00317**	5.666666667
Bi-209	2.00E+06	**0.0043**	**0.00312**	-27.44186047	**0.002778**	-35.39534884	**0.00295582**	-31.26006977	**0.00446177**	3.762139535	**0.00402**	-6.511627907	**0.004778**	11.11627907
Bi-209	2.50E+06	**0.0059**	**0.00329**	-44.23728814	**0.003579**	-39.33898305	**0.00394753**	-33.09268218	**0.00589272**	-0.123313559	**0.00587**	-0.508474576	**0.005926**	0.440677966
Bi-209	3.00E+06	**0.0067**	**0.00286**	-57.31343284	**0.003814**	-43.07462687	**0.00449515**	-32.90826866	**0.00655542**	-2.157865672	**0.00686**	2.388059701	**0.005737**	-14.37313433
Bi-209	1.41E+07	**0.0009**	**0.00102**	15.90909091	**0.0007382**	-16.11363636	**0.00070688**	-19.67218507	**0.00051916**	-41.00485	**0.00157345**	78.80113636	**0.0015298**	73.84090909

Table A.4 – Point-by-point comparison for the $^{209}\mathrm{Bi}(\mathrm{n},\gamma)^{210}\mathrm{Bi}$

Th-232 experimental (n,γ) EXFOR			ENDF/B-VIII.0		JEFF-3.3		JENDL-5		ROSFOND-2010		CENDL-3.2	
Target	Energy [eV]	σ exp [b]	σ interp [b]	Relative difference [%]	σ interp [b]	Relative difference [%]	σ interp [b]	Relative difference [%]	σ interp [b]	Relative difference [%]	σ interp [b]	Relative difference [%]
Th-232	2.06E+06	0.0528	0.0705	33.64	0.0705	33.64	0.0671	27.18	0.0591	12.08	0.0685	29.91
Th-232	3.52E+06	0.0080	0.0142	76.52	0.0142	76.52	0.0164	104.51	0.0178	121.81	0.0138	71.73
Th-232	4.36E+06	0.0022	0.0056	154.25	0.0056	154.25	0.0063	187.11	0.0111	406.54	0.0054	147.38
Th-232	1.10E+07	0.0018	0.0012	-33.70	0.0012	-33.70	0.0015	-16.22	0.0017	-4.94	0.0012	-33.86
Th-232	1.40E+07	0.0012	0.0012	-4.47	0.0012	-4.47	0.0011	-5.91	0.0010	-13.50	0.0011	-4.77
Th-232	1.50E+07	0.0012	0.0008	-36.72	0.0008	-36.72	0.0009	-23.03	0.0010	-20.36	0.0008	-36.97
Th-232	1.90E+07	0.0005	0.0002	-59.43	0.0002	-59.43	0.0005	-5.62	0.0007	28.99	0.0002	-59.55
Th-232	2.45E+06	0.0364	0.0473	30.00	0.0473	30.00	0.0476	30.84	0.0389	6.89	0.0460	26.46
Th-232	1.48E+07	0.0016	0.0009	-40.97	0.0009	-40.97	0.0010	-37.80	0.0010	-37.15	0.0009	-41.17
Th-232	1.60E+06	0.0915	0.0993	8.56	0.0993	8.56	0.0986	7.75	0.0933	1.93	0.0970	6.06
Th-232	2.20E+06	0.0480	0.0605	26.10	0.0605	26.10	0.0594	23.66	0.0519	8.07	0.0589	22.62
Th-232	3.00E+06	0.0165	0.0253	53.32	0.0253	53.32	0.0282	71.15	0.0237	43.59	0.0246	49.17
Th-232	3.70E+06	0.0108	0.0116	6.97	0.0116	6.97	0.0134	23.76	0.0158	46.07	0.0112	4.06
Th-232	5.90E+06	0.0011	0.0012	9.82	0.0012	9.82	0.0013	18.43	0.0056	393.81	0.0012	7.45
Th-232	1.55E+07	0.0008	0.0006	-21.40	0.0006	-21.40	0.0008	8.87	0.0009	19.94	0.0006	-21.67
Th-232	8.04E+06	0.0008	0.0008	-0.38	0.0008	-0.38	0.0010	26.60	0.0029	278.52	0.0008	-0.96
Th-232	1.19E+07	0.0011	0.0011	2.05	0.0011	2.05	0.0015	30.75	0.0015	34.14	0.0011	1.83
Th-232	1.35E+07	0.0011	0.0012	10.41	0.0012	10.41	0.0012	17.16	0.0012	9.61	0.0012	10.06
Th-232	1.55E+07	0.0007	0.0006	-12.54	0.0006	-12.54	0.0008	21.14	0.0009	33.45	0.0006	-12.84
Th-232	1.73E+07	0.0005	0.0003	-36.15	0.0003	-36.15	0.0006	22.97	0.0008	60.10	0.0003	-36.47
Th-232	3.70E+06	0.0109	0.0116	5.99	0.0116	5.99	0.0134	22.63	0.0158	44.73	0.0112	3.11
Th-232	9.85E+06	0.0014	0.0011	-20.32	0.0011	-20.32	0.0014	2.44	0.0020	47.66	0.0011	-20.44
Th-232	1.19E+06	0.1060	0.1189	12.17	0.1189	12.17	0.1340	26.45	0.1060	-0.02	0.1164	9.84
Th-232	1.44E+06	0.0980	0.1049	7.04	0.1049	7.04	0.1120	14.33	0.0984	0.41	0.1025	4.62
Th-232	1.69E+06	0.0840	0.0983	17.04	0.0983	17.04	0.0916	9.10	0.0893	6.34	0.0959	14.21
Th-232	1.69E+06	0.0840	0.0983	17.04	0.0983	17.04	0.0916	9.10	0.0893	6.34	0.0959	14.21
Th-232	1.94E+06	0.0670	0.0798	19.12	0.0798	19.12	0.0745	11.19	0.0681	1.66	0.0776	15.87
Th-232	1.00E+06	0.1130	0.1355	19.93	0.1355	19.93	0.1494	32.19	0.1224	8.35	0.1332	17.92
Th-232	1.03E+06	0.1134	0.1338	17.97	0.1338	17.97	0.1490	31.36	0.1198	5.68	0.1315	15.92
Th-232	1.53E+06	0.0962	0.1027	6.72	0.1027	6.72	0.1043	8.43	0.0963	0.14	0.1003	4.28
Th-232	2.04E+06	0.0558	0.0722	29.45	0.0722	29.45	0.0683	22.46	0.0602	7.84	0.0702	25.84
Th-232	2.44E+06	0.0346	0.0477	37.98	0.0477	37.98	0.0480	38.86	0.0394	13.94	0.0464	34.23
Th-232	1.01E+06	0.1370	0.1349	-1.50	0.1349	-1.50	0.1492	8.91	0.1216	-11.26	0.1326	-3.18
Th-232	1.50E+06	0.1110	0.1050	-5.41	0.1050	-5.41	0.1070	-3.65	0.0976	-12.03	0.1026	-7.56
Th-232	1.98E+06	0.0760	0.0759	-0.11	0.0759	-0.11	0.0721	-5.17	0.0642	-15.52	0.0738	-2.88
Th-232	2.48E+06	0.0500	0.0460	-7.94	0.0460	-7.94	0.0464	-7.25	0.0373	-25.30	0.0448	-10.44
Th-232	1.01E+06	0.1260	0.1349	7.09	0.1349	7.09	0.1492	18.41	0.1216	-3.52	0.1326	5.28
Th-232	1.07E+06	0.1270	0.1315	3.51	0.1315	3.51	0.1478	16.40	0.1164	-8.37	0.1291	1.62
Th-232	1.24E+06	0.1140	0.1135	-0.43	0.1135	-0.43	0.1295	13.60	0.1016	-10.83	0.1110	-2.61
Th-232	1.44E+06	0.1040	0.1049	0.87	0.1049	0.87	0.1120	7.74	0.0984	-5.39	0.1025	-1.42
Th-232	1.66E+06	0.0950	0.1001	5.40	0.1001	5.40	0.0939	-1.20	0.0906	-4.59	0.0977	2.89
Th-232	1.90E+06	0.0720	0.0853	18.45	0.0853	18.45	0.0771	7.04	0.0720	0.04	0.0830	15.27
Th-232	2.14E+06	0.0570	0.0641	12.53	0.0641	12.53	0.0625	9.65	0.0550	-3.53	0.0624	9.41
Th-232	2.37E+06	0.0430	0.0514	19.44	0.0514	19.44	0.0512	19.04	0.0431	0.13	0.0500	16.18
Th-232	2.73E+06	0.0300	0.0345	14.95	0.0345	14.95	0.0367	22.20	0.0305	1.69	0.0336	11.84

Table A.5 – Point-by-point comparison for the $^{232}Th(n,\gamma)^{233}Th$

Appendix B – TALYS Level Density and Photon Strength Function Models

This appendix briefly summarizes the TALYS Level Density and Photon Strength Function model options varied in this work. The aim is not to reproduce the complete TALYS theoretical implementation, but to document the main nuclear model inputs used in the TALYS calculations.

In the notation adopted throughout this thesis, LD1–LD6 correspond to the TALYS options "ldmodel 1–ldmodel 6", whereas PSF1–PSF3 correspond to "strength 1–strength 3".

In TALYS, the nuclear level density $\rho(E_x, J, \Pi)$represents the number of nuclear levels per MeV at excitation energy E_x, spin J, and parity Π. The total level density is obtained by summing over spin and parity:

$$\rho^{tot}(E_x) = \sum_J \sum_{\Pi} \rho(E_x, J, \Pi)$$

For analytical level-density models, TALYS generally factorizes the spin- and parity-dependent level density as:

$$\rho(E_x, J, \Pi) = P(E_x, J, \Pi) R(E_x, J) \rho^{tot}(E_x)$$

where $P(E_x, J, \Pi)$is the parity distribution and $R(E_x, J)$is the spin distribution. In most TALYS level-density models, parity equipartition is assumed:

$$P(E_x, J, \Pi) = \frac{1}{2}$$

A common expression used in the analytical models is the Fermi Gas level density:

$$\rho_F^{tot}(E_x) = \frac{1}{\sqrt{2\pi}\sigma} \frac{\sqrt{\pi}}{12} \frac{\exp\left(2\sqrt{aU}\right)}{a^{1/4} U^{5/4}}$$

with:

$$U = E_x - \Delta$$

where $a$is the level-density parameter, $\sigma$is the spin cut-off parameter, and $\Delta$is an energy shift related to pairing effects.

The Level Density options used in this work are summarized in Table B.1 according to the model definitions reported in the TALYS manual [18].

TALYS option	Model	Main formulation
ldmodel 1	Constant Temperature + Fermi Gas Model	Uses a constant-temperature expression at low excitation energy and the Fermi Gas expression at higher energy.
ldmodel 2	Back-shifted Fermi Gas Model	Uses the Fermi Gas formulation with a shifted excitation energy (U=E_x-\Delta_{BFM}).
ldmodel 3	Generalized Superfluid Model	Includes pairing correlations and describes the transition from superfluid behaviour at low energy to Fermi Gas behaviour at high energy.
ldmodel 4	Microscopic level-density tables	Based on microscopic tabulated level densities.
ldmodel 5	Microscopic combinatorial level-density tables	Based on microscopic combinatorial calculations.
ldmodel 6	Temperature-dependent Gogny-HFB combinatorial tables	Based on temperature-dependent Hartree-Fock-Bogoliubov calculations using the Gogny force.

Table B.1 – TALYS Level Density models used in this work, summarized from the TALYS manual [18].

For **ldmodel 1**, the Constant Temperature Model uses:

$$\rho_T^{tot}(E_x) = \frac{1}{T}\exp\left(\frac{E_x - E_0}{T}\right)$$

at low excitation energy, while the Fermi Gas expression is used above the matching energy. For **ldmodel 2**, the Back-shifted Fermi Gas Model uses the Fermi Gas expression with:

$$U = E_x - \Delta_{BFM}$$

For **ldmodel 3**, the Generalized Superfluid Model introduces pairing effects. In its low-energy region, the total level density is expressed as:

$$\rho_{GSM}^{tot}(E_x) = \frac{1}{\sqrt{2\pi}\sigma}\frac{e^S}{\sqrt{D}}$$

where $S$is the entropy and $D$is the determinant associated with the saddle-point approximation. At higher excitation energy, the model returns to a Fermi Gas type expression. The models **ldmodel 4**, **ldmodel 5**, and **ldmodel 6** are instead based on microscopic tabulated level densities; therefore, no single compact analytical expression is reported here.

The Photon Strength Function describes the average probability of gamma-ray emission or absorption. In TALYS, the photon transmission coefficient is related to the Photon Strength Function by:

$$T_{X\ell}(E_\gamma) = 2\pi f_{X\ell}(E_\gamma)E_\gamma^{2\ell+1}$$

where E_γ is the gamma-ray energy, Xdenotes electric or magnetic radiation, and $\ell$is the multipolarity.

The Photon Strength Function options used in this work are summarized in Table B.2 according to the model definitions reported in the TALYS manual [18].

TALYS option	Model	Main formulation
strength 1	Kopecky-Uhl generalized Lorentzian	Generalized Lorentzian with energy- and temperature-dependent width.
strength 2	Brink-Axel standard Lorentzian	Standard Lorentzian description of the giant dipole resonance.
strength 3	Skyrme-Hartree-Fock BCS + QRPA tables	Microscopic tabulated photon strength functions.

Table B.2 – TALYS Photon Strength Function models used in this work, summarized from the TALYS manual [18].

For **strength 1**, the Kopecky-Uhl generalized Lorentzian for E1 radiation is expressed as:

$$f_{E1}(E_\gamma, T) = K_{E1}\left[\frac{E_\gamma \tilde{\Gamma}_{E1}(E_\gamma)}{\left(E_\gamma^2 - E_{E1}^2\right)^2 + E_\gamma^2 \tilde{\Gamma}_{E1}^2(E_\gamma)} + \frac{0.7\Gamma_{E1}4\pi^2T^2}{E_{E1}^5}\right]\sigma_{E1}\Gamma_{E1}$$

with:

$$\tilde{\Gamma}_{E1}(E_\gamma) = \Gamma_{E1}\frac{E_\gamma^2 + 4\pi^2T^2}{E_{E1}^2}$$

and:

$$T = \sqrt{\frac{E_n + S_n - \Delta - E_\gamma}{a(S_n)}}$$

where $E_n$is the incident neutron energy, $S_n$is the neutron separation energy, $\Delta$is the pairing correction, and $a(S_n)$is the level-density parameter at the neutron separation energy.

For **strength 2**, the Brink-Axel standard Lorentzian is written as:

$$f_{X\ell}(E_\gamma) = K_{X\ell}\frac{\sigma_{X\ell}E_\gamma\Gamma_{X\ell}^2}{\left(E_\gamma^2 - E_{X\ell}^2\right)^2 + E_\gamma^2\Gamma_{X\ell}^2}$$

where $\sigma_{X\ell}$, $E_{X\ell}$, and $\Gamma_{X\ell}$are the strength, energy, and width of the giant resonance, respectively.

For **strength 3**, TALYS uses microscopic Skyrme-Hartree-Fock BCS photon strength functions with QRPA. Since this option is implemented through tabulated microscopic strength functions, it is not represented by a single Lorentzian analytical expression in this appendix.